2023

Development of Zeolitic Imidazolate Framework-Derived Carbon Hosts for Advanced Lithium Metal Anodes

Hamzeh Qasem Qutaish

UNIVERSITY
OF WOLLONGONG
AUSTRALIA

Development of Zeolitic Imidazolate Framework-Derived Carbon Hosts for Advanced Lithium Metal Anodes

Hamzeh Qasem Qutaish

Supervisors:

Prof. Jung Ho Kim

Prof. Konstantin Konstantinov

This thesis is presented as part of the requirement for the conferral of the degree:

Doctor of Philosophy

University of Wollongong

School of Engineering and Information Sciences

Institute for Superconductive & Electronic Materials

April 2023

CERTIFICATION

I, Hamzeh Qutaish, declare that this thesis is submitted in partial of the requirements for the award of Doctor of Philosophy, in the institute for superconducting & electronic materials (ISEM), the Australian Institute of Innovative Materials (AIIM), University of Wollongong, NSW, Australia. This thesis is wholly my own work unless otherwise referenced or acknowledged. All the experimental data is original. This thesis has never been submitted for qualification at any other academic institution.

Hamzeh Qutaish, 2023

ACKNOWLEDGMENT

This PhD dissertation would not have seen the light without the help and support of many people.

First of all, I would like to express my recognition and gratitude to my academic supervisor Professor Jung Ho Kim. Your advice, support, care, and friendship are the reasons for the delivering of this thesis.

Additionally, I owe a great deal to my co-supervisors; Prof. Konstantin Konstantinov, Prof. Min-sik Park, and Prof. Janghyuk Moon for their insightful feedback and continuous guidance.

The privilege of working with Prof. Kim has extended to include many lab members who became incredible friends. Special thanks to Jaewoo Lee, Sang A Han, and Hani-Yup Yum for the stimulating discussions and tremendous help throughout my thesis progression.

I am fully indebted to my dear parents for all of their encouragements, love, and support. I am not sure where I would be now without their eyes and continuous prayers. Thank you for believing in me and for always being by my side.

Finally, and most importantly, I wish to thank my beautiful wife, soulmate, and partner in crime, Reem. Thank you for your support over these years of study. I look forward to our future as a family with excitement and anticipation.

ABSTRACT

Lithium (Li) metal batteries have recently gained tremendous attention owing to their high energy capacity compared to other rechargeable batteries. Nevertheless, Li dendritic growth causes low Coulombic efficiency, thermal runaway, and safety issues, all of which hinder the practical application of Li metal as a promising anodic material. From the material development aspect, new and creative solutions are required to resolve the current technical issues on advanced Li batteries and improve their safety during operation.

The research encompassed in this work spans a broad investigation of utilizing Zeolitic imidazolate framework derived carbon (ZIF-C) as a 3D host material in Li metal batteries. The reason behind choosing ZIF-C in this thesis not only relies on its flexibility with which constituents' geometry, size, and functionality can be modified to match application needs, but also because it exhibits several outstanding properties, such as robust mechanical strength, large surface area and pore volume, and adequate electrical conductivity, making it a potential candidate for cost-effective practical usage. These host materials, however, could suffer from poor Li wettability, which results in significant nucleation barriers and upper surface electrodeposition of Li metal, leading to dendritic growth and safety concerns.

This thesis covers multiple aspects related to ZIF-C material. Firstly, the physical properties of porous ZIF-C, which can be controlled by the inorganic components, were thoroughly studied. This provided the basis of enhancing the properties of ZIF-C by varying the ratios of zinc/cobalt ion metallic precursors. A key finding from this study is that the initiation of carbon nanotubes growth and the pore size on the surface of ZIF-C is highly dependent on the Co/Zn ratio. Secondly, we theoretically demonstrated and experimentally correlated the growth mechanism of Li clusters on the surface of Co/Zn ZIF-C by employing different heteroatoms (pyridinic N,

pyrrolic N, quaternary N, and Co-N4). As a key feature, the Co-N4 affects the Li deposition behavior with axial Li growth on the surfaces of the carbon frameworks, while the other heteroatoms (i.e., nitrogen defects) induce unfavorable vertical Li growth. Thirdly, we functionalized the Co/Zn ZIF-C with oxidized nitrogen groups by utilizing nitric acid. We found that the functionalized porous carbon demonstrated an enhanced wettability compared to its non-functionalized counterpart. Moreover, by functionalizing the carbon surface with oxidized nitrogen during Li plating and stripping, catalyzed Li nitride (Li_3N) formed in the solid electrolyte interphase which effectively enhanced the surface morphology of Li deposition. The electrochemical measurements showed a massive improvement in the capacitive behavior of the functionalized porous carbon and an enhanced electrochemistry performance in terms of cyclability and reversibility.

Some additional theoretical and experimental work, involving advanced computational simulations and in situ characterization techniques, opens the door to further work in developing high-performance battery materials for the advance of a new generation of Li-based batteries.

TABLE OF CONTENTS

CHAPTER 1 . INTRODUCTION

1.1. Research Background

The term “secondary battery” refers to a rechargeable battery that can be used for converting electrical energy into the form of chemical energy, storing it, and then converting it back into the form of electrical energy when necessary. [1,2] A lithium (Li) secondary battery is one type of rechargeable battery and is a device that stores and generates electricity through charging and discharging using Li^+ ions. [3,4] Currently, Li-ion batteries (LIBs) are used as a universal power source for various portable electronic devices, leading the era of smart devices. Some say that the battery of things era has arrived, saying that energy can now be used anytime, anywhere without being constrained by time and space through innovation in secondary battery technology. [4-6] The largest demand for LIBs is coming from the need to power digital devices such as mobile phones, laptops, and the demand is expanding from portable information and communication devices to large-scale applications such as space and aviation, electric vehicles, hybrid vehicles, and advanced energy storage systems for supporting electrical grids. [7-9]

Figure 1.1 is a schematic diagram showing the history and development direction of secondary batteries starting with lead-acid batteries. In recent years, the market has been growing, largely based on the development of electric vehicles. [8-10] Research on secondary batteries has continued, starting with lead-acid batteries in the 1900s, nickel metal hydride (MH) batteries in the 1950s, and LIBs in the 1990s. [7,9,11] After Sony first developed LIBs in 1991, it spurred research on secondary battery development. Taking advantage of these opportunities, LIBs are currently being applied as essential power sources for mobile electronic devices, leading to the era of smart devices. [11,12] LIBs are free from the environmental hazards of lead-acid batteries and the memory effect that is a fatal weakness of nickel-metal hydride (nickel-MH) batteries,

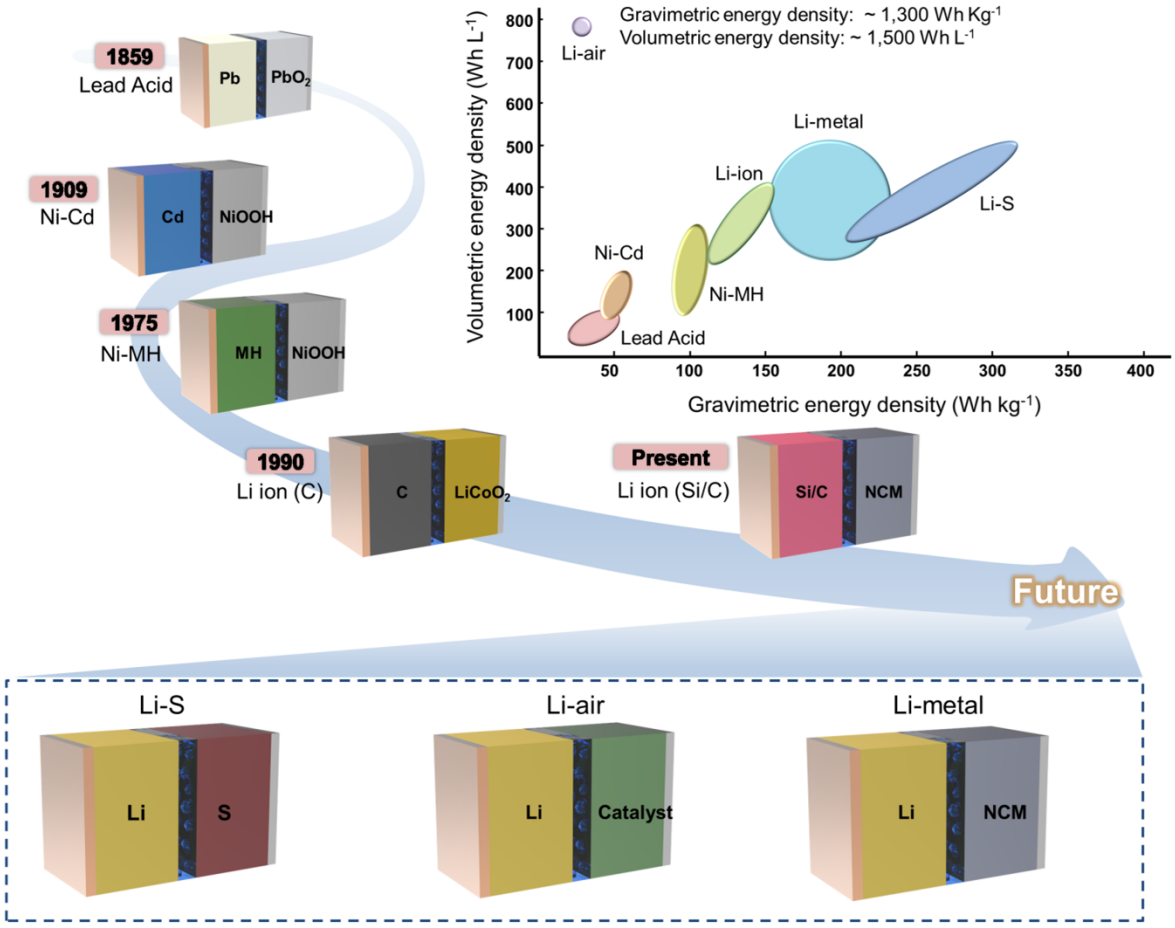

Figure 1.1. Schematic diagram showing the history and development direction of secondary batteries, with the inset showing the energy densities of the different types.

and they have superior gravimetric and volumetric energy densities compared to conventional secondary batteries. [12,13]

The energy density limitations of LIBs, however, have raised the need for more advanced types of new battery. [13,14] In order to meet the rapidly diversifying needs for secondary batteries, a technological innovation that encompasses issues of high energy, safety, and functionality is required. Current research on the next-generation batteries can be divided into LIB-related research, which corresponds to the mature stage, and future battery-related fields, corresponding to the introduction/growth stage, in consideration of the technological cycle.[14,15] Li-metal battery (LMB), Li-sulfur battery (LSB), and Li-air battery (LAB) have been studied to overcome the limitations of LIB's energy density.[15-20]

Each battery system has its own problems. Therefore, it is important to develop suitable electrode materials with appropriate physical and electrochemical properties (e.g., electronic and ionic conductivity, redox potentials, capacity, catalytic activity, etc.) and to implement novel structures and chemical compositions. [21,22] To realize this, new and creative solutions are needed for the development of materials. Polymeric and conductive carbon (C) materials, which are relatively low-cost and whose properties can be controlled to some extent through synthesis, suffer from a lack of chemical and physical stability for practical device implementation.[23] Solid inorganic materials (e.g., silicon and metal oxides) with a redox active sites and robust structure can also be used as electrode materials for Li battery.[24,25] Their slow ionic diffusion limits the charge/discharge rate, however, and induces large volume changes during cycling, leading to mechanical fragility. These shortcomings are inspiring the development and discovery of new types of advanced energy storage materials. [22, 24, 25]

Metal–organic frameworks (MOFs) are considered as attractive candidates to satisfy the demands of advanced energy storage technologies.[26,27] MOFs, which have outstanding characteristics, such as high surface area, large pore volume, and design flexibility, enabling easy functionalization to achieve desired properties.[26,28] In addition, porosity, one of the greatest characteristics of MOFs, also plays a significant role in energy storage and charge transport. The easily tunable capabilities of MOFs make them suitable for use as templates and precursors, allowing the synthesis of functional materials with desired properties, chemical composition, and unique morphology. [29-32]

1.2. Research Objectives

The primary aim of this thesis is to develop and characterize zeolitic imidazolate framework derived carbon (ZIF-C) as anodic materials for practical implementation in LMBs. The thesis objectives revolve around designing and functionalizing anodic materials to achieve some desired battery characteristics such as high capacities, long cycling life, and high columbic efficiency. To realize these outcomes, the following aims were addressed in this thesis:

1. To understand and study the main physical properties of ZIF-C, by controlling synthetic variables, including metal materials and ratios, in order to find the best parameters to obtain the desired properties for Li metal storage applications.
2. To find the correlation between Li growth mechanism and heteroatoms in ZIF-C framework by investigating the formation mechanism of Li cluster through DFT calculation along with experimental validation.
3. To study the effect of surface functionalization of ZIF-C on its electrochemical performance.

1.3. Thesis outline

The chapter following this introductory one provides a general background of the failure mechanism of the LMBs, including Li dendrite growth, instability of the SEI, and significant volume changes. We then discuss the main principles for utilizing carbon-based frameworks as Li host materials. Additionally, we discuss the recent progress on developing stable framework materials, including using one-, two-, and three-dimensional (1D, 2D, and 3D) carbon frameworks and composites. Lastly, we fully discuss the current state-of-the-art techniques that

involves enhancing the key characteristics of MOFs in order to satisfy the energy storage needs in LMBs.

The remaining chapters are arranged as follows. Chapter 3 is devoted to the work directly involved in optimizing the host material structure by varying the ratios of metallic contents to achieve the desired porous structures of high pore volumes and large surface areas. In addition, we studied the impact of metallic content on the electrical properties of the host materials.

Chapter 4 is focused on understanding the growth mechanism of Li clusters during Li plating. By considering nitrogen heteroatoms and cobalt in the carbon framework, the density functional theory (DFT) and experimental results are systematically compared. We further verify the local electronic structure and adsorption of Li ions from the viewpoints of Li deposition for next-generation Li metal batteries.

Chapter 5 is aimed at functionalizing ZIF-C with oxidized nitrogen groups to increase electronegativity towards Li and decrease the Li nucleation overpotential. The functionalized ZIF-C also catalyzed Li_3N within the SEI, thus improving its ionic conductivity and electrochemical performance.

Chapter 6 provides a conclusive review of what has been achieved and the relevance of our findings to the field of energy storage materials in the current context. Future work is also suggested to improve the performance of the developed materials.

Main chapters (Chapter 2-6) were compiled from the articles which were already published or submitted to peer-reviewed journals. Article citation/s for each chapter is shown below (Table 1.1).

Table 1.1. Journal articles for the thesis compilation.

Chapter 2	1. **Hamzeh Qutaish**, Sang A. Han, Yaser Rehman, Konstantin Konstantinov, Min-Sik Park, and Jung Ho Kim. "*Porous carbon architectures with different dimensionalities for lithium metal storage*." **Science and Technology of Advanced Materials** 23, no. 1 (2022): 169-188. 2. Han, Sang A., **Hamzeh Qutaish**, Jong-Won Lee, Min-Sik Park, and Jung Ho Kim. "*Metal-organic framework derived porous structures towards lithium rechargeable batteries*." **EcoMat** 5, no. 2 (2023): e12283.
Chapter 3	**Hamzeh Qutaish**, Jaewoo Lee, Yuhwan Hyeon, Sang A. Han, In-Hwan Lee, Yoon-Uk Heo, Dongmok Whang, Janghyuk Moon, Min-Sik Park, and Jung Ho Kim. "*Design of cobalt catalysed carbon nanotubes in bimetallic zeolitic imidazolate frameworks*." **Applied Surface Science** 547 (2021): 149134.
Chapter 4	**Hamzeh Qutaish**, Hongjun Chang, Joo Hyeong Suh, Sang A Han, Han-Yup Yum, Min-Sik Park, Jan-ghyuk Moon, and Jung Ho Kim. "*Growth mechanism of lithium clusters on the surface of porous carbon framework for lithium metal batteries."* **ACS Materials Letters** 5, no. 6 (2023): 1593-1600.
Chapter 5	**Hamzeh Qutaish**, Joo Hyeong Suh, Sang A. Han, Soyeun Kim, Min-Sik Park, and Jung Ho Kim. "*Regulation of ionic conductivity and lithium affinity of porous carbon framework in Li metal batteries through oxidized nitrogen groups*." **Applied Surface Science** 605 (2022): 154757.

1.4. References

1. Wu F, Maier J, Yu Y. Guidelines and trends for next-generation rechargeable lithium and lithium-ion batteries. Chem Soc Rev 2020; 49: 1569-1614.
2. Xu G, Nie P, Dou H, Ding B, Li L, Zhang X. Exploring metal organic frameworks for energy storage in batteries and supercapacitors. Mater. Today 2017; 20:191-209.
3. Weiss M, Ruess R, Kasnatscheew J, et al. Fast charging of lithium-ion batteries: A review of materials aspects. Adv Energy Mater 2021; 11:211126.
4. He X, Bresser D, Passerini S, et al. The passivity of lithium electrodes in liquid electrolytes for secondary batteries. Nat Rev Mater 2021; 6:1036–1052.
5. Galos J, Pattarakunnan K, Best AS, Kyratzis IL, Wang C-H, Mouritz A. P. Energy storage structural composites with integrated lithium-ion batteries: A review. Adv Mater Technol 2021; 6:2001059.
6. Chen S, Dai F, Cai M. Opportunities and challenges of high-energy lithium metal batteries for electric vehicle applications. ACS Energy Lett 2020; 5:3140-3151.
7. Hyeon Y, Lee J, Qutaish H, et al. Lithium metal storage in zeilitic imidazolate framework drived nanoarchitectures. Energy Storage Mater 2020; 33:95-107.
8. Wang Q, Liu B, Shen Y, et al. Confronting the challenges in lithium anodes for lithium metal batteries. Adv Sci 2021; 8:2101111.
9. Zhao Y, Guo J. Development of flexible Li-ion batteries for flexible electronics. InfoMat 2020; 2:866-878.
10. Gao X, Dong Y, Li S, Zhou J, Wang L, Wang B. MOFs and COFs for batteries and supercapacitors. Electrochem Energy Rev 2020; 3:81-126.
11. Xu Y, Li Q, Xue H, Pang H. Metal-organic frameworks for direct electrochemical applications. Coord Chem Rev 2018; 376:292-318.
12. Zhang W, Liu Y, Zhang L, Chen J. Recent advances in isolated single-atom catalysits for zinc air batteries: A focus review. Nanomaterials 2019; 9:1402.
13. Reddy RCK, Lin J, Chen Y, et al. Progress of nanostructured metal oxides derived from metal-organic frameworks as anode materials for lithium-ion batteries. Coord Chem Rev 2020; 420:213434.
14. Mehtab T, Yasin G, Arif M, et al. Metal-organic frameworks for energy storage devices: Batteries and supercapacitors. J Energy Storage 2019; 21:632-646.
15. Shin H, Baek M, Gupta A, Char K, Manthiram A, Choi JW. Recent progress in high donor electrolytes for lithium-sulfur batteries. Adv Energy Mater 2020; 10:2001456.

16. Liu T, Vivek JP, Zhao EW, Lei J, Garcia-Araez N, Grey CP. Current challenges and routes forward for nonaqueous lithium-air batteries. Chem Rev 2020; 120:6558-6625.
17. Kang J-H, Lee J, Jung J-W, et al. Lithium-air batteries: Air-breathing challenges and perspective. ACS Nano 2020; 14:14549-14578.
18. Liang Y, Lai W-H, Miao Z, Chou S-L. Nanocomposite materials for the sodium-ion battery: A review. Small 2018; 14:1702514.
19. Sun M, Jiang Y, Ni J, Li L. Application of materials based on group VB elements in sodium-ion batteries: A review. J Mater Sci Technol 2018; 34:1969-1976.
20. Hosseini S, Soltani SM, Li Y-Y. Current status and technical challenges of electrolytes in zinc-air batteries: An in-depth review. Chem Eng J 2021; 408:127241.
21. Zhang Y, Deng Y-P, Wang J, et al. Recent progress on flexible Zn-air batteries. Energy Storage Mater 2021; 35:538-549.
22. Kumar P, Pournara A, Kim K-H, Bansal V, Rapti S, Manos MJ. Metal-organic frameworks: Challenges and opportunities for ion-exchange/sorption applications. Prog Mater Sci 2017; 86:25-74.
23. Hankari SEl, Bousmina M, Kadib AEl. Biopolymer@metal-organic framework hybrid materials: A critical survey. Prog Mater Sci 2019; 106:100579.
24. Li W. Metal-organic framework membranes: Production, modification, and applications. Prog Mater Sci 2019; 100:21-63.
25. Liang Z, Zhao R, Qiu T, Zou R, Xu Q. Metal-organic framework-derived materials for electrochemical energy applications. EnergyChem 2019; 1:100001.
26. Zhao R, Liang Z, Zou R, Xu Q. Metal-organic frameworks for batteries. Joule 2018; 2:2235-2259.
27. Xu G, Nie P, Dou H, Ding B, Li L, Zhang X. Exploring metal organic frameworks for energy storage in batteries and supercapacitors. Mater Today 2017; 20:191-209.
28. Zhu JP, Wang XH, Zuo XX. The application of metal-organic frameworks in electrode materials for lithium-ion and lithium-sulfur batteries. R Soc Open Sci 2019; 6:190634.
29. Li H, Eddaoudi M, O'Keeffe M, Yaghi OM. Design and synthesis of an exceptionally stable and highly porous metal-organic framework. Nature 1999; 402:276-279.
30. Xuan W, Zhu C, Liu Y, Cui Y. Mesoporous metal-organic framework materials. Chem Soc Rev 2012; 41:1677-1695.
31. Li B, Wen H-M, Cui Y, Zhou W, Qian G, Chen B. Emerging multifunctional metal-organic framework materials. Adv Mater 2016; 28:8819-8860.

32. Sanati S, Abazari R, Albero J, et al. Metal-organic framework derived bimetallic materials for electrochemical energy storage. Angew Chem Int Ed 2021; 60:11048-11067

CHAPTER 2 . LITERATURE REVIEW

2.1. Introduction

During recent decades, research on energy storage systems has grown massively as a result of the escalating global shortage of fossil fuels. [1-3] Li-ion batteries (LIBs) have emerged as a primary source of power for various electrical devices due to their favorable characteristics, such as high thermal stability, energy capacity, durability, and environmental friendliness. [4-7] Even though LIBs can power small, portable electric devices, they are inadequate for long-range electric vehicles (EVs) because of their lengthy charging duration and short operation time. In addition, there is still a demand for higher excess energy storage than what LIBs currently provide to accommodate more electrochemical energy from intermittent renewable resources. [8-10] These resources, such as those harvested from hydroelectric, wind, and solar power, require large-scale and cost-effective energy storage devices with higher capacity. [11-14]

Li metal anode has stood out as an ideal candidate, not only due to its ultrahigh theoretical specific capacity (3860 mA h g^{-1}), but also its lowest redox potential among the alkali metals (-3.04 V vs. standard hydrogen electrode), and light weight (0.53 g cm^{-3}). In particular, the specific energy density of Li metal batteries (LMBs) is expected to reach as high as 700 W h kg^{-1}. [15,16] Moreover, LMBs have gained substantial interest, including all-solid-state LMBs as well as Li-S and Li-air batteries, where the energy density was speculated to reach 2600 W h kg^{-1} for Li-S and 11680 W h kg^{-1} for Li-air. [15-19]. Nevertheless, Li metal suffers from severe drawbacks that hinder its usage in practical applications, including unstable or uneven solid-electrolyte interphase (SEI), the formation of dead Li, dendrite growth, and volume changes during plating and stripping processes. These lead to severe issues, such as short-

circuiting, low Coulombic efficiency (CE), capacity loss, and safety complications. [17,20,21] Consequently, a plethora of research studies has been devoted to overcoming the failure mechanism of the LMBs, including stabilizing the SEI using electrolyte additives, preventing dendrite penetration via artificial SEI layers of high modulus or solid-state electrolytes, and guiding uniform Li deposition by utilizing three-dimensional (3D)-constructed porous hosts. Among these strategies, the latter technique has gained tremendous attention. [22,23]

One of the candidates with the greatest potential for cost-effective practical usage of 3D-constructed porous hosts is carbon-based frameworks, as they exhibit several outstanding properties, [18,22] and has been integrated in multiple applications. [24-29] In details, a carbon-based framework has excellent electrical conductivity that facilitates continuous electron

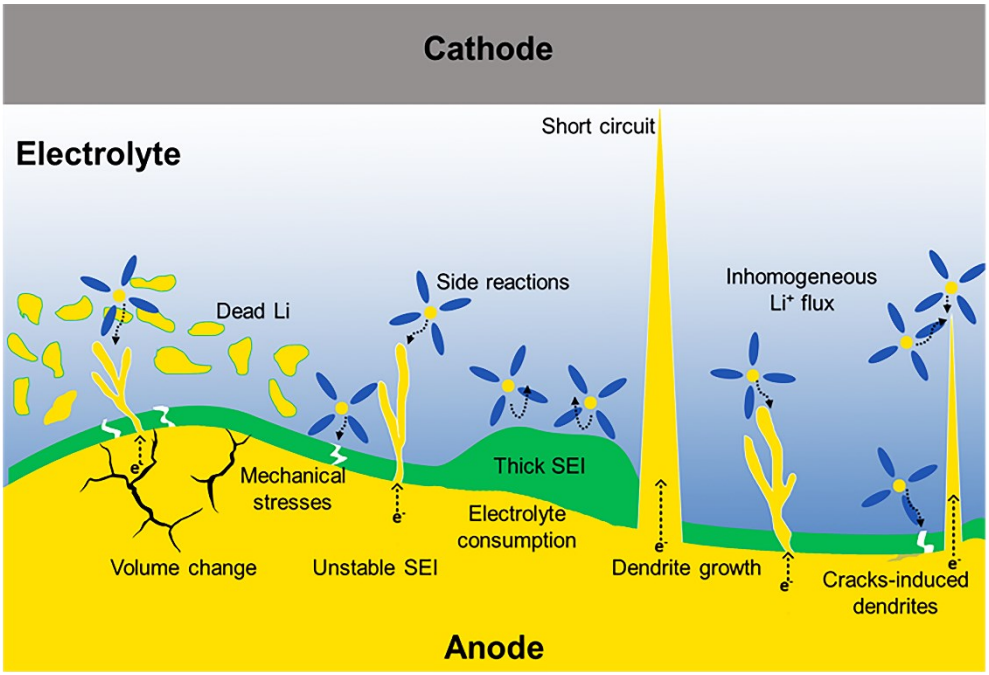

Figure 2.1. Schematic illustration of the failure mechanisms that occur in Li metal anode; Infinite volume expansion of Li metal causes instability of SEI and induces mechanical stresses that destroy the integrity of the anode. Extremely thick SEI layer causes high interfacial impedance. The dendritic growth forms in various dendritic structures, such as trees and whiskers. The further extension of these Li dendrites can lead to a loss in their electric contact with the anode during stripping, resulting in “dead Li”. Furthermore, long dendrites can cause short circuits.

transport and limits electrode polarization. Moreover, the large surface area of the carbon-based framework reduces the local current density of the anode and prevents dendrite growth by tuning the lithiophilicity of the surface. In addition, the pore network inside the carbon-based framework shows high electrochemical stability and can store a large amount of metallic Li while maintaining the structural integrity of the electrode. Finally, a carbon-based framework exhibits robust mechanical strength that permits volume change accommodation and internal stress resistance. [30-33]

2.2. Failure mechanism of Li metal anode

The failure mechanisms of the Li metal anodes are primarily associated with uncontrollable dendritic Li growth, infinite volume changes, and the unstable SEI, which all occur during electrochemical cycling, as shown in Figure 2.1. [34-38]

2.2.1. Infinite volume change

The volume change of the battery during operation is a common serious issue, which afflicts almost all commercially available electrode materials. For example, the “rocking chair” model shows that the volume changes of graphite- and silicon-based electrodes are limited to 10 % and 400 %, respectively. [17,20] Utilizing bare Li metal as an anode, on the other hand, causes infinite volume expansion due to its “hostless” nature. The problem starts with the Li interface movement during the stripping/plating process, in which the volume expansion could reach up to tens of micrometers in thickness, imposing SEI instability (see Figure 2.1). In addition, the significant volume changes may induce mechanical stresses that destroy the integrity of the anode and increase electrode impedance and capacity fade. [7,29]

2.2.2. Unstable solid-electrolyte interphase (SEI)

Conceptually, the electrolyte reduction on the surface of the electrode forms a bilayer SEI film, which consists of a main layer that directly grows on the anode surface and a second

porous layer that originates from the solution side. Therefore, the SEI can block electrons and conducting ions. In normal circumstances, the formation of the SEI film on the battery's electrode can eliminate excessive reactions between the electrode and electrolyte. Utilizing Li metal as the anode, however, can result in a fragile and unstable SEI with variable morphology and thickness, owing to the high reactivity of Li and infinite volume change (Figure 2.1).[35] This takes place during battery cycling, in which the Li anode surface can spontaneously react with various polar-aprotic electrolyte solvents and salts. In addition, the morphology of the Li metal deposited on the electrode surface is highly affected by the diffusion behavior through the SEI layer. In other words, an extremely thick SEI layer, as shown in Figure 2.1, causes high interfacial impedance while an extremely thin SEI layer cannot protect the electrode from side reactions.[17] Furthermore, the irreversible Li depletion usually degrades the CE of LMBs, which severely affects its overall performance and becomes the main obstacle to practical applications. In addition, the SEI continues to react and consume more fresh Li ions to compensate for the breaking of its integrity, which eventually leads to low CE and faded capacity. [17,39]

2.2.3. Dendritic growth

Dendritic growth is a well-known phenomenon that emerges during metal electroplating. The Li-ions within the electrolyte acquire electrons and are deposited on the surface of the anode, forming various dendrite structures, such as trees, snowflakes, needles, and whiskers. [40-43] The ungovernable generation of dendrites during battery cycling increases the surface area of the electrode, which increases the side reactions between the electrolyte and the Li metal. Consequently, the Li-ions would favor the dendrites as their deposition surface due to the stronger electric fields and larger electroactive surfaces, inducing more unnecessary side reactions. This results in rapid consumption of the electrolyte, and accelerating capacity fading, (see Figure 2.1). [42] Moreover, the further extension of a Li

dendrite can lead to the loss of its electronic contact with the electrode during stripping, a phenomenon called “dead Li”, which reduces the active material, minimizes the surface area, and renders huge impedance. Moreover, the continuous growth of the Li dendrites can generate sharp and long ones that could reach the surface of the cathode while penetrating the separator, causing an inner short circuit within the electrochemical cell. Short circuits are accompanied by heat dissipation, and thus electrical fires and explosions, as illustrated in Figure 2.1. [34,42,44]

2.3. Li deposition and dendritic growth

As explained in the previous section, dendritic Li growth causes many significant challenges that hinder the practical application of LMBs. Hence, realizing the main factors that play a role in dendritic growth is the first step, including the failure mechanisms and appreciating the importance of utilizing engineered carbon-based frameworks as a powerful solution.

2.3.1. General models of Li formation and dendritic growth

During the last four decades, many theoretical models have been established to investigate the factors and processes responsible for dendritic growth. This section discusses some standard essential models. At the beginning of the Li plating process, the Li-ions start migrating to the electrode surface under the dual effects of the concentration gradient and the electric field. The Li-ions will be reduced and start nucleating, in which the speed of Li-ion consumption and deposition relies on the applied current density. [23,40,45] Therefore, the cathode begins to supply Li ions to macroscopically compensate for the Li-ion depletion at the anode, which also relies on the applied current density. Hence, the microscopic distribution of these ions at the anode governs the overall deposition morphology. For this reason, Brissot et al. have provided one of the most widely acceptable models that demonstrates the dendritic

growth mechanism based on the concentration gradient near the electrode, [46-48] as illustrated in the following equation:

$$\frac{\partial C}{\partial x}(x) = \frac{J\mu_a}{eD(\mu_a + \mu_{Li})} \quad (1)$$

where e is the electric charge, D is the ambipolar diffusion coefficient, C is the Li^+ concentration in the electrolyte, J is the effective current density, μ_a is the anionic mobility, and μ_{Li} is the Li-ion mobility.

The change in ionic concentration ($\partial C/\partial x$) from the anode to the cathode is linearly correlated to J. In contrast, two different types of behavior are expected from a Li symmetric cell at low and high applied current densities, depending on the initial concentration, C_0, D, and the inter-electrode distance (L). At a low current density, when $\partial C/\partial x < 2\ C_0/L$, the deposition of Li ions shows a smooth surface morphology. In contrast, at a high current density, when $\partial C/\partial x > 2\ C_0/L$, the Li-ion and anionic concentrations behave differently at a certain point, forming a localized space charge. This results in a large electric field, thus inducing dendritic growth. More specifically, Chazlviel et al. described the relationship between the current density (J) and the time at which the ionic concentration vanishes at the anode, denoted as Sand's time (τ). The Sand's time is inversely proportional to J^2, so that a high value of τ means that a longer time is needed for Li deposition. [49] This correlation and other influential factors are presented in the following equation:

$$\tau = \pi D \left(\frac{eC_0}{2Jt_a}\right)^2 \quad (2)$$

where t_a is the anionic transference number. A low τ value means that the dendritic growth will initiate in a shorter time. The Chazalviel model is considered as one of the most reliable models that simulates and predicts the Li deposition behavior at high current density. Other

experimental results and models, however, have clearly demonstrated that the Chazalviel model can also be extended to low current densities. This was attributed to the local fluctuations of current density on the anode surface. [50-52]

For example, one study by Cheng et al. showed that mossy-like (2D) dendrites are induced at low current densities due to the kinetic limitations of Li reduction (Figure 2.2a). [43,44,53] The high current density, in contrast, causes three-dimensional dendritic growth due to rapid Li-ion depletion in the proximity of the electrode surface. Another recent study, Bai et al., explains the dendritic growth analytically at various current densities using a nanoporous ceramic separator and Li metal anode (Figure 2.2b). [54,55] First, if the current density is less than its critical value ($J < J_{cc}$), the mechanism of dendrite growth is called 'root-growth', and the structure becomes whisker-like. In this case, the SEI remains intact, and the deposition occurs beneath until it reaches a certain point of time when pinholes in the SEI begin to release pressure in the form of whisker-like dendrites (Figure 2.2b). The whiskers protrude as wires from the SEI surface when the deposition continues further. On the other hand, if the current density is more than the diffusion-limited current density ($J > J_{lim}$), the aforementioned Chazalviel model is applied, where tree-like dendrite structures form (Figure 2.2b). Bai et al. added to this model an additional interesting regime in between ($J_{cc} < J < J_{lim}$), where the intermediate current density is applied at a rate that is similar to the rate of SEI formation. This causes mossy-like dendritic growth with a non-uniform interfacial layer (Figure 2.2b).

Another model, proposed by Monroe and Newman, addressed the growth rate of the dendrites under different galvanostatic conditions. [56,57] The model demonstrated that the local electric field is intensely increased at the tip of a dendrite, inducing further Li deposition from the electrolyte and thus accelerating its growth.

Additional thermodynamic factors also contribute to the dendritic growth besides the kinetic factors. Ely et al. designed analytical frameworks for reaction-rate-limited systems to anticipate Li growth and nucleation during electrodeposition. [58] The work showed different five

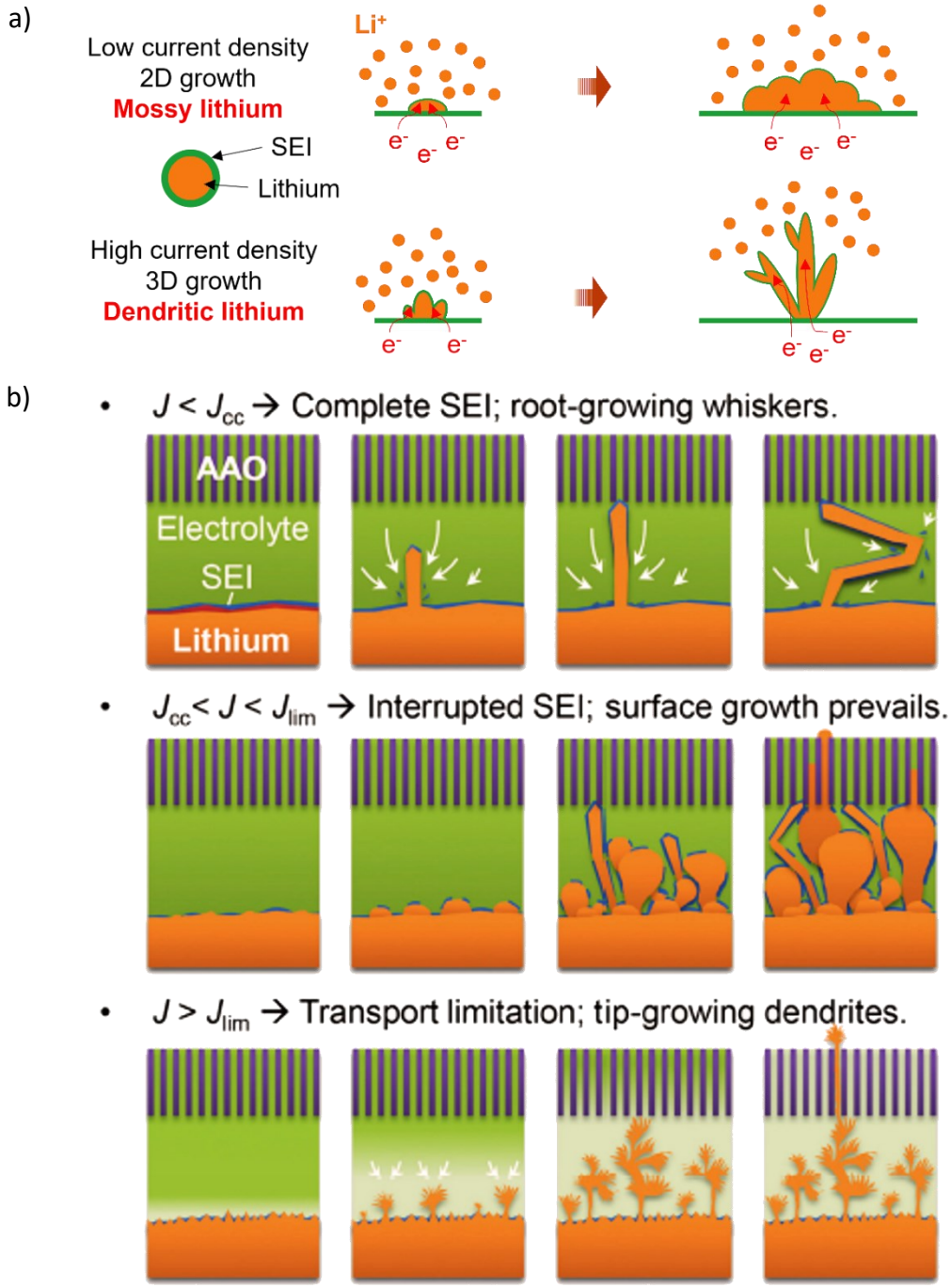

Figure 2.2. a) Schematic illustration showing the early stages of Li dendritic growth at different current densities. [44] b) The different types of Li dendritic growth and their interactions with a nanoporous alumina separator under different current density conditions. AAO: anodic aluminium oxide. [54]

regimes of nucleation behaviour, including short incubation time, long incubation time, nucleation suppression, early growth, and late growth (Figure 2.3a). In the nucleation suppression regime, the embryos were unable to persist and thermodynamically unstable, which possibly caused them to dissolve back into the electrolyte. In the long incubation time regime, the embryos were in a thermodynamically favored and metastable condition, in which they persisted without growing until they were subjected to thermal variations. In the short incubation time regime, narrow-sized embryos started to nucleate faster with increasing overpotential. Thermodynamic and kinetic stability in the growth of nuclei were displayed in the early growth regime, where the growth rate reached the constant terminal velocity.

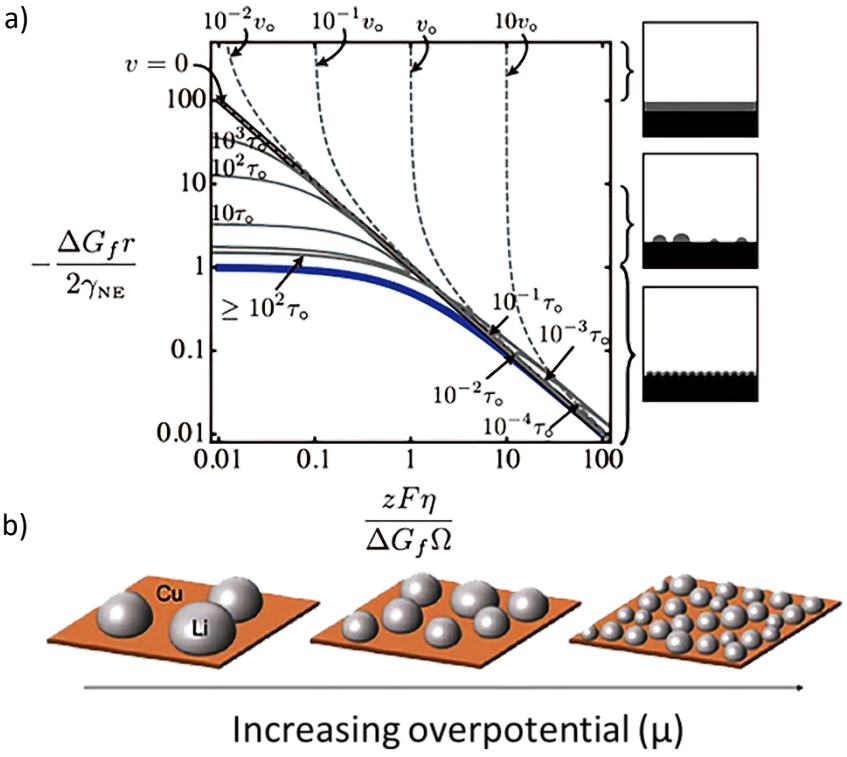

Figure 2.3. The main regimes of the initial stage behavior of Li nucleation and growth. a) Above the black bold curve, there is a zone of stable Li growth. Below the blue curve is the undesirable Li growth zone. The solid grey curves represent the fixed incubation times. The dotted grey curves highlight the initial velocities of Li nucleation. [58] b) Schematic illustration of the size and density of Li nuclei deposited on Cu current collectors at different nucleation overpotentials. [59]

Eventually, the late growth regime included unstable morphologies that were dominated by the localized electric fields, as shown in Figure 2.3a.

A recent study by Pei et al. that investigated the Li deposition morphology at different current densities, illustrated the dependence of the shape, size, and areal density of Li nuclei on the current rate, as shown in Figure 2.3b. [59] This aligns with the classical nucleation and growth theory, as they found that the size of the nuclei is inversely proportional to the nucleation overpotential and that the density of the nuclei is directly proportional to the cubic power of the overpotential.

The deposition and solution model has demonstrated that mechanical stress causes dendritic growth. [23,60] The Laplace's equation (2) shows the relationship between surface tension (γ), pressure difference (ΔP), and orthogonal curvature radii (R_1, R_2) as described:

$$\Delta P = \gamma \left(\frac{1}{R_1} + \frac{1}{R_2}\right) \tag{3}$$

on the basis of this model, Yamaki et al. conducted a study on utilizing hard films with surface tension of more than 0.2 N/m to prevent dendrite penetration mechanically, acting as a blocking layer. [61,62]

The studies and theories mentioned above provide a comprehensive understanding of the main mechanisms and factors contributing to dendritic growth, which paves the way toward designing and engineering stable anode materials utilizing a carbon-based framework.

2.4. Principles toward utilizing carbon-based frameworks as Li host materials

Based on the aforementioned models and discussion, tremendous attention has been drawn toward designing Li host frameworks to regulate and stabilize the LMBs. Carbon matrices, such as graphite felts, carbon nanotubes, graphene, hollow carbon nanospheres, and

carbon foams, are among the most researched candidates owing to their easily controlled properties, cost-effectiveness, and easy synthesis and functionalization for real practical applications of LMBs. [18,63-67] In this section, the main principles that must be considered to utilize carbon matrices as Li host materials will be discussed.

As inferred earlier, the initial nucleation of dendritic growth and its rate is mainly affected by the non-uniform distribution of the Li-ion flux on the electrode surface, which arises from the enormously high local current density. To slow down the nucleation of dendrites, carbon-based frameworks were initially designed to offer a larger surface area that increases Sand's time by decreasing the local current density (*J*). Nevertheless, unwanted massive electrolyte consumption might occur during the SEI formation due to the large electrode/electrolyte interface area. As a result, the impedance for Li-ion transport may increase, leading to premature death of the LMB. [63,68-70]

This concept was demonstrated by Jeong et al., who compared two different pore sizes and surface areas of carbon material (Figure 2.4a). [71] The microporous carbon (MSP-20) with a pore size of < 2.0 nm and a surface area of 2110 m^2g^{-1} showed a significant decrease in the CE after the 80^{th} cycle and faded at around the 110^{th} cycle. In contrast, the mesoporous carbon (CMK-3) with a pore size of 3.4 nm and a surface area of 1120 m^2g^{-1} exhibited stable cycling up to 200 cycles and a CE of > 95 %. The results of this study provide evidence that surface area is not the only factor that affects the dendrite growth, but also the pore size.

The high mechanical stability and flexibility of a carbon-based framework are essential properties to stabilize the SEI by alleviating volume change, suppressing the Li dendrite growth, and inhibiting the electrode disintegration. These properties make the SEI less susceptible to swelling-related stresses and fluctuations during Li plating/stripping cycles. [18,31,33,72,73] One study, conducted by Zheng et al. provided evidence that interconnected amorphous hollow carbon nanospheres, acting as a monolayer coating for Li metal anode, as shown in Figure 2.4b,

help in isolating the deposition of Li metal and facilitating the formation of a stable SEI. [74] In another study, conducted by Liu et al., a 3D porous structure was constructed as a Li metal host, which was made of carbon cloth and interconnected carbon nanotubes (CNTs) (CC/CNT). [75] The results showed that the porous structure of CC/CNT offered enough space to suppress

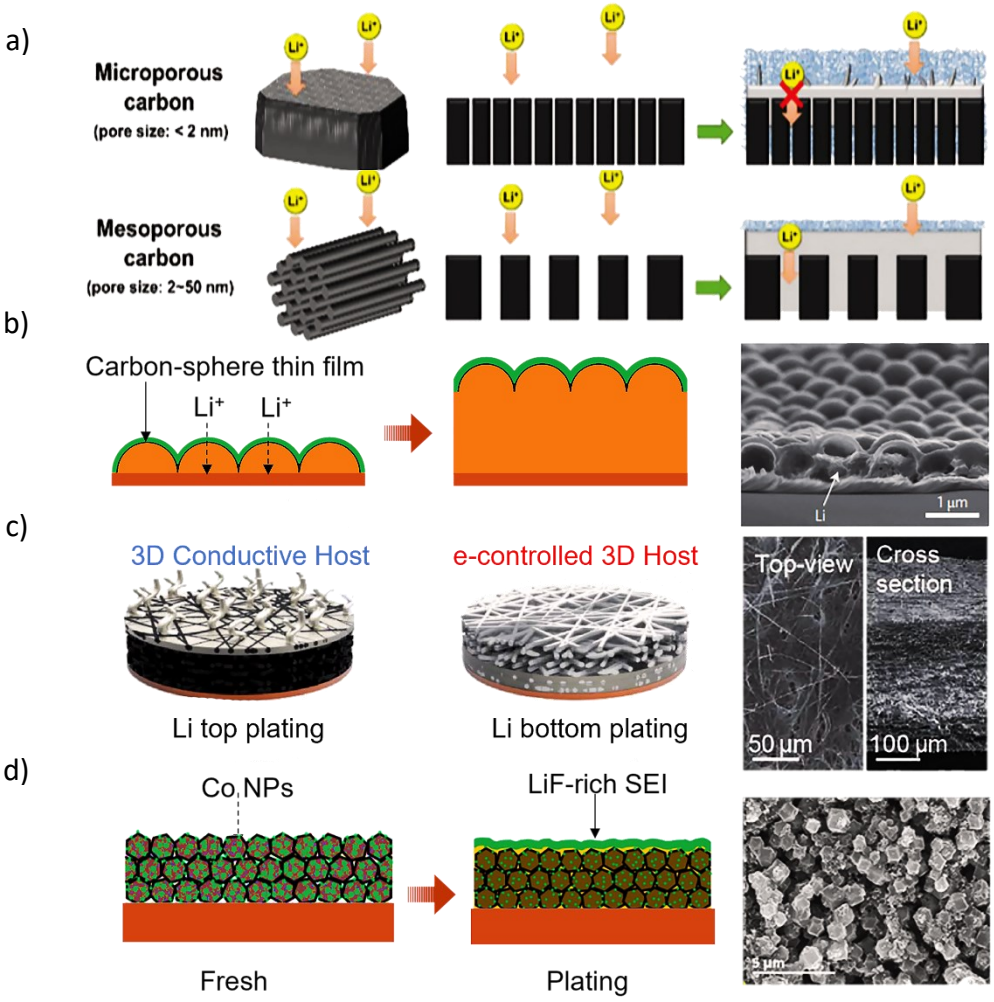

Figure 2.4. a) Schematic representation of the effects of different pore sizes on Li deposition behavior. [71] b) The hollow carbon nanospheres act as a scaffold to stabilize the SEI layer. The scanning electron microscopy (SEM) image on the right displays no dendritic growth after Li deposition. [74] c) Schematic illustration of the behavior of Li plating on an electrical conductivity-controlled 3D host and a 3D conductive host. The SEM images present different views of the pristine partially reduced graphene oxide –graphene foam (PrGO–GF)/Cu electrode. [89] d) LiF-rich SEI formation on Co-ZIF-C electrode stabilizes the cycling performance. The SEM image shows no dendritic growth after cycling. [90]

volume changes, whereas the CNTs on the top surface acted as active sites to reduce the local current density. Consequently, a stable SEI was formed, and battery life was extended.

For practical application, a large pore volume and low mass density are necessary to increase the gravimetric capacity by holding more Li inside the host materials while maintaining the structural integrity of the electrode. [76-78] For example, to achieve a gravimetric energy capacity of 3860 mA h cm^{-2} for 1 g of Li metal, the volume required is 1.87 cm^3. This means the host materials should offer a large pore volume to accommodate the Li and increase its energy storage properties. [79,80] Theoretically, the gravimetric capacity of carbon-based frameworks can be calculated via the following equation:

$$Q_{theortical,g} = \frac{V \times Q_{Li} + m_c \times Q_c}{m_{Li} + m_c} \quad (4)$$

where $Q_{theortical,g}$ is the theoretical gravimetric capacity, Q_c is the theoretical volumetric capacity of carbon, Q_{Li} is the volumetric capacity of Li, V is the pore volume, and m_c and m_{Li} are the masses of the carbon frameworks and the Li-metal, respectively. Although high pore volume is the desired property, carbon-based frameworks usually exhibit low reversibility in terms of areal capacity. A study that employed a Li-metal-filled carbon fiber network as a host material, showed that while the gravimetric and areal capacities were enhanced by 2000 mA h g^{-1} and 19 mA h cm^{-2}, respectively, the reversibility was for one discharge only. [81] Typically, practical applications of Li-metal anodes require a reversible areal capacity that is higher than 5 mA h cm^{-2}, which most studies in the literature have not yet accomplished. Therefore, other factors were investigated to increase the reversibility, including the pore size and depth. [82] As discussed earlier in Figure 2.4a, micropores show resistance to Li storage, while mesopores show higher Li storage and reversible capacity. The morphology of the Li deposition is also governed by the pore depth, as the distribution of electric field can be altered by tuning the pore

depth as well as the chemistry of the host material, which will be discussed in the following section. [83,84]

The electrical conductivity of the host material is another crucial aspect to consider when designing the carbon-based framework, because it facilitates continuous electron transport and limits electrode polarization. Therefore, a highly conductive framework can result in fast Li-ion transportation and capture. [78] Nevertheless, if the electrical conductivity of the host material is non-uniform, this could result in irregular Li deposition, since the regions of higher electrical conductivity quickly capture more Li ions compared to other regions of lower conductivity. [85-86] Creating a conductivity gradient within the Li host is an effective strategy that is used to generate more current flow in bottom deposition. [88] A 3D conductive framework was introduced by Park et al. that ultimately mitigated the dendrite growth by integrating non-conductive glass fiber or polyacrylonitrile (PAN) as a top membrane, as shown in Figure 2.4c. [89] This layer induced a conductivity gradient that ensured a proper distribution of Li-ion flux and regulated the bottom-up Li deposition, enhancing the overall performance.

The chemical stability and composition of the carbon-based framework are additional properties that prevent side reactions with the electrolyte under the redox environment and maintain a robust SEI, respectively. [18,72] Lee et al., for instance, demonstrated the role of cobalt (Co) nanoparticles, which were integrated into a porous carbon framework, in forming a thick Li fluoride layer that dominated the SEI in ether-based electrolytes. [90] The results showed that the host anode containing Co nanoparticles exhibited an outstanding electrochemical performance with a high CE and a stable long-term operational lifespan (see Figure 2.4d).

2.5. Wettability of carbon-based frameworks

In normal circumstances, the mechanism of electroplating is known to start when the Li-ions approach the anode from the bulk electrolyte, after which, they shed off the solvent molecules to reduce themselves and transform to Li adatoms. Following this, the Li adatoms diffuse on the surface of the anode until they become incorporated into the metal lattice.[91] This is not the ideal case, however, as weak interactions and a high diffusion barrier are expected, which make the Li metal thermodynamically susceptible to dendritic growth. Based on this, a detailed understanding of the chemistry of the carbon-based framework and its structure needs to be considered. These materials might suffer from poor Li wettability, which results in significant nucleation and diffusion barriers as well as upper surface electrodeposition of Li metal. [1,17,38,43,58,92]

The pore structures and the Li wettability of the carbon-based frameworks are of special importance according to the classical heterogeneous nucleation theory, which explains the dependence of the nucleation barrier on the Li wettability of the anode material, as described in the following equation:

$$\Delta G_{het} = S(\theta)\Delta G_{hom} \quad (5)$$

where ΔG_{het} and ΔG_{hom} are the heterogeneous and homogeneous nucleation barriers, respectively. The heterogeneous nucleation barrier ΔG_{het} is also determined by the shape factor $S(\theta)$, which corresponds to the surface morphology of the substrate and changes its value according to the presence of pores, as shown in Figure 2.5a. The nucleation barrier does not exist when the angle between the host material and the Li metal nucleus is equal to zero. If the angle comes close to 180 degrees, in contrast, the heterogeneous nucleation barrier is at its maximum and equals the homogenous nucleation barrier. In summary, the lower the Li

wettability, the greater is the nucleation barrier as well as the critical radius to form nuclei, resulting in dendrite growth.[93]

On the basis of the classical heterogeneous nucleation theory, the lithiophilicity of the anode is quantitively described by the nucleation overpotential. Primarily, the overpotential can be

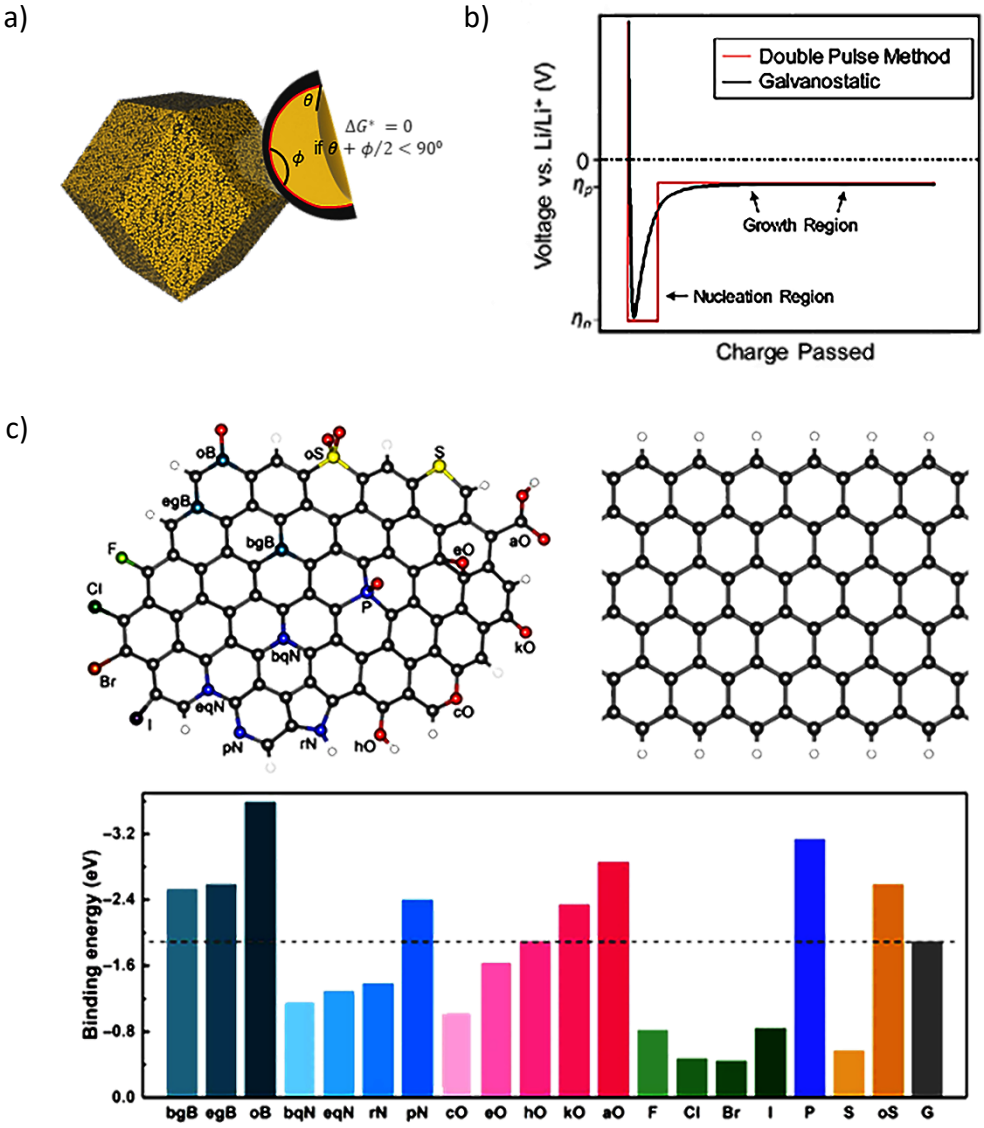

Figure 2.5. a) Schematic illustration of how lithiophilic pores within a suitable host material can store the Li-metal. When the sum of the half angle of the cavity and the contact angle of the nucleus on the substrate is below 90°, the energy barrier will be zero. [15] b) Typical voltage profile of galvanostatic Li deposition (black) and double pulse potentiostatic Li deposition (red). [59] c) Modelling of heteroatom-doped carbon versus pristine graphene model. The bar chart below is a summary of the calculated binding energy between different heteroatom-doped carbons and a Li atom. [91]

divided into three regimes, (Figure 2.5b). The first one is the initial steep fall in the overpotential of nucleation, which indicates the SEI formation. The second regime is the sharp negative spike in the overpotential, which indicates the formation of the Li metal nuclei. The spike indicates the electrochemical supersaturation needed to overcome the nucleation barrier for Li plating. The last regime is when the overpotential rises to a plateau due to the post nucleation growth phase of the Li nuclei. This is because adding a Li adatom to an existing Li nucleus is more favorable and has a lower energy barrier than forming a seed of Li metal. [21,94]

A comprehensive understanding of the lithiophilic nature of heteroatom-doped carbon-based frameworks was demonstrated by a theoretical study conducted by Chen et al. The binding energy between a Li atom and heteroatom-doped carbon was calculated for various cases (Figure 2.5c), including pyrrolic nitrogen (rN), a carboxylic group (aO), graphitic boron on the edge (egB), graphitic boron in the bulk phase (bgB), B-2C-O-type boron (oB), a ketone group (kO), quaternary nitrogen (bqN), quaternary nitrogen on the edge (eqN), pyridinic nitrogen (pN), cyclic oxygen (cO), an epoxy group (eO), a hydroxyl group (hO), F, Cl, Br, I, P, S, and a sulfonyl group (oS).[91] The simulation results suggested three basic principles that could be used to improve the lithiophilicity of the anode substrate, in terms of electronegativity, charge transfer, and local dipoles. The upshot of the study was that the Li ions, acting as a Lewis acid, are strongly attracted to heteroatoms, which act as Lewis base sites owing to their high electronegativity. The functional groups with B, N, and O are found to decrease the Li nucleation overpotential. In contrast, Cl, I, S, F, and Br do not provide high electronegativity toward Li atoms. The second principle includes enhancing the binding energy via co-doping as a strategy to induce a strong local dipole, such as O-S/B/P co-doping. Finally, it was determined that a critical charge transfer above 0.9 e^- is required to increase the binding energy, suggesting that charge transfer has a crucial role during Li nucleation.

2.6. Recent progress on designing carbon-based frameworks (1D, 2D, 3D) and composites

The use of carbon-based frameworks has recently become a highly favorable strategy that can stabilize the electrochemical reactions and enhance the safety of Li metal anodes. In practice, any carbon-based framework needs to exhibit some basic requirements to improve the performance of the anode, including light weight, chemical and mechanical stability, high surface area, large pore volume, sufficient conductivity, and most importantly, lithiophilicity. Understanding the dimensionality of the host material and its corresponding properties is important for constructing a highly efficient anode. This section will discuss the recent progress on utilizing 1D, 2D, and 3D carbon-based frameworks, and their nanocomposites.

2.6.1 1D carbon

2.6.1.1 Carbon fibers

Carbon fibers (CFs) come in a 1D structure with diameters that range from the nano- to the microscale. Besides its outstanding mechanical properties, CFs can be mass-produced in a cost-effective way to facilitate the quantitative integration of electrode materials. The main purpose of employing CFs in the anode is to offer a high surface area that enhances the Li-ion flux. A multifunctional current collector was constructed by Niu et al. that utilized graphitized carbon fibers (GCF) to enlarge the Li storage capacity by intercalation and plating reactions. [95] In addition, using GCF provided a porous structure, which increased the surface area and mitigated volume changes. The enhanced electrochemical performance of this designed anode structure was proved by its large areal capacity of 8 mA h cm^{-2}, high CE of 98 % for 50 cycles, and low nucleation overpotential of 10 mV. (Figure 2.6a) Another approach was adopted by Niu et al., where mesoporous carbon nanofibers were functionalized by amine groups while monitoring the battery stability under practical conditions, as shown in Figure 6b. Interestingly, in this study, it was found that the mesoporous carbon structure and the amine groups facilitated

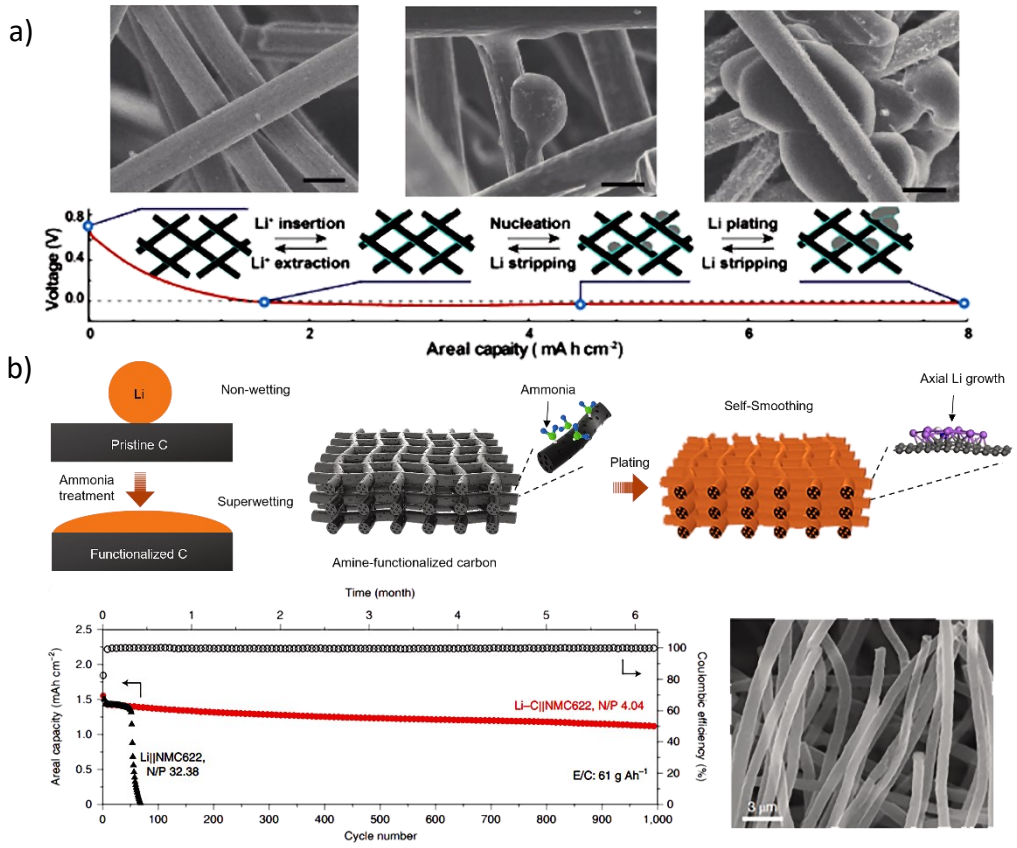

Figure 2.6. a) SEM images showing the morphology of the pristine GCF, intercalated GCF, and GCF charged up to 2 mAh cm^{-2}. The galvanostatic discharge profile with inset schematic diagrams of lithium behavior during cycling is shown below. All scale bars in (a) are 10 µm. [95] b) The schematic illustration on the left shows that the pristine carbon is not Li-wetting, but after being functionalized with heteroatoms, it becomes superwetting. The schematic illustration on the right side shows that, after functionalizing graphitized fiber carbon (GFC) with amine groups, it becomes superwetting, and the Li grows axially. The cycling performance and CE of Li-C||NMC622 and Li||NMC622 cells, demonstrating long-term cycling. An SEM image of amine functionalized GFC shows smooth growth of Li. [96]

the self-smoothing of Li during the deposition process and enabled the carbon hosts to be superwetting towards Li. [96] These results were reflected by the electrochemical performance of the battery, in which the areal capacity was 1.25 mA h cm^{-2} for 1000 cycles at a current density of 1.25 mA cm^{-2}.

2.6.1.2 Carbon nanotubes

Carbon nanotubes (CNTs) have a unique 1D structure that enables fast ion and electron conduction, so that they serve as ideal candidates for anodes that perform under high current densities. The light weight, expandability, and mechanical robustness of the CNT play a significant role in enhancing the reversible capacity of batteries. One research study, conducted by Sun et al., showed the benefits of these properties by using CNT paper as a conductive framework to increase the Li metal storage by 80.7 wt %. [97] The physical and mechanical nature of this sp^2-hybridized carbon framework permitted a high CE of > 97.5 % for 1000 cycles at a current density of 10 mA cm^{-2} and a high areal capacity of 10 mA h cm^{-2} (see Table 1). To enhance the lithiophilicity of their CNT framework, Liu and co-workers introduced oxygen into the CNTs as a doping material (O-CNT). [98] The theoretical and experimental results proved that the ketonic group (C=O) enhances the Li wettability of the anode, which was quantitively measured by its lower nucleation overpotential (35 mV). Moreover, the porous structure of the 3D O-CNT conductive network facilitated Li-ion and electron transport with long-term durability, which was reflected in the electrochemical performance of the battery (see Table 2.1).

Table 2.1. Electrochemical performances of Li-metal anodes utilizing 1D carbon-based frameworks.

Material	Li nucleation overpotential (mV)	Current density (mA cm^{-2})	CE (%)	Cycles	Areal capacity (mA h cm^{-2})
CNT sponge [97]	33.00	1.00	98.5	90	2.00
Oxygen-rich CNT [98]	35.00	1.00	99	200	2.00
CNT paper [108]	-	10.00	97.5	1000	10.00
Amine-doped carbon nanofiber [96]	-	1.56	.	1000	1.56
Graphitized fibers [95]	10.00	0.50	98	50	8.00

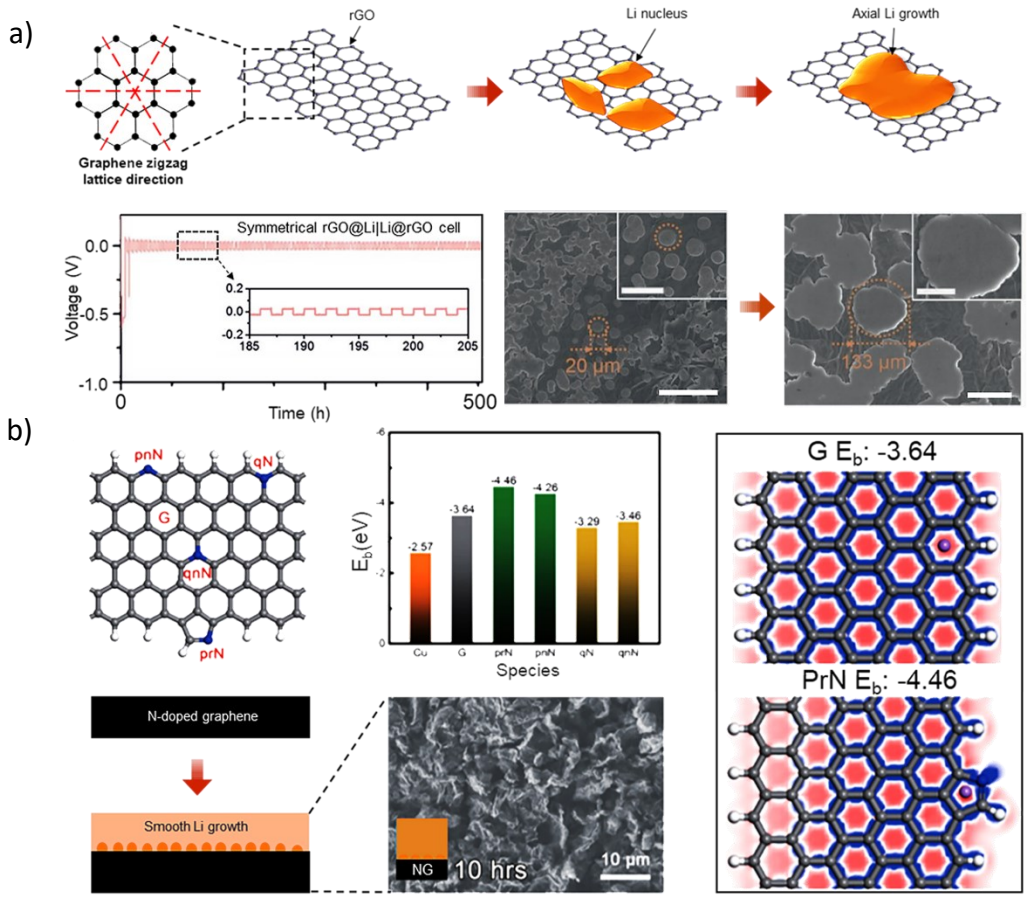

Figure 2.7. a) Schematic illustration of the axial growth of Li on an rGO substrate. The red dashed lines are the graphene zigzag lattice directions. The electrochemical performance of the rGO demonstrates the stability of the symmetrical cell up to 500 hours SEM images of the rGO show the axial growth of the Li metal. Scale bars in (a) are 100 μm and all scale bars in insets are 50 μm. [99] b) Schematic illustration of different doped heteroatoms in the graphene. The middle bar chart illustrates the binding energy calculated between the Li atom and different functional groups. The schematic illustration below and inset SEM image show the smooth Li growth. The right-side schematic shows the total electron density (blue) of isolated atoms on graphene and pyrrolic-N. The red regions indicate less electron density. [100]

2.6.2 2D carbon

Graphene is a 2D monolayer of carbon atoms that are oriented into a hexagonal honeycomb-like lattice, which provides superior electrical conductivity, high surface area, and mechanical flexibility and stability. Therefore, many studies have focused on integrating graphene in LMBs. For example, Li et al. utilized self-assembled reduced graphene oxide (rGO) as a carbon-based framework, owing to its compact layer-by-layer structure and smooth surface.

[99] Interestingly, they obtained epitaxial and dense Li electrodeposition, even at a high current density of 20 mA cm^{-2}. The deposition mechanism behind achieving planar (110) crystallographic planes of Li crystal is related to the in-plane lattice matching between two Li atoms, which have atomic length of 4.96 Å along the (110) plane, and two carbon hexagons, which have length of 4.92 Å in the zigzag direction of graphene (See Figure 2.7a). The performance of the dendrite-free rGO-based anode was demonstrated by its high CE of 99 % for 300 cycles at a current density of 1 mA cm^{-2} and a capacity density of 1 mA h cm^{-2}. Another study, conducted by Zhang et al., designed N-doped graphene as an Li plating matrix to control Li nucleation and inhibit dendritic growth. [100] The pyrrolic nitrogen and pyridinic nitrogen functional groups displayed favorable lithiophilicity due to the relatively small nucleation barrier, which yielded a uniform distribution of the Li metal on the electrode substrate compared to pristine graphene and Cu anodes. Such guided Li nucleation resulted in dendrite-free morphology during cyclic Li plating, and the cell exhibited a high CE of 98 % over nearly 200 cycles (see Figure 2.7b). Additionally, a study was conducted by Liu et al. that utilized CoN_x-doped graphene to obtain high stability and high CE of 99.2 % within 400 cycles. They reported that the existence of CoN_x as heteroatoms in graphene enhanced the adsorption of the Li ions and promoted uniform nucleation as well as smooth Li deposition (see Table 2.2). [109]

Table 2.2. Electrochemical performances of Li-metal anodes utilizing 2D carbon-based frameworks.

Material	Li nucleation overpotential (mV)	Current density (mA cm $^{-2}$)	CE (%)	Cycles	Areal capacity (mA h cm^{-2})
O-doped graphene [91]	15.00	0.50	-	-	-
Reduced graphene oxide [99]	31.20	1.00	99	300	1.00
N-doped graphene [100]	0.36	1.00	98	200	1.00
CoN_x-graphene [109]	-	2.00	99.2	400	2.00

2.6.3 3D carbon

Carbon materials with 3D structures have desirable characteristics in terms of cost-effectiveness, easy synthesis and functionalization, controllable microstructures, electrical conductivity, and high surface area. Thus, this type of carbon structure is considered as one of the most practical candidates for industrial production. Investigations of guiding homogeneous Li plating via 3D carbon frameworks were conducted by Liu et al., who used lightweight, flexible nitrogen-doped graphitic carbon foam (NGCF) *in situ*. [101] The presence of N-containing functional groups, including pyridinic N and pyrrolic N, in the anode design, enabled dendrite-free Li electroplating and enhanced the electrochemical performance even at high areal capacity of 10 mA h cm^{-2}. (See Figure 2.8a) This was evidenced by the low nucleation overpotential (< 25 mV at 3 mA cm^{-2}) and the high CE (99.6 %) for 300 cycles. In another study, Kim et al. utilized Zn/N doped porous carbon framework (PCF), which was derived from ZIF-8, where ZIF is zeolitic imidazolate framework. [102] It was shown that the dispersed Zn facilitated Li plating and enhanced the reversibility of Li storage. More importantly, the cycle test demonstrated stable behavior over 350 cycles, with an areal capacity of 0.2 mA h cm^{-2} (see

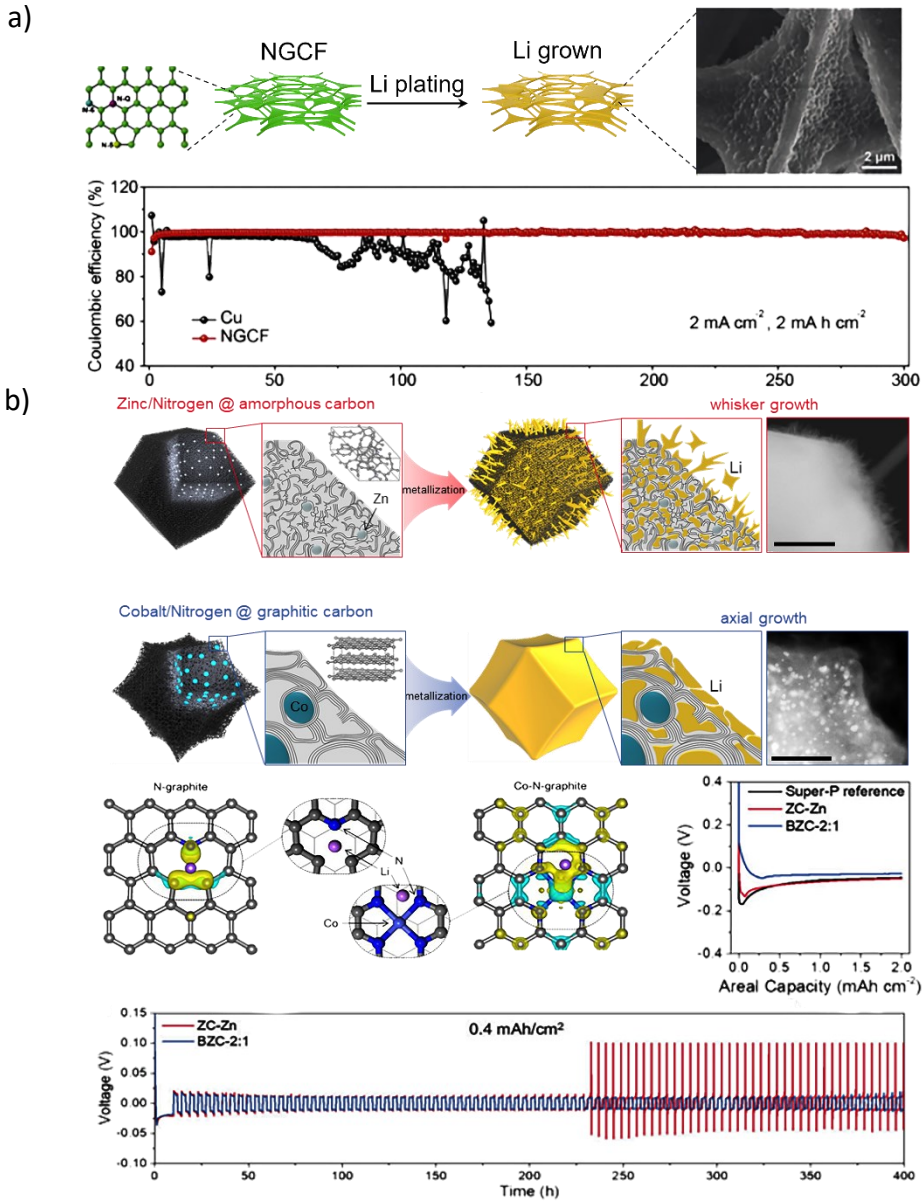

Figure 2.8. a) Schematic illustration of NGCF, with the SEM image showing the smooth Li deposition without dendritic growth. The graph below presents the difference in CE between NGCF and Cu current collector at areal capacity of 2 mAh cm^{-2} during Li plating/stripping. [101] b) Schematic illustration of the Li deposition behaviour on the Zn/N@amorphous carbon and Co/N@graphitic carbon. The transmission electron microscope (TEM) images show the morphology of the Li deposits. The schematic diagram below shows the charge densities and the charge transfer behaviour on the N-doped carbon and Co-N co-doped carbon. The voltage profiles of the Zn/N@amorphous carbon and Co/N@graphitic carbon are on the right, and their cycling performances are at the bottom. Scale bares in (b) are 50 nm. [103]

Table 2.3). Building on the work completed by Kim et al., Lee et al. compared the performance of Zinc/Nitrogen@amorphous carbon and Cobalt/Nitrogen@graphitic carbon to understand the effects of graphitized carbon and doped materials on the electrochemical deposition behavior. [103] The results showed that the Zinc/Nitrogen@amorphous carbon exhibited a relatively less lithiophilic surface and gradually formed an SEI on the Li whiskers. On the other hand, the Cobalt/Nitrogen@graphitic carbon showed a relatively low nucleation barrier due to the uniform distribution of the lithiophilic sites that facilitate the nucleation of Li metal. It was found that the utilization of Co/N co-doped porous carbon can delocalize electrons to the neighboring C atoms, which enhances the electronegativity of the surface and the interaction between the Li^+ and the Co/N doped graphite. The electrochemical performance results indicate 100 % CE for > 100 cycles with an areal capacity of 0.4 mA h cm^{-2} at 0.2 mA cm^{-2}. (See Figure 2.8b)

Table 2.3. Electrochemical performances of Li-metal anodes utilizing 3D carbon-based frameworks.

Material	Li nucleation overpotential (mV)	Current density (mA cm^{-2})	CE (%)	Cycles	Areal capacity (mA h cm^{-2})
N-doped hierarchically porous membranes [110]	0.500	1.00	99	-	2.00
Hollow carbon nanospheres [74]	25.00	0.25	99	150	1.00
N-doped graphitic carbon foams [101]	-	2.00	99.6	300	2.00
Co/N co-doped ZIF-C [103]	-	0.20	100	100	0.40
Zn/N co-doped ZIF-C [102]	24.40	0.50	-	350	0.20

2.6.4 Nanoseed-carbon composites

Despite the ability of carbon materials to react with heteroatoms or functional groups, high current densities remain a challenge in attaining homogeneous Li nucleation with a high Li content and prolonged operational cycles. Realizing more stable Li plating by alloying with other functional materials, such as Ag, Mg, Zn, Au, Si, and Al, is a promising alternative technique. [104,105] These material substrates show a low nucleation barrier to Li plating, since they act as an intermediate buffer layer and can dissolve in Li at specific temperatures. Figure 2.9b displays the nucleation overpotential for different material substrates at which the alloy

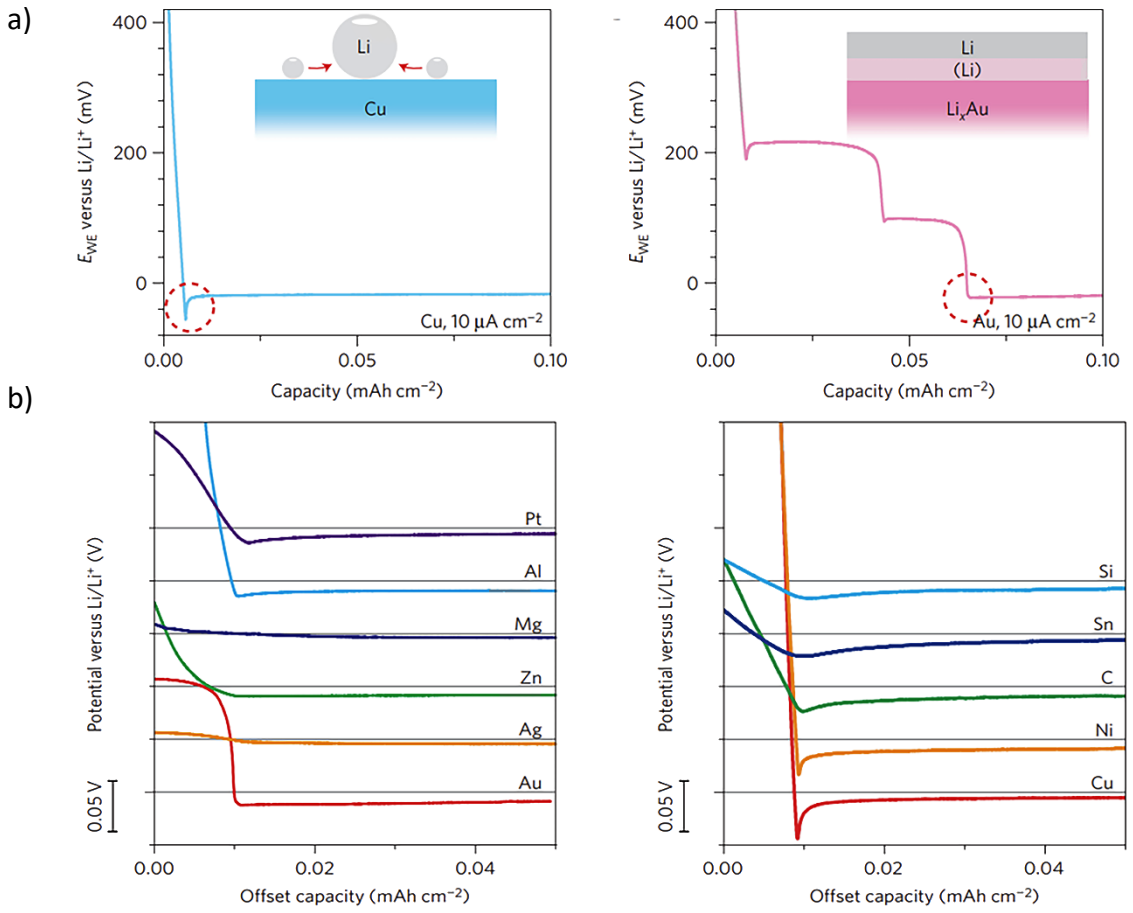

Figure 2.9. a) A voltage profile of galvanostatic Li deposition on a copper substrate at 10 µA cm^{-2}. The inset schematic shows the mechanism of Li nucleation. The right-side voltage profile is of galvanostatic Li deposition on a gold substrate at 10 µA cm^{-2}. The inset schematic diagram demonstrates how the solid solution buffer layer of Au is dissolved in Li and reduces the nucleation energy. [104] b) Voltage profiles of various materials with some Li solubility compared to materials with negligible Li solubility. [104]

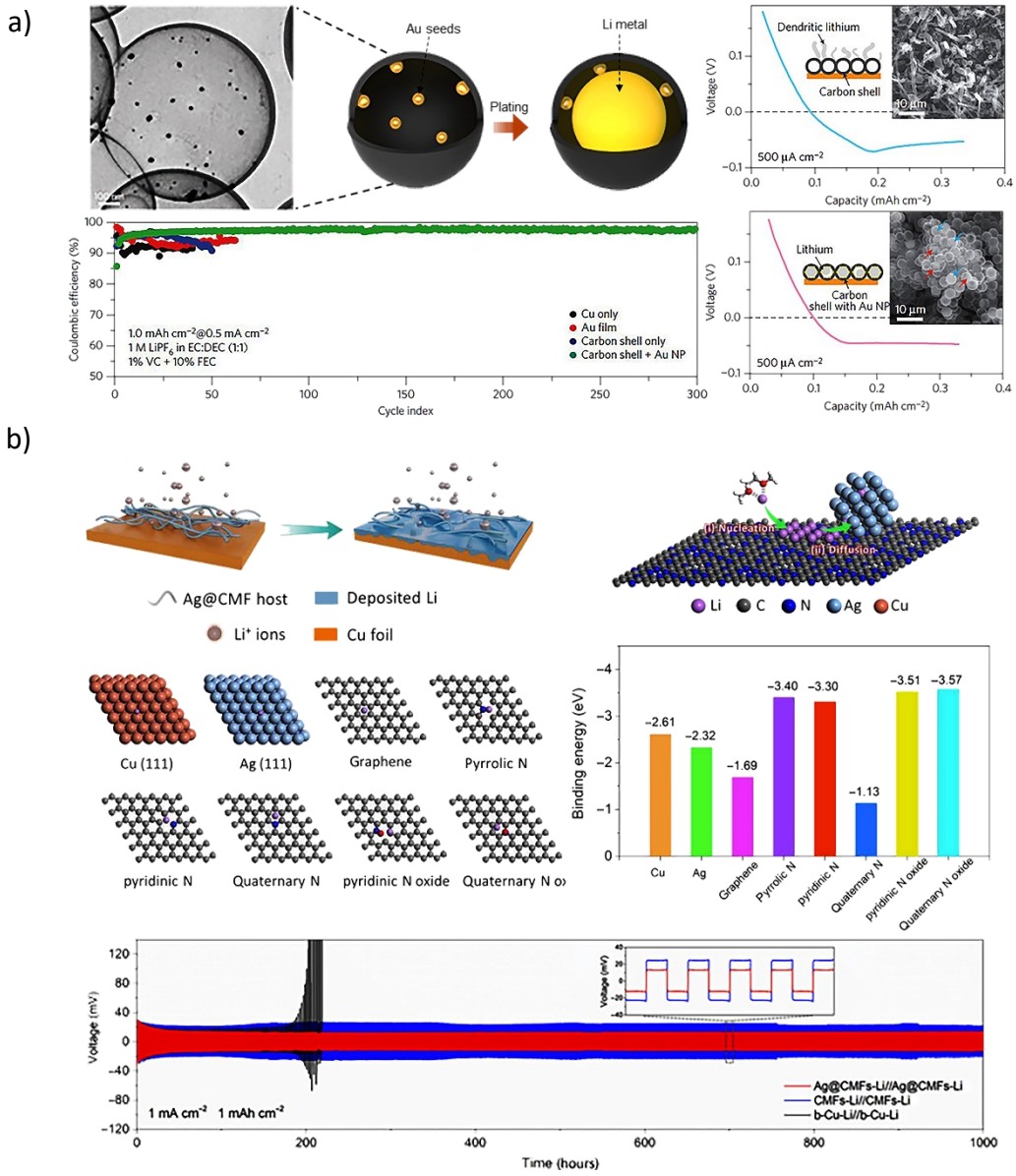

Figure 2.10. a) Schematic illustration and an SEM image that show the Au nanoparticles inside hollow carbon spheres followed by Li growth after cycling. The right-side images present the nucleation overpotential of the hollow carbon. The inset schematics and SEM images show the Au nanoparticles inside the hollow carbon and the smooth Li deposition compared to a carbon shell. Below are the electrochemical performances of different electrodes when cycled in alkyl carbonate electrolyte. Scale bare for TEM in (a) is 100 nm and all scale bares for inset SEM images are 10 μm. [104] b) Schematic illustration showing the Li deposition behaviour on the Ag@CMFs. The schematic on the top right explains the Li deposition process on Ag@CMFs. The middle schematics model the Ag, Cu, graphene, and nitrogen-doped carbons. A summary of the calculated binding energies of Li atom with Cu, Ag, graphene, and nitrogen-doped carbons is also shown (middle right side). The bottom graph shows the electrochemical performances of the Cu, Ag@CMFs and CMFs at 1 mA cm^{-2}. [106]

formation enabled by Ag, Mg, Zn, Au, Si, and Al lowers the overpotential to the minimum compared to Cu, Ni, and C. [104] Owing to this important property, research studies have focused on incorporating these materials in the form of nanoseeds into the carbon-based frameworks. One study, conducted by Yan et al., explored the nucleation pattern of Au nanoseeds encapsulated in hollow carbon spheres to benefit from its crystal lattice matching and solubility in Li. [104] The deposition process demonstrated selective stable encapsulation with improved cycling for more than 300 cycles and a CE of 98 %.

A more recent study done by Fang et al. incorporated Ag nanoparticle–embedded nitrogen-doped carbon macroporous fibers (Ag@CMFs) to enable targeted Li deposition and selective nucleation. [106] The results showed that the small nucleation barrier of the lithiophilic nitrogen-doped carbon was one of the main factors that allowed the formation of homogeneous nucleation sites. In addition, the Ag nanoparticles further enhanced the Li growth and nucleation behavior based on the alloying reaction. The Ag@CMFs therefore allowed dendrite-free Li plating and stripping behavior and exhibited a high CE of > 98 % for more than 500 cycles. Moreover, electrospinning was exploited as a technique to form a flexible MnO nanoparticle/nitrogen (N)-doped polyimide (PI)-based porous carbon nanofiber (MnO–PCNF) film. Yan et al. revealed that the lithiophilic nature of this electrode material enabled the smooth growth of Li during the deposition process. [107] Another advantage was the flexible nature of the interlayer, which accommodated the volume changes of the anode and suppressed the dendritic growth. Furthermore, the conductive structure of MnO–PCNF offered rapid charge transfer, which reduced the electrode polarization. It was reported that the operational lifespan of the battery cycling reached up to 200 cycles at a current density of 1 mA cm^{-2} (see Table 2.4).

Table 2.4. Electrochemical performances of Li-metal anodes utilizing carbon-based nanocomposite frameworks. NPs stands for nanoparticles.

Material	Li nucleation overpotential (mV)	Current density (mA cm $^{-2}$)	CE (%)	Cycles	Areal capacity (mA h cm^{-2})
Au NPs/hollow carbon spheres [104]	20.00	0.50	98	300	1.00
Ag NPs/nitrogen doped carbon [106]	-	1.00	98	800	1.00
MnO NPs/N porous carbon nanofibers [107]	-	1.00	97	200	1.00
ZnO-decorated hierarchical porous carbon [111]	40.00	1.00	97	200	1.00

2.7. Recent progress of utilizing Metal-organic frameworks (MOFs) in Li batteries

After MIL-177 was first applied as an anode material for a Li-ion battery, the possibility of MOFs was confirmed. Since then, various MOF series materials, including MIL-53, MIL-10, HKUST-1, etc., have been used for Li storage applications, see figure 2.11. For each Li storage device, the priority of the characteristics required for the applied material is different, and MOFs have been used for the anode, cathode, separator, and so forth. MOFs are broadly classified into basic pristine MOFs and structures derived from MOFs. Besides direct utilization of pristine MOFs, they can perform as a self-sacrificial template for generating various nanostructured electrode materials. It is one of an effective method to accomplish enhanced electrochemical behavior for various applications. Numerous MOF-derived nanoarchitectures/nanoarchitectonics materials have been reported including nanostructured carbon materials, metal compounds, and their composites. MOFs also show good performance for Li storage, however, MOF-derived materials especially containing carbon components, have great potential as electrode materials owing to the improved electrical conductivity and

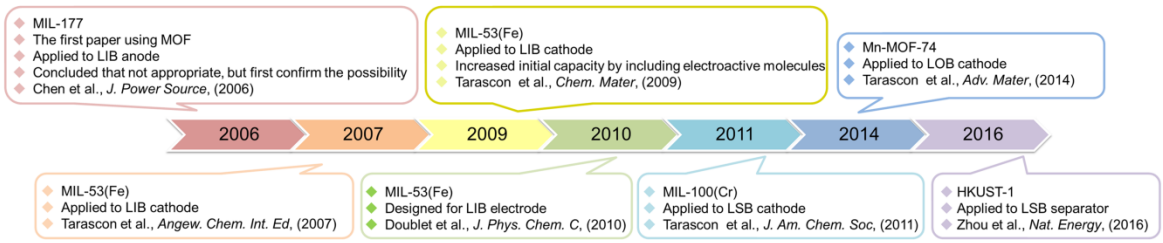

Figure 2.11. A brief history of research on the application of MOFs in Li batteries.

stability. In this section, the latest research will be explained using pristine MOFs and MOF-derived structures applying in LMBs.

The current collector affects the Li anode performance,[112] and depositing Li on an existing current collector leads to the growth of Li dendrites. An electrode modified using MOFs that has good chemical compatibility with Li metal and stable electrochemical properties inhibits the growth of Li dendrites due to its high surface area and abundant polar functional groups. Lin et al. designed an electrode modified with Cu-MOF to inhibit Li dendrite growth.[113] MOF nanosheets were prepared by the hydrothermal method using BDC and cobalt nitrate. The MOF-nanosheet modified electrode (denoted as Cu-MOFs electrode) was fabricated by the simple method of coating the dispersed MOF nanosheets on Cu foil using a doctor blade. In the TEM image of Figure 2.12(a), clear MOF nanosheets can be confirmed. 2D nanosheets facilitate electrolyte adsorption and Li ion adhesion due to their unique structural periodicity, uniform thickness of nanostructures, and exposure of polar functional groups and ligands. The electrochemical stability of the Cu-MOFs electrode was evaluated using CV and linear sweep voltammetry (LSV) methods. Bare Cu electrodes without MOFs were used for comparison. The low current density in the CV and the large electrochemical stability window in the LSV indicate that the Cu-MOFs electrode is more stable towards the electrolyte during the electrochemical cycling, which helps to reduce side reactions. The improved electrolyte absorption capacity of MOF nanosheets can be confirmed by dropping an ether-based electrolyte on the Cu electrode and Cu-MOFs electrode to investigate the contact angles. The

enhanced affinity of the MOF nanosheets reduces the Li^+ concentration gradient and inhibits the growth of dendrites, which in turn allows the electrolyte to remain stable on the electrode surface. Figure 2.12(b) and (c) show the surface and cross-sectional (inset images) morphologies of Li deposited on the bare Cu electrode and Cu-MOFs electrode, respectively. After 5 cycles limited to the capacity of 1 mAh cm^{-2} at a current density of 0.5 mA cm^{-2}, the bare Cu electrode showed a very uneven shape, whereas the Cu-MOFs electrode showed a relatively flat surface. The optical images (inset images in the upper right of Figure 2.12(b) and (c) of Li deposited on these two electrodes also show significant differences. A typical dark gray Li deposit called Elton's gray layer was observed on the bare Cu electrode. Coin-type batteries were used to observe the cycling stability of Li plating/stripping. As shown in Figure 2.12(d), the Cu-MOFs electrode maintained a CE of about 98.4 % for more than 180 cycles under the condition of a lithiation capacity of 1 mAh cm^{-2} and a current density of 2 mA cm^{-2}. On the other hand, the bare Cu electrode exhibits an unstable CE and short cycle life under the same operating condition, representing an inferior electrochemical cycle. The results of this study open the possibility of designing LMBs with high energy density due to the advantages that they offer of high electrolyte absorption, high surface area, polar functional groups, and tuneable pore structure with a high content of MOFs as an electrode modifier.

In addition to the porous and large surface area properties of MOFs, their polar functional groups can induce uniform Li nucleation.[114-119] Wang et al. proposed a dual lithiophilic MOF structure composed of HKUST-1 impregnated with conductive lithiophilic Au nanoparticles (expressed as Ag@HKUST-1) to induce the uniform deposition of Li.[120] Due to the large surface area and abundant O sites of the MOFs, the binding energy for Li is increased, followed by low nucleation overpotentials leading to a uniform distribution of Li nuclei. When Au particles with highly conductive lithiophilic are integrated with MOFs, the binding energy to Li is increases, and the nucleation overpotential approaches almost zero.

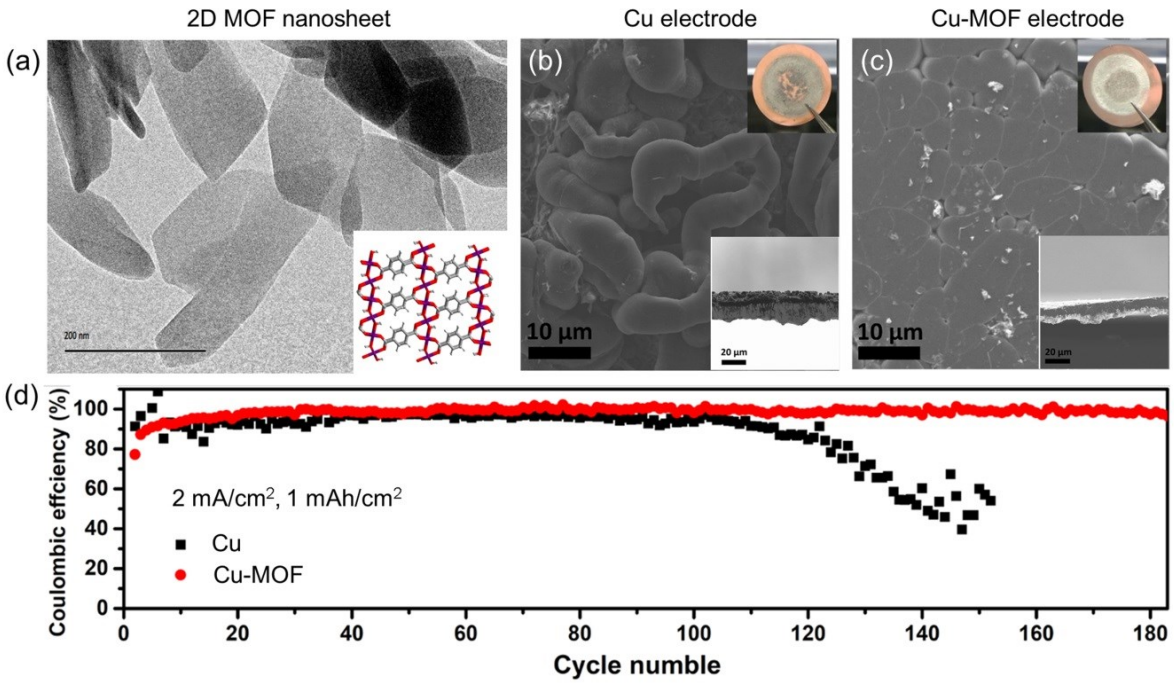

Figure 2.12. (a) TEM image of 2D MOF nanosheet and schematic diagram of the structure. (b) SEM images of the surface and cross-sectional (lower inset) morphologies of bare Cu electrode with 1.0 mAh cm^{-2} Li deposition at a current density of 0.5 mA cm^{-2}. (c) SEM images of the surface and cross-sectional (lower inset) morphologies of Cu-MOF electrode with 1.0 mAh cm^{-2} Li deposition at a current density of 0.5 mA cm^{-2}. The supper insets of c and d are photographs of the electrodes. (d) Cycling performances of bare Cu electrode and Cu-MOFs electrode at the current density of 2 mA cm^{-2} with a lithiation capacity of 1 mAh cm^{-2}.[113]

Consequently, Li plating and stripping of Ag@HKUST-1 substrate exhibited a 97 % of CE and had a high areal capacity of 5 mAh cm^{-2} without the formation of Li dendrites.

Yang et al. reported Li-cMOFs (cMOFs: carbonized MOFs) hybrid 3D anode structures and studied their electrochemical performance.[121] The MOF used in this study was ZIF-8, which is tetrahedrally coordinated by Zn^{2+} and imidazolate, and was transformed into a unique microporous carbon with well-constrained metal clusters after simple heat treatment.[122-124] Carbonized ZIF-8 demonstrated that it was an ideal lithiophilic host for metallic Li, providing that easily molten Li can be implanted into the matrix to form a homogeneous Li carbide MOF (Li-cMOF) hybrid. Since numerous Zn clusters were uniformly dispersed in the matrix and thermodynamically well matched with Li, which can overcome the nucleation barrier, they

acted like pre-planted nucleation seeds, leading to uniform Li deposition. At the same time, the 3D conductive porous structure in ZIF-8 dramatically homogenized the distributions of electric field and Li ion flux, preventing the formation of Li dendrites. In addition, the unlimited volume changes of Li due to plating and stripping could also be well handled by the porous ZIF-8. These characteristics make Li-cMOF a promising rechargeable Li anode material with excellent electrochemical performance, including a very low voltage hysteresis of 29 mV at 1 mA cm^{-2} and a long lifetime of up to 350 cycles.

Similarly, Zhang et al. reported a ZnO/carbon/Li advanced anode using ZIF-8 that provided excellent battery performance.[125] With the help of abundant ZnO, and carbonyl and N-containing surface functional groups, a free-standing and current-collector-free Li electrode in which molten Li was injected into the framework, was created. The structure has two notable advantages. First, the ZnO/carbon framework provides a stable scaffold for Li plating/stripping, greatly alleviating volume changes during cycling at the electrode level. Second, the excellent affinity of the ZnO/carbon framework with a large surface area ensures deposition and infusion of Li during synthesis and cycling. Due to these advantages, the ZnO/carbon/Li electrode shows good stability during cycling, even at a high current density of 10 mA cm^{-2}, which can significantly improve the electrochemical performance.

Recently, Park et al. proposed a dual function for Li storage in a porous carbon host using a ZIF-8-derived porous carbon framework (PCF).[141] Without using other templates, the ZIF-8 product was obtained by a simple method of dissolving and mixing Zn ions and 2-MIM in a solution, and a porous carbon structure was obtained through an easy carbonization process. The obtained porous carbon framework was denoted as PCF, and the product obtained by removing the residual Zn with HCl solution was called PCF-E, respectively. The reason why ZIF-8-based porous carbon material was selected in this study is that it has the following attributes: 1) carbon structure to absorb Li^+, 2) large pore volume to accommodate metallic Li,

3) large surface area to reduce the effective current density, and 4) lithiophilic heteroelements to promote the nucleation kinetics. Based on the atomic model, the Li lattice gap formation energy for the Zn dopant was calculated by DFT, and the results showed that Zn donates excess electrons and further lowers the activation energy for Li adsorption and metallic Li formation, promoting lithiation and metallization of Li. Figure 2.13(a) is a schematic illustration showing dual-phase Li storage in a PCF structure. It can be seen that Li metal is stored in the pores of PCF and that Li ions are intercalated on the PCF surface. The reaction mechanisms are as follows. During charging, Li^+ is inserted into the carbon structure and a lithiation reaction occurs. When PCF is fully lithiated, the surface becomes more lithiophilic, which mainly serves to lower the activation energy for Li adsorption and induce a uniform surface reaction inside the nanopores. The metallization reaction occurs as Li is plated inside the nanopores through the nucleation-growth process after the lithiation process. To confirm the electrochemical behavior, the galvanostatic charge-discharge curves of Super-P, PCF, and PCF-E were investigated. Super-P, which is a conductive and non-porous carbon material was used for comparison. PCF-E with a larger pore volume exhibited high reversibility and low overpotential for Li stripping during subsequent discharge. These results indicate that, in addition to lithiophilic element coordination, the porous structure of PCF is a major factor in accommodating the metallic Li phase. The electrochemical behavior of the metallization reaction was performed for full lithiation after 3 cycles in the voltage range of 0.01 to 2.0 V vs. Li/Li^+, discharging to 0 V vs. Li/Li^+. Then, a constant cathodic current (0.5 mA cm^{-2}) was applied to drive the metallization reaction, and the potential was monitored from that moment until the capacity reached 1.0 mAh cm^{-2}. PCF showed a flat voltage profile with a significant decrease in overpotential during Li plating at the same current density. Figures 2.13(b) and (c) are cross-sectional field emission SEM (FESEM) images of Super-P and PCF-E obtained after charging to 1.0 mAh cm^{-2}. It is clear that Super-P is covered with a thick layer of metallic Li moss-like fibers, whereas in PCF-E there is no Li dendrite growth. The reversibility of Li

plating and stripping processes was determined by characterizing and comparing the cycling performance of Super-P and PCF-based anodes. For the cycling test, the cell was first charged to 2.0 mAh cm^{-2} and cycled at a constant capacity of 0.2 mAh cm^{-2} at 0.2 mA cm^{-2}. In the cycling results shown in Figure 2.13(d), the Li||Super-P cell using Super-P as an electrode showed very high overpotential and CE fluctuation after 88 cycles, suggesting dendritic Li growth or cell failure by Li exhaustion. The Li||PCF-E cell using PCF-E as an electrode showed stable cycling behavior with no signs of failure over 350 cycles. The results of this study showed that MOF-derived PCF can act as a promising metallic Li storage material with dimensional stability, high capacity, and excellent circulation in application to LMBs.

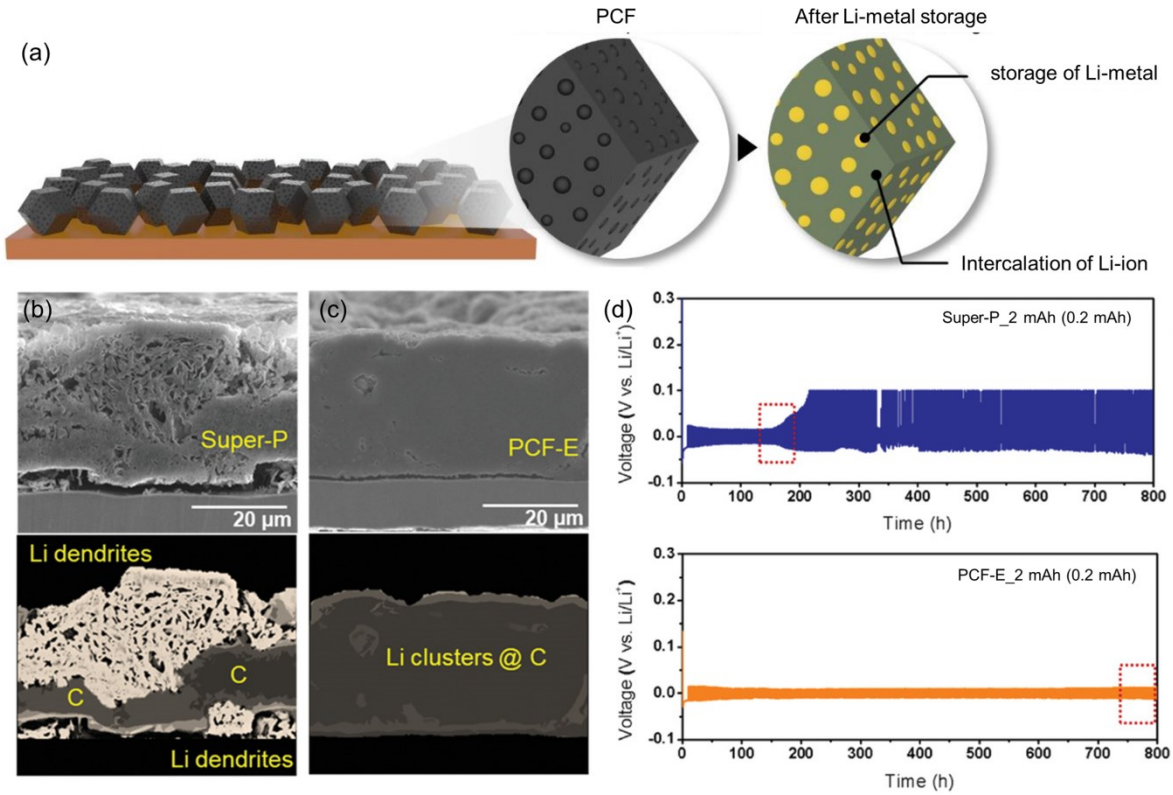

Figure 2.13. (a) Schematic illustration showing dual-phase Li storage in a porous carbon framework (PCF) structure. Li metal is stored in the pores of PCF, and Li ions are intercalated on the PCF surface. (b) Cross-sectional SEM images of Super-P obtained after charging to 1.0 mAh cm^{-2}. (c) Cross-sectional SEM images of PCF-E obtained after charging to 1.0 mAh cm^{-2}. (d) Cycling performances of Super-P and PCF-E at a constant capacity of 0.2 mAh cm^{-2} at 0.2 mA cm^{-2}.[141]

The achievable rate capability and reversible capacity of ZIF-8 is limited, however, in terms of electrolyte access and Li^+ migration by its structural features, which are mainly composed of micropores (< 2 nm). Therefore, the pore structure of the porous material becomes a major factor in determining the electrochemical performance in Li storage, as the Li^+ conduction kinetics in the electrolyte must be considered for effective metallization of Li in a given pore structure.[126, 127] It is also necessary to establish a porous material and an open path with internal pores of appropriate size for homogeneous metallization of Li throughout the electrode. Otherwise, the internal pores will be electrochemically deactivated, eventually resulting in reduced reversible capacity and long-term cyclability. Park et al. created craters on the surfaces of ZIF-8 to secure an open path and investigated the role of the craters in improving the reversibility of plating and peeling when using ZIF-8 as a host for LMBs.[128] First, poly(vinylpolypyrrolidone) (PVP, $(C_6H_9NO)_n$) was dissolved in deionized (DI) water, and colloidal silica (SiO_2) solution was added to the PVP solution under stirring for 24 hours. Then, a solution of zinc acetate dihydrate and 2-MIM dissolved in DI water as precursors were mixed with a PVP-SiO_2 solution and maintained without stirring. The precipitate was collected, washed, dried, and then the resulting powder was heat-treated in an Ar atmosphere. After etching with hydrofluoric acid solution to remove chemical residues, washing and drying were performed to obtain the final product. The structure without surface craters was named PCF, and the structure with surface craters was named SC-PCF. The surface structures of PCF and SC-PCF are shown in Figure 2.14(a). The surface of SC-PCF, which is cratered due to silica particles, shows noticeable morphological changes and large pores are formed. PCF particles with surface craters have a typical amorphous carbon structure, and various chemical states of N exist, such as quaternary N, pyrrolic N, and pyridinic N, which play an key role in stable Li metal formation. The function of surface craters in modulating the Li storage response was analyzed using two different AC impedance measurements. From the impedance results, the MacMullin number (N_M) was estimated for both PCF electrodes, as shown in Figure 2.14(b).

N_M is defined as the ratio of the ionic conductivity (κ) of an electrolyte solution to the effective ionic conductivity (κ_{eff}) of an electrolyte-filled porous electrode, and indicates how effectively ions are transported through the electrode.[129] The N_M value of SC-PCF was estimated to be 2.18 and that of PCF to be 4.47, which means that the integration of surface craters in SC-PCF helps to provide robust pathways for facile Li^+ transport through the electrode. PCFs are mainly composed of micropores, which provide a narrow path for the movement of Li^+, resulting in high ionic resistance. This prevents the transport of Li^+ deep into the pores, causing preferential plating of Li at the pore orifice, which provides only limited utilization of the internal pores during charge the process. SC-PCF regulates Li^+ transport by reducing ionic resistance through the electrode due to the craters on the particle surfaces, while also allowing Li^+ to migrate into the internal pores to be plated. When the inner pores are filled with Li, the surface craters provide additional space for Li storage, allowing efficient use of both the inner pores and the surface craters, and enhancing the reversibility of Li plating and stripping. To clarify the role of surface craters for Li storage, the results for the electrochemical behavior during Li plating and stripping of PCF and SC-PCF are shown in Figure 2.13(c). Both the PCF and the SC-PCF electrodes were galvanostatically charged to an areal capacity of 2 mAh cm^{-2} with a current density of 0.2 mA cm^{-2}. They were initially lithiated (> 0 V vs. Li/Li^+) during charging (Li plating) and then metallic Li (< 0 V vs. Li/Li^+) was plated into the internal pores. During discharging (Li stripping), PCF and SC-PCF exhibited different behavior, and the initial CE of SC-PCF electrode was ~ 90.5 %, much higher than that of PCF (~ 72.7 %) because a larger amount of Li was removed from the SC-PCF electrode. This is because more of the pore space of the SC-PCF was effectively utilized as a reservoir for metallic Li during cycling. In conclusion, the full cell composed of PCF anode with surface craters introduced noticeable improvements in speed and cycling performance compared to the original PCF full cell. This demonstrates that tuning the surface structure of PCFs can be novel strategy to enhance the electrochemical performance and cycle life of advanced host materials for LMBs.

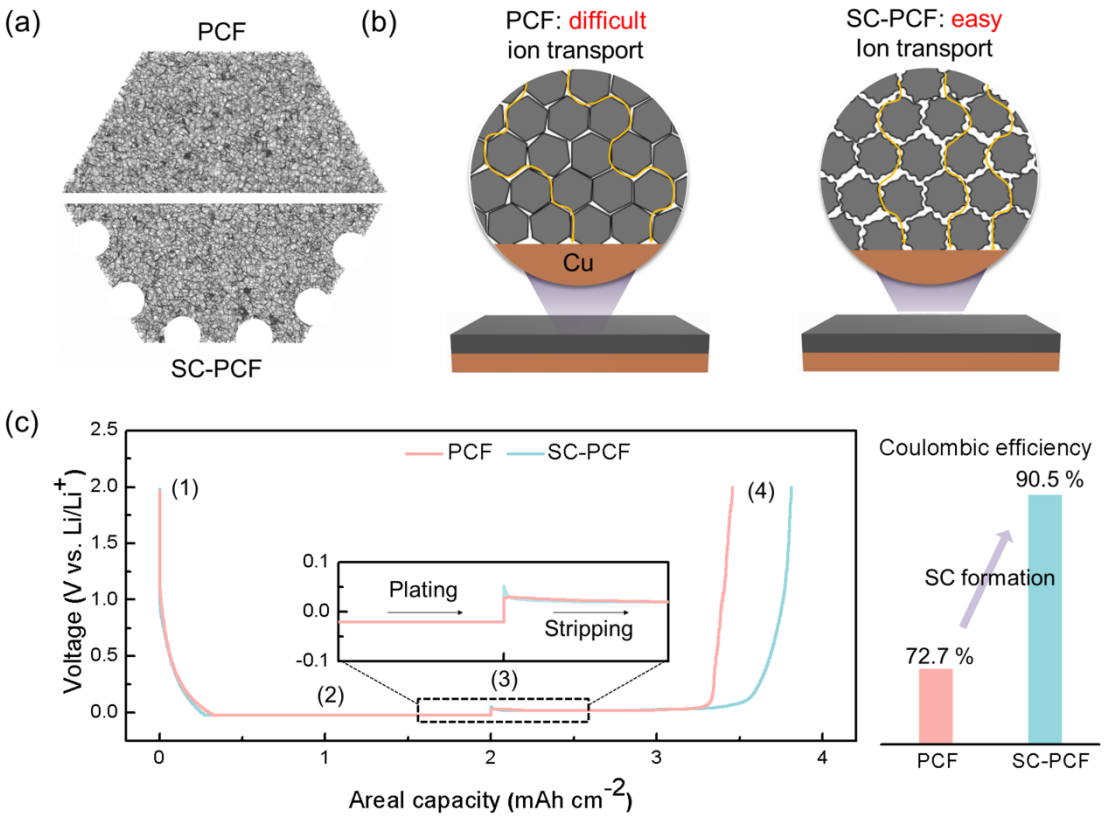

Figure 2.14. (a) Surface structures of porous carbon framework (PCF) and structure with surface craters (SC-PCF). (b) Schematic illustrations showing the ion transport, which was used to calculate the MacMullin numbers of PCF and SC-PCF electrodes. (c) The Li plating and stripping behavior of PCF and SC-PCF electrodes.[128]

The Zn atoms, which are metal ions constituting ZIF-8, play a role in promoting stable Li metal formation in the host by increasing lipophilicity. Moreover, dual-phase lithiation and metallization can be realized in a single anode electrode, enabling a large amount of Li storage. Reinforcing weaknesses such as less stable surface chemistry causing dead-Li growth, however, still remains a challenge to be solved. Kim et al. proposed a structure in which Co nanoparticles are embedded in a porous N-doped graphite material derived from ZIF-8 as part of a study to improve this.[126]

All the results based on using the porous carbon obtained from ZIF-8 as host material confirmed that it suppresses volume expansion as it does not form Li dendrites during Li plating/stripping. Furthermore, they showed that N and Zn (or ZnO) nanoparticles within the host structure had

enhanced affinity with Li and caused favorable nucleation and stable growth of Li metal. In conclusion, the ZIF-derived carbon hosts showed dramatically improved cycling performance compared to Li metal or non-porous carbon materials. So far, more than 30,000 MOFs with various structures and properties composed of different metal ions or clusters and ligands have been reported, which show tremendous potential to obtain carbonized composites that can be used as templates or precursors.

Metals, metal oxides, and metal sulfides act as lithiophilic sites for Li nucleation and deposition. In addition to constructing a standalone carbonized MOF anode, other methods such as hot-pressing methods can be used to introduce MOFs into the network.[130, 131] The introduction of electrolyte additives can improve the cycling stability of LMBs,[132-133] and several MOFs have been proposed for this purpose. The introduction of the additive usually results from the *in-situ* formation of a strong but thin SEI when the degradable additive comes into contact with Li, as is the case with $LiNO_3$ and fluoroethylene carbonate.[142, 143] Because sufficient porosity and thin-grain self-assembly are important in electrolyte fillers,[135] the search for flexible or modifiable additives that are full of multi-scale pores, functional groups, or building blocks is essential for the advancement of Li metal anodes. Additives are used to protect the anode by reacting with Li to form an SEI layer, and to inhibit the growth of Li dendrite.[136] Li et al. proposed three MOFs (UiO-66, HKUST-1, NH_2-MIL-101) as electrolyte solid additives to inhibit the growth of Li dendrite.[137] The MOF-based additives were synthesized by mixing with common carbonate electrolytes. Among them, Zr-based MOF additives (UiO-66) had the best electrical conductivity compared to other Cu-based MOFs (HKUST-1) and Al-based MOFs (NH_2-MIL-101). The system with UiO-66 enabled very long cycling of Li plating/stripping with a small voltage gap of 75–150 mV up to 1400 hours at an areal capacity of 1.5 mAh cm^{-2}, based on a Li-Li symmetric cell. The robustness, porosity and electrochemical stability of the MOF additives promote the concentration of LiF in the SEI to reduce unwanted

side reactions. It makes an important contribution to good Li anode performance by homogenizing the distribution and size of the Li^+ flux and suppressing the extrusion of Li deposits. Table 2.5 summarizes the studies where MOFs were applied as host materials for LMBs. [138-140]

Table 2.5. Summary of recent studies in which MOFs or MOF derived materials were applied as host materials for LMBs

MOF	Application part	Reversible capacity (mAh g^{-1})	Cycle number
Ag@HKUST-1 [120]	Host material	-	300
ZIF-8 [121]	Host material	-	350
ZIF-8 [125]	Host material	-	200
ZIF-8 [141]	Host material	-	350
ZIF-8 [128]	Host material	991	120
Bimetallic ZIF [126]	Host material	-	200

2.8. Summary

Li-metal suffers from severe drawbacks that hinder its usage in practical applications, including unstable or uneven SEI formation of dead Li during plating and stripping processes, dendrite growth, and volume changes. These lead to serious issues, such as short-circuiting, low CE, capacity loss, and safety complications. Understanding the principles and mechanism of dendrite growth is necessary to build up our knowledge and enable us to design a new safe anode for Li metal batteries. In this chapter, we have summarized the main principles, including light weight, chemical and mechanical stability, high surface area, large pore volume, sufficient conductivity, and most importantly, lithiophilicity, to utilize porous carbon-based frameworks as Li host materials as a solution, as shown in Figure 2.15. In addition, understanding the dimensionality of the host materials and their corresponding properties is important for constructing a highly efficient anode, so we have discussed the recent progress on utilizing 1D, 2D, and 3D carbon-based

frameworks and their nanocomposites. Finally, we summarized the recent progress of the practical design of MOF electrodes for realizing highly reliable LMBs.

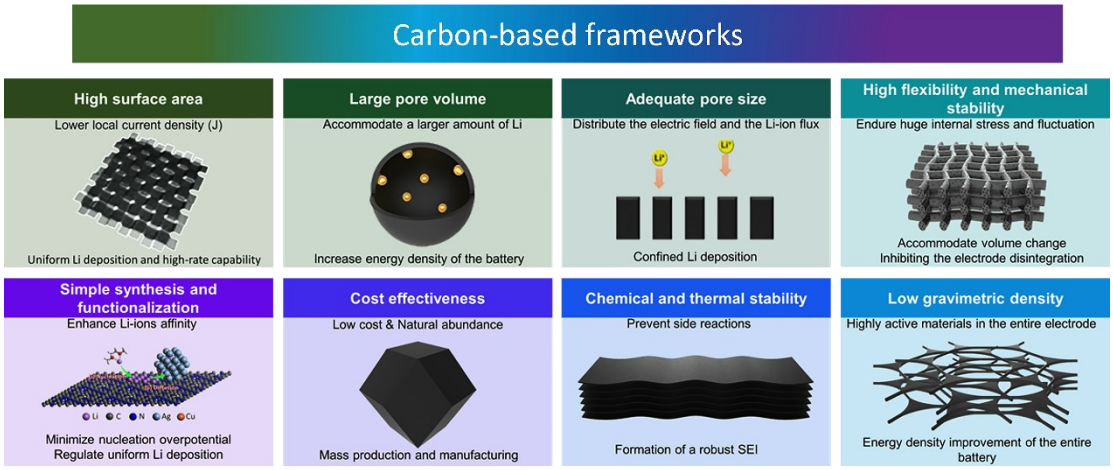

Figure 2.15. Schematic summary of the main properties of carbon-based frameworks and their corresponding advantages.

2.9. References

[1] Asl HY, Manthiram A. Toward sustainable batteries. Nature Sustainability. 2021;4(5):379-380.

[2] Dell RM, Rand DAJ. Energy storage a key technology for global energy sustainability. Journal of power sources. 2001;100(1-2):2-17.

[3] Hannan MA, Hoque MM, Mohamed A, et al. Review of energy storage systems for electric vehicle applications: Issues and challenges. Renewable and Sustainable Energy Reviews. 2017 2017/03/01/;69:771-789.

[4] Perumal P, Andersen SM, Nikoloski A, et al. Leading strategies and research advances for the restoration of graphite from expired Li+ energy storage devices. Journal of Environmental Chemical Engineering. 2021;9(6):106455.

[5] Mrozik W, Rajaeifar MA, Heidrich O, et al. Environmental impacts, pollution sources and pathways of spent lithium-ion batteries. Energy & Environmental Science. 2021.

[6] Dunn B, Kamath H, Tarascon J-M. Electrical energy storage for the grid: a battery of choices. Science. 2011;334(6058):928-935.

[7] Wang Y, Zhang W, Chen L, et al. Quantitative description on structure–property relationships of Li-ion battery materials for high-throughput computations. Science and Technology of advanced MaTerialS. 2017;18(1):134-146.

[8] Ding Y, Cano ZP, Yu A, et al. Automotive Li-ion batteries: current status and future perspectives. Electrochemical Energy Reviews. 2019;2(1):1-28.

[9] Sun P, Bisschop R, Niu H, et al. A review of battery fires in electric vehicles. Fire technology. 2020:1-50.

[10] Liu J, Gu T, Sun X, et al. Synthesis of MnO/C/Co3O4 nanocomposites by a Mn2+-oxidizing bacterium as a biotemplate for lithium-ion batteries. Science and Technology of Advanced Materials. 2021;22(1):429-440.

[11] Jehnichen P, Wedlich K, Korte C. Degradation of high-voltage cathodes for advanced lithium-ion batteries–differential capacity study on differently balanced cells. Science and technology of advanced materials. 2019;20(1):1-9.

[12] Baik JM, Lee JP. Strategies for ultrahigh outputs generation in triboelectric energy harvesting technologies: from fundamentals to devices. Science and technology of advanced materials. 2019;20(1):927-936.

[13] Kim JH. Focus on nanogenerators: toward smart wearable devices. Science and Technology of Advanced Materials. 2020;21(1):422-423.

[14] Han SA, Lee JH, Seung W, et al. Patchable and implantable 2D nanogenerator. Small. 2021;17(9):1903519.

[15] Hyeon Y, Lee J, Qutaish H, et al. Lithium metal storage in zeolitic imidazolate framework derived nanoarchitectures. Energy Storage Materials. 2020.

[16] Shin HR, Yun J, Eom GH, et al. Mechanistic and Nanoarchitectonics Insight into Li–Host Interactions in Carbon Hosts for Reversible Li Metal Storage. Nano Energy. 2022:106999.

[17] Ghazi ZA, Sun Z, Sun C, et al. Key aspects of lithium metal anodes for lithium metal batteries. Small. 2019;15(32):1900687.

[18] Pathak R, Chen K, Wu F, et al. Advanced Strategies for the Development of Porous Carbon as a Li Host/Current Collector for Lithium Metal Batteries. Energy Storage Materials. 2021.

[19] Kang J-H, Lee J, Jung J-W, et al. Lithium–Air Batteries: Air-Breathing Challenges and Perspective. ACS nano. 2020;14(11):14549-14578.

[20] Ye H, Zhang Y, Yin Y-X, et al. An outlook on low-volume-change lithium metal anodes for long-life batteries. ACS Central Science. 2020;6(5):661-671.

[21] Liu W, Liu P, Mitlin D. Tutorial review on structure–dendrite growth relations in metal battery anode supports. Chemical Society Reviews. 2020;49(20):7284-7300.

[22] Zhang C, Huang Z, Lv W, et al. Carbon enables the practical use of lithium metal in a battery. Carbon. 2017;123:744-755.

[23] Wang J, Xu Y, Ding B, et al. Confined self-assembly in two-dimensional interlayer space: monolayered mesoporous carbon nanosheets with in-plane orderly arranged mesopores and a highly graphitized framework. Angewandte Chemie International Edition. 2018;57(11):2894-2898.

[24] Wang X-B, Jiang X-F, Bando Y. Blowing route towards advanced inorganic foams. Bulletin of the Chemical Society of Japan. 2019;92(1):245-263.

[25] Salunkhe RR, Tang J, Kamachi Y, et al. Asymmetric supercapacitors using 3D nanoporous carbon and cobalt oxide electrodes synthesized from a single metal–organic framework. ACS nano. 2015;9(6):6288-6296.

[26] Tang J, Salunkhe RR, Zhang H, et al. Bimetallic metal-organic frameworks for controlled catalytic graphitization of nanoporous carbons. Scientific reports. 2016;6(1):1-8.

[27] Lee J-H, Kim J, Kim TY, et al. All-in-one energy harvesting and storage devices. Journal of Materials Chemistry A. 2016;4(21):7983-7999.

[28] Salunkhe RR, Kaneti YV, Kim J, et al. Nanoarchitectures for metal–organic framework-derived nanoporous carbons toward supercapacitor applications. Accounts of chemical research. 2016;49(12):2796-2806.

[29] Zhang X, Wang A, Liu X, et al. Dendrites in lithium metal anodes: suppression, regulation, and elimination. Accounts of chemical research. 2019;52(11):3223-3232.

[30] Yan X, Lin L, Chen Q, et al. Multifunctional roles of carbon-based hosts for Li-metal anodes: A review. Carbon Energy. 2021.

[31] Liu Y, Li X, Fan L, et al. A review of carbon-based materials for safe lithium metal anodes. Frontiers in chemistry. 2019;7:721.

[32] Tang K, Xiao J, Li X, et al. Advances of carbon-based materials for lithium metal anodes. Frontiers in chemistry. 2020:931.

[33] Han W, Li Q, Zhu H, et al. Hierarchical Porous Graphene Bubbles as Host Materials for Advanced Lithium Sulfur Battery Cathode. Frontiers in chemistry. 2021;9:171.

[34] Guan X, Wang A, Liu S, et al. Controlling nucleation in lithium metal anodes. Small. 2018;14(37):1801423.

[35] Li B, Wang Y, Yang S. A material perspective of rechargeable metallic lithium anodes. Advanced Energy Materials. 2018;8(13):1702296.

[36] Guo Y, Li H, Zhai T. Reviving lithium-metal anodes for next-generation high-energy batteries. Advanced materials. 2017;29(29):1700007.

[37] Li L, Li S, Lu Y. Suppression of dendritic lithium growth in lithium metal-based batteries. Chemical communications. 2018;54(50):6648-6661.

[38] Gao M, Li H, Xu L, et al. Lithium metal batteries for high energy density: Fundamental electrochemistry and challenges. Journal of Energy Chemistry. 2021;59:666-687.

[39] Vu TT, Kim BG, Kim JH, et al. Suppression of dendritic lithium-metal growth through concentrated dual-salt electrolyte and its accurate prediction. Journal of Materials Chemistry A. 2021;9(40):22833-22841.

[40] Xu W, Wang J, Ding F, et al. Lithium metal anodes for rechargeable batteries. Energy & Environmental Science. 2014;7(2):513-537.

[41] Um JH, Yu SH. Unraveling the mechanisms of lithium metal plating/stripping via in situ/operando analytical techniques. Advanced Energy Materials. 2021;11(27):2003004.

[42] Zhang J-G, Xu W, Henderson WA. Characterization and modeling of lithium dendrite growth. Lithium Metal Anodes and Rechargeable Lithium Metal Batteries: Springer; 2017. p. 5-43.

[43] Hagopian A, Doublet M-L, Filhol J-S. Thermodynamic origin of dendrite growth in metal anode batteries. Energy & Environmental Science. 2020;13(12):5186-5197.

[44] Han SA, Qutaish H, Park MS, et al. Strategic approaches to the dendritic growth and interfacial reaction of lithium metal anode. Chemistry–An Asian Journal. 2021;16(24):4010-4017.

[45] Li Z, Huang J, Liaw BY, et al. A review of lithium deposition in lithium-ion and lithium metal secondary batteries. Journal of power sources. 2014;254:168-182.

[46] Steiger J, Kramer D, Mönig R. Mechanisms of dendritic growth investigated by in situ light microscopy during electrodeposition and dissolution of lithium. Journal of Power Sources. 2014;261:112-119.

[47] Brissot C, Rosso M, Chazalviel JN, et al. In Situ Concentration Cartography in the Neighborhood of Dendrites Growing in Lithium/Polymer-Electrolyte/Lithium Cells. Journal of the Electrochemical Society. 1999;146(12):4393.

[48] Brissot C, Rosso M, Chazalviel J-N, et al. Concentration measurements in lithium/polymer–electrolyte/lithium cells during cycling. Journal of power sources. 2001;94(2):212-218.

[49] Brissot C, Rosso M, Chazalviel J-N, et al. Dendritic growth mechanisms in lithium/polymer cells. Journal of power sources. 1999;81:925-929.

[50] Fleury V, Chazalviel J-N, Rosso M. Coupling of drift, diffusion, and electroconvection, in the vicinity of growing electrodeposits. Physical Review E. 1993;48(2):1279.

[51] Rosso M, Gobron T, Brissot C, et al. Onset of dendritic growth in lithium/polymer cells. Journal of power sources. 2001;97:804-806.

[52] Rosso M, Brissot C, Teyssot A, et al. Dendrite short-circuit and fuse effect on Li/polymer/Li cells. Electrochimica Acta. 2006;51(25):5334-5340.

[53] Cheng J-H, Assegie AA, Huang C-J, et al. Visualization of lithium plating and stripping via in operando transmission X-ray microscopy. The Journal of Physical Chemistry C. 2017;121(14):7761-7766.

[54] Bai P, Guo J, Wang M, et al. Interactions between lithium growths and nanoporous ceramic separators. Joule. 2018;2(11):2434-2449.

[55] Choudhury S. The many shapes of lithium. Joule. 2018;2(11):2201-2203.

[56] Monroe C, Newman J. Dendrite growth in lithium/polymer systems: A propagation model for liquid electrolytes under galvanostatic conditions. Journal of The Electrochemical Society. 2003;150(10):A1377.

[57] Monroe C, Newman J. The effect of interfacial deformation on electrodeposition kinetics. Journal of The Electrochemical Society. 2004;151(6):A880.

[58] Ely DR, García RE. Heterogeneous nucleation and growth of lithium electrodeposits on negative electrodes. Journal of the Electrochemical Society. 2013;160(4):A662.

[59] Pei A, Zheng G, Shi F, et al. Nanoscale nucleation and growth of electrodeposited lithium metal. Nano letters. 2017;17(2):1132-1139.

[60] Barai P, Higa K, Ngo AT, et al. Mechanical stress induced current focusing and fracture in grain boundaries. Journal of The Electrochemical Society. 2019;166(10):A1752.

[61] Aslam MK, Niu Y, Hussain T, et al. How to avoid dendrite formation in metal batteries: Innovative strategies for dendrite suppression. Nano Energy. 2021:106142.

[62] Schweikert N, Hofmann A, Schulz M, et al. Suppressed lithium dendrite growth in lithium batteries using ionic liquid electrolytes: Investigation by electrochemical impedance spectroscopy, scanning electron microscopy, and in situ 7Li nuclear magnetic resonance spectroscopy. Journal of Power Sources. 2013;228:237-243.

[63] Cui J, Yao S, Ihsan-Ul-Haq M, et al. Correlation between Li plating behavior and surface characteristics of carbon matrix toward stable Li metal anodes. Advanced Energy Materials. 2019;9(1):1802777.

[64] Zhang R, Cheng XB, Zhao CZ, et al. Conductive nanostructured scaffolds render low local current density to inhibit lithium dendrite growth. Advanced Materials. 2016;28(11):2155-2162.

[65] Jiang R, Diao W, Xie D, et al. N-doped Porous Host with Lithiophilic Co Nanoparticles Implanted into 3D Carbon Nanotubes for Dendrite-Free Lithium Metal Anodes. ACS Applied Energy Materials. 2021;4(11):12871-12881.

[66] Farha OK, Eryazici I, Jeong NC, et al. Metal–organic framework materials with ultrahigh surface areas: is the sky the limit? Journal of the American Chemical Society. 2012;134(36):15016-15021.

[67] Qutaish H, Lee J, Hyeon Y, et al. Design of cobalt catalysed carbon nanotubes in bimetallic zeolitic imidazolate frameworks. Applied Surface Science. 2021;547:149134.

[68] Liu Y, Xu X, Sadd M, et al. Insight into the Critical Role of Exchange Current Density on Electrodeposition Behavior of Lithium Metal. Advanced Science. 2021;8(5):2003301.

[69] Tao R, Bi X, Li S, et al. Kinetics tuning the electrochemistry of lithium dendrites formation in lithium batteries through electrolytes. ACS applied materials & interfaces. 2017;9(8):7003-7008.

[70] Cheng Y, Chen J, Chen Y, et al. Lithium Host: Advanced Architecture Components for Lithium Metal Anode. Energy Storage Materials. 2021.

[71] Jeong J, Chun J, Lim W-G, et al. Mesoporous carbon host material for stable lithium metal anode. Nanoscale. 2020;12(22):11818-11824.

[72] Zhang Y, Liu B, Hitz E, et al. A carbon-based 3D current collector with surface protection for Li metal anode. Nano Research. 2017;10(4):1356-1365.

[73] Geng H, Peng Y, Qu L, et al. Structure Design and Composition Engineering of Carbon-Based Nanomaterials for Lithium Energy Storage. Advanced Energy Materials. 2020;10(10):1903030.

[74] Zheng G, Lee SW, Liang Z, et al. Interconnected hollow carbon nanospheres for stable lithium metal anodes. Nature nanotechnology. 2014;9(8):618-623.

[75] Liu F, Xu R, Hu Z, et al. Regulating lithium nucleation via CNTs modifying carbon cloth film for stable Li metal anode. Small. 2019;15(5):1803734.

[76] Evers S, Nazar LF. New approaches for high energy density lithium–sulfur battery cathodes. Accounts of chemical research. 2013;46(5):1135-1143.

[77] Kuang Y, Chen C, Kirsch D, et al. Thick electrode batteries: principles, opportunities, and challenges. Advanced Energy Materials. 2019;9(33):1901457.

[78] Choi SH, Hyeon Y, Shin HR, et al. Critical role of surface craters for improving the reversibility of Li metal storage in porous carbon frameworks. Nano Energy. 2021:106243.

[79] Nanda S, Gupta A, Manthiram A. Anode-free full cells: a pathway to high-energy density lithium-metal batteries. Advanced Energy Materials. 2021;11(2):2000804.

[80] Li Y, Guo S. Material design and structure optimization for rechargeable lithium-sulfur batteries. Matter. 2021;4(4):1142-1188.

[81] Chi S-S, Wang Q, Han B, et al. Lithiophilic Zn sites in porous CuZn alloy induced uniform Li nucleation and dendrite-free Li metal deposition. Nano letters. 2020;20(4):2724-2732.

[82] Sun Z, Jin S, Jin H, et al. Robust expandable carbon nanotube scaffold for ultrahigh-capacity lithium-metal anodes. Advanced Materials. 2018;30(32):1800884.

[83] Roberts AD, Li X, Zhang H. Porous carbon spheres and monoliths: morphology control, pore size tuning and their applications as Li-ion battery anode materials. Chemical Society Reviews. 2014;43(13):4341-4356.

[84] Shen L, Shi P, Hao X, et al. Progress on lithium dendrite suppression strategies from the interior to exterior by hierarchical structure designs. Small. 2020;16(26):2000699.

[85] Lin D, Liu Y, Cui Y. Reviving the lithium metal anode for high-energy batteries. Nature nanotechnology. 2017;12(3):194-206.

[86] Zhang Y, Zuo T-T, Popovic J, et al. Towards better Li metal anodes: challenges and strategies. Materials Today. 2020;33:56-74.

[87] Jiang H, Dong Q, Bai M, et al. A 3D-mixed ion/electron conducting scaffold prepared by in situ conversion for long-life lithium metal anodes. Nanoscale. 2021;13(5):3144-3152.

[88] Yun J, Park B-K, Won E-S, et al. Bottom-up lithium growth triggered by interfacial activity gradient on porous framework for lithium-metal anode. ACS Energy Letters. 2020;5(10):3108-3114.

[89] Park KH, Kang DW, Park J-W, et al. Modulating the electrical conductivity of a graphene oxide-coated 3D framework for guiding bottom-up lithium growth. Journal of Materials Chemistry A. 2021;9(3):1822-1834.

[90] Lee J, Park M-S, Kim JH. Stabilizing Li-metal host anode with LiF-rich solid electrolyte interphase. Nano Convergence. 2021;8(1):1-8.

[91] Chen X, Chen X-R, Hou T-Z, et al. Lithiophilicity chemistry of heteroatom-doped carbon to guide uniform lithium nucleation in lithium metal anodes. Science Advances. 2019;5(2):eaau7728.

[92] Tarascon JM, Armand M. Issues and challenges facing rechargeable lithium batteries. Nature. 2001 2001/11/01;414(6861):359-367.

[93] Cheng X-B, Zhang R, Zhao C-Z, et al. Toward Safe Lithium Metal Anode in Rechargeable Batteries: A Review. Chemical Reviews. 2017 2017/08/09;117(15):10403-10473.

[94] Biswal P, Stalin S, Kludze A, et al. Nucleation and Early Stage Growth of Li Electrodeposits. Nano Letters. 2019 2019/11/13;19(11):8191-8200.

[95] Zuo T-T, Wu X-W, Yang C-P, et al. Graphitized Carbon Fibers as Multifunctional 3D Current Collectors for High Areal Capacity Li Anodes. Advanced Materials. 2017;29(29):1700389.

[96] Niu C, Pan H, Xu W, et al. Self-smoothing anode for achieving high-energy lithium metal batteries under realistic conditions. Nature Nanotechnology. 2019 2019/06/01;14(6):594-601.

[97] Sun Z, Jin S, Jin H, et al. Robust Expandable Carbon Nanotube Scaffold for Ultrahigh-Capacity Lithium-Metal Anodes. Advanced Materials. 2018;30(32):1800884.

[98] Liu K, Li Z, Xie W, et al. Oxygen-rich carbon nanotube networks for enhanced lithium metal anode. Energy Storage Materials. 2018 2018/11/01/;15:308-314.

[99] Li N, Zhang K, Xie K, et al. Reduced-Graphene-Oxide-Guided Directional Growth of Planar Lithium Layers. Advanced Materials. 2020;32(7):1907079.

[100] Zhang R, Chen X-R, Chen X, et al. Lithiophilic Sites in Doped Graphene Guide Uniform Lithium Nucleation for Dendrite-Free Lithium Metal Anodes. Angewandte Chemie. 2017;129(27):7872-7876.

[101] Liu L, Yin Y-X, Li J-Y, et al. Uniform Lithium Nucleation/Growth Induced by Lightweight Nitrogen-Doped Graphitic Carbon Foams for High-Performance Lithium Metal Anodes. Advanced Materials. 2018;30(10):1706216.

[102] Kim J, Lee J, Yun J, et al. Functionality of Dual-Phase Lithium Storage in a Porous Carbon Host for Lithium-Metal Anode. Advanced Functional Materials. 2020;30(15):1910538.

[103] Lee J, Choi SH, Qutaish H, et al. Structurally stabilized lithium-metal anode via surface chemistry engineering. Energy Storage Materials. 2021 2021/05/01/;37:315-324.

[104] Yan K, Lu Z, Lee H-W, et al. Selective deposition and stable encapsulation of lithium through heterogeneous seeded growth. Nature Energy. 2016 2016/02/22;1(3):16010.

[105] Yang C, Yao Y, He S, et al. Ultrafine Silver Nanoparticles for Seeded Lithium Deposition toward Stable Lithium Metal Anode. Advanced Materials. 2017;29(38):1702714.

[106] Fang Y, Zhang SL, Wu Z-P, et al. A highly stable lithium metal anode enabled by Ag nanoparticle–embedded nitrogen-doped carbon macroporous fibers. Science Advances. 2021;7(21):eabg3626.

[107] Yan J, Liu M, Deng N, et al. Flexible MnO nanoparticle-anchored N-doped porous carbon nanofiber interlayers for superior performance lithium metal anodes [10.1039/D0NA00690D]. Nanoscale Advances. 2021;3(4):1136-1147.

[108] Yang G, Li Y, Tong Y, et al. Lithium Plating and Stripping on Carbon Nanotube Sponge. Nano Letters. 2019 2019/01/09;19(1):494-499.

[109] Liu H, Chen X, Cheng X-B, et al. Uniform Lithium Nucleation Guided by Atomically Dispersed Lithiophilic CoNx Sites for Safe Lithium Metal Batteries. Small Methods. 2019;3(9):1800354.

[110] Li X, Chu Z, Jiang H, et al. Redistributing Li-ion flux and homogenizing Li-metal growth by N-doped hierarchically porous membranes for dendrite-free Lithium metal batteries. Energy Storage Materials. 2021 2021/05/01/;37:233-242.

[111] Jin C, Sheng O, Luo J, et al. 3D lithium metal embedded within lithiophilic porous matrix for stable lithium metal batteries. Nano Energy. 2017 2017/07/01/;37:177-186.

[112] Li Q, Zhu S, Lu Y. 3D porous Cu current collector/Li-metal composite anode for stable lithium-metal batteries. Adv Funct Mater 2017; 27:1606422.

[113] Jiang Z, Liu T, Yan L, et al. Metal-organic framework nanosheets-guided uniform lithium deposition for metallic lithium batteries. Energy Storage Mater 2018; 11:267-273.

[114] Eom GH, Han SA, Suh JH, Kim JH, Park M-S. Enriched Cavities to ZIF-8-Derived Porous Carbon for Reversible Metallic Lithium Storage. ACS Appl Energy Mater 2021; 4:14520-14525.

[115] Chu F, Hu J, Tian J, Zhou X, Li Z, Li C. In situ plating of porous Mg network layer to reinforce anode dendrite suppression in Li-metal batteries. ACS Appl Mater Interfaces 2018; 10:12678-12689.

[116] Wang Y, Wang Z, Lei D, et al. Spherical Li deposited inside 3D Cu skeleton as anode with ultrastable performance. ACS Appl Mater Interfaces 2018; 10:20244-20249.

[117] Foroozan T, Soto FA, Yurkiv V, et al. Synergistic effect of graphene sxide for impeding the dendritic plating of Li. Adv Funct Mater 2018; 28:1705917.

[118] Jin C, Sheng O, Luo J, et al. 3D lithium metal embedded within lithiophilic porous matrix for stable lithium metal batteries. Nano Energy 2017; 37:177-186.

[119] Zhao H, Lei D, He Y-B, et al. Compact 3D copper with uniform porous structure derived by electrochemical dealloying as dendrite-free lithium metal anode current collector. Adv Energy Mater 2018; 8:1800266.

[120] Yuan S, Bao JL, Li C, Xia Y, Truhlar DG, Wang Y. Dual lithiophilic structure for uniform Li deposition. ACS Appl Mater Interfaces 2019; 11:10616-10623.

[121] Zhu M, Li B, Li S, Du Z, Gong Y, Yang S. Dendrite-free metallic lithium in lithiophilic carbonized metal–organic frameworks. Adv Energy Mater 2018; 8:1703505.

[122] Li Y, Fan J, Zhang J, et al. A Honeycomb-like Co@N–C composite for ultrahigh sulfur loading Li–S batteries. ACS Nano 2017; 11:11417-11424.

[123] Jagadeesh RV, Murugesan K, Alshammari AS, et al. MOF-derived cobalt nanoparticles catalyze a general synthesis of amines. Seince 2017; 358:326-332.

[124] Lee KJ, Lee JH, Jeoung S, Moo HR. Transformation of metal–organic frameworks/coordination polymers into functional nanostructured materials: Experimental approaches based on mechanistic insights. Acc Chem Res 2017; 50:2684-2692.

[125] Wang L, Zhu X, Guan Y, et al. ZnO/carbon framework derived from metal-organic frameworks as a stable host for lithium metal anodes. Energy Storage Mater 2018; 11:191-196.

[126] Lee J, Choi SH, Qutaish H, et al. Structurally stabilized lithium-metal anode via surface chemistry engineering. Energy Storage Mater 2021; 37:315-324.

[127] Qutaish H, Han SA, Rehman Y, Konstantiov K, Park M-S, Kim JH. Porous carbon architectures with different dimensionalities for lithium metal storage. Sci Technol Adv Mater 2022; 23:169-188.

[128] Choi SH, Hyeon Y, Shin HR, et al. Critical role of surface craters for improving the reversibility of Li metal storage in porous carbon frameworks. Nano Energy 2021; 88:106243.

[129] Landesfeind J, Hattendorff J, Ehrl A, Wall WA, Gasteiger HA. Tortuosity determination of battery electrodes and separators by impedance spectroscopy. J Electrochem Soc 2016; 163:A1373-A1387.

[130] Chen Y, Li S, Pei X, et al. A Solvent-free hot-pressing method for preparing metal–organic-framework coatings. Angew Chem Int Ed 2016; 55:3419-3423.

[131] Gao X, Du Y, Zhou J, et al. Large-scale production of MOF-derived coatings for functional interlayers in high-performance Li–S batteries. ACS Appl Energy Mater 2018; 1:6986-6991.

[132] Liu Z-C, Xu J-J, Yuan S, et al. Artificial protection film on lithium metal anode toward long-cycle-life lithium–oxygen batteries. Adv Mater 2015; 27:5241-5247.

[133] Zhang X, Zhang Q, Wang X-G, et al. An extremely simple method for protecting lithium anodes in Li-O_2 batteries. Angew Chem Int Ed 2018; 57:12814-12818.

[134] Pang Q, Liang X, Shyamsunder A, Nazar LF. An in vivo formed solid electrolyte surface layer enables stable plating of Li metal. Joule 2017; 1:870-886.

[135] Hu J, Tian J, Li C. Nanostructured carbon nitride polymer-reinforced electrolyte to enable dendrite-suppressed lithium metal batteries. ACS Appl Mater Interfaces 2017; 9:11615-11625.

[136] Chen L, Connell JG, Nie A, et al. Lithium metal protected by atomic layer deposition metal oxide for high performance anodes. J Mater Chem A 2017; 5:12297-12309.

[137] Chu F, Hu J, Wu C, et al. Metal–organic frameworks as electrolyte additives to enable ultrastable plating/stripping of Li anode with dendrite inhibition. ACS Appl Mater Interfaces 2019; 11:3869-3879.

[138] Wang Z, Tan R, Wang H, et al. A Metal–organic-framework-based electrolyte with nanowetted interfaces for high-energy-density solid-state lithium battery. Adv Mater 2018; 30:1704436.

[139] Wu J-F, Guo X. MOF-derived nanoporous multifunctional fillers enhancing the performances of polymer electrolytes for solid-state lithium batteries. J Mater Chem A 2019; 7:2653-2659.

[140] Wang Z, Wang S, Wang A, et al. Covalently linked metal–organic framework (MOF)-polymer all-solid-state electrolyte membranes for room temperature high performance lithium batteries. J Mater Chem A 2018; 6:17227-34.

[141] Kim J, Lee J, Yun J, et al. Functionality of dual-phase lithium storage in a porous carbon host for lithium-metal anode. Adv Funct Mater 2020; 30:1910538.

[142] Yan C, Cheng X-B, Tian Y, et al. Dual-layered film protected lithium metal anode to enable dendrite-free lithium deposition. Adv Mater 2018; 30:1707629.

[143] Zhang X-Q, Cheng X-B, Chen X, Yan C, Zhang Q. Fluoroethylene carbonate additives to render uniform Li deposits in lithium metal batteries. Adv Funct Mater 2017; 27:1605989.

CHAPTER 3 . DESIGN OF COBALT CATALYSED CARBON NANOTUBES IN BIMETALLIC ZEOLITIC IMIDAZOLATE FRAMEWORKS

3.1. Introduction

Porous carbon nanoarchitectures have attracted significant attention as promising candidates for energy applications such as energy storage and harvesting [1-6]. In particular, porous carbon materials derived from metal-organic frameworks (MOFs) are highly attractive due to their favorable properties, such as pore size, surface area, and pore volume, which are easily controlled by adjusting the metal ions or organic linkers for the purpose [7-12]. Among the MOF groups, it is well known that zeolitic imidazolate frameworks (ZIFs) can be converted into ideal carbon hosts because of their outstanding structural and chemical stability. Typically, the carbon nanoarchitectures derived from ZIF-8 and ZIF-67, composed of zinc (Zn) and cobalt (Co) with 2-methylimidazole (2-MIM), are well known for their superior structural properties, providing many advantages such as large surface area and pore volume [13-15].

Still, each ZIF-derived carbon material has some limitations. ZIF-8-derived carbon exhibits an amorphous carbon structure, restricting the overall electrical conductivity, and ZIF-67-derived carbon suffers from relatively low surface area and pore volume [16]. Bimetallic ZIF, which results from combining ZIF-8 and ZIF-67, can address these issues by forming crystalline structures while maintaining high pore volume and

surface area [17-19]. Furthermore, the presence of Co can also induce carbon nanotube (CNT) growth on the surfaces of ZIF-derived carbon nanoarchitectures, which extremely improves the electrical properties [20, 21]. Even though hierarchical CNT-grown ZIF-derived carbon materials have been utilized in various applications, a comprehensive understanding of the CNT growth mechanisms in ZIF-derived carbon still remains elusive. Thus, in-depth knowledge of the growth mechanisms of CNTs in ZIF structures is highly desirable.

Herein, we have synthesized three types of bimetallic ZIFs to elucidate the CNT growth on bimetallic ZIF-derived carbon. Each bimetallic ZIF was controlled by adjusting the molar ratio of Zn to Co ions such as 1:1 (BZ1), 1:2 (BZ2), and 1:3 (BZ3). ZIF-8 and ZIF-67 were also prepared to use as references. All the as-prepared ZIFs were directly converted into porous carbon nanoarchitectures under nitrogen (N_2) atmosphere at 1000 °C. Excess metal species were etched away by 1 M hydrochloric acid (HCl) after carbonization to make additional mesopore structures. Zn is almost evaporated during the carbonization process due to its low boiling point (907 °C). Thus, we can infer residual Co nanoparticles (NPs) would play an essential role in growing CNTs during the carbonization process. The fact that the presence of Co triggers graphitization during pyrolysis is confirmed by X-ray diffraction (XRD) patterns and Raman spectra. In addition, a certain molar ratio of Zn to Co induces the CNT growth with graphitic carbon structure, which contributed to the enormous improvement of electrical conductivity.

3.2. Materials and methods

3.2.1. Preparation of ZIFs

All chemicals were purchased from Sigma Aldrich and utilized without any further treatment. The overall experimental procedures are shown in figure 3.1a. To start, 10 g of 2-MIM was dissolved in 50 ml of deionized (DI) water. Different molar ratios of Zn to Co ions were dissolved in another 50 ml of DI water using cobalt acetate tetrahydrate ($Co(CH_3CO_2)_2 \cdot 4H_2O$) and zinc acetate dihydrate ($Zn(CH_3CO_2)_2 \cdot 2H_2O$), as shown in Table S1. The metal ionic solutions were slowly added to the 2-MIM solution and stirred for 10 min at 1500 rpm. The mixtures were kept at room temperature for 24 hours to allow the bimetallic ZIF to precipitate. Then, the particles were collected from the mixtures and thoroughly washed with DI water and methanol several times by centrifugation at 7500 rpm. The particles were dried at 70 ºC under vacuum.

3.2.2. Carbonization of ZIFs

Prior to the heating process, the powders were kept under N_2 atmosphere for 20 min at room temperature inside a tube furnace. Then, the ZIF samples were directly converted to nanoporous carbon by pyrolysis under N_2 atmosphere at 1000 ºC. The samples were kept at 1000 ºC for 5 hours with a heating rate of 2 ºC min^{-1}. The obtained nanoporous carbon powders were washed several times with 1 M HCl and was dried at 70 ºC under vacuum for 12 hours. C-ZIF-8, C-BZ1, C-BZ2, C-BZ3, and C-ZIF-67 to abbreviate carbonized ZIF-8, BZ1, BZ2, BZ3, and ZIF-67, respectively.

3.2.3. Characterization

The surface morphology of the samples was analyzed by field emission scanning electron microscopy (SEM, JSM-7500FA) at 5 kV and transmission electron microscopy (TEM, JEOL ARM-200F and JEOL 2100F) at 200 kV. The crystalline

structures were studied utilizing a powder X-ray diffractometer (MMA, GBC Scientific Equipment LLC, Hampshire, IL) system equipped with Cu Kα radiation (λ = 0.15406 nm). Raman spectra were obtained using a MicroRaman spectrometer (Horiba-Jovin Yvon HR800). N_2 adsorption-desorption isotherms were measured by a Micrometrics TriStar II 3020 at 77 K. The surface area and pore volume were calculated by the Brunauer-Emmett-Teller (BET) method, the t-plot method, and the non-localized density functional theory (NLDFT) method. The electrical properties were measured by a powder resistivity measurement system (MCP-PD51).

3.2.4. DFT Calculations of the carbon adsorption on Co and Co_2C surfaces

Spin-polarized density functional theory (DFT) calculations were performed using the Vienna Ab-initio Simulation Package implementing first-principles calculations. The projector augmented wave approach with an energy cut-off of 500 eV and the exchange-correlation form of the Perdew-Burke-Ernzerhof generalized gradient approximation (GGA) were used in all calculations. Monkhorst-Pack k-point sets of 7 × 7 × 7 for the bulk and 7 × 7 × 1 for the surface were used. Various surfaces having 4 or 5 layers with 10 Å vacuum space were generated, and then the atomic positions were only fully relaxed with fixed cell parameters. Surface energies (γ) were calculated from the following expression:

$$\gamma = \frac{E_{slab} - N \cdot E_{bulk}}{2A} \quad (1)$$

Where $E_{slab}$the total energy of the surface slab is obtained using density functional theory. N is the number of atoms in the surface slab, and E_{bulk} is the bulk energy per atom. A is the surface area exposed to the vacuum spacing.

To determine the thermodynamically favourable C doping sites, the adsorption energy for each atomic configuration was computed as follows:

$$E_{adsorb} = E\left(C - Co_{surf}\ or\ Co_2C_{surf}\right) - \left\{E\left(Co_{surf}\ or\ Co_2C_{surf}\right) + E(C)\right\} \quad (2)$$

Where $E\left(C - Co_{surf}\ or\ Co_2C_{surf}\right)$ is the total free energy of a C atom on the Co or Co_2C surface obtained from first-principles calculations. $E\left(Co_{surf}\ or\ Co_2C_{surf}\right)$ and $E(C)$ are the total free energy values of a low index Co or Co_2C surface and a carbon single atom, respectively. Herein, we considered three different low surface indices: (100), (110), and (111).

3.3. Results and discussion

3.3.1. The role of Co nanocatalyst

The XRD patterns and Raman spectra elucidate the crystallinity difference between C-ZIF-8 and C-ZIF-67, indicating that Co-containing C-ZIF-67 consist of graphitic carbon while C-ZIF-8 is made up of amorphous carbon (figure 3.2). Thus, we focused on the effect of Co NPs on the graphitization. Spin-polarized DFT calculations were performed using the Vienna Ab-initio Simulation Package implementing first-principles calculations. Co (face-centered cubic, FCC) metal was modelled as a catalyst to induce graphitization, and cobalt carbide (Co_2C, Pnnm) was also considered because Co metal tends to dissolve the carbon (C) under high temperature [22-25]. This tendency can be confirmed by the XRD pattern of ZIF-67-derived carbon, which shows peaks for the Co_2C(111) (JCPDS file no. 96-152-8416) as well as the Co(111) (JCPDS file no. 96-901-2950) planes (figure 3.3).

The surface energies and C adsorption energies of some crystal facets in Co and Co_2C were investigated to provide clues as to which crystal facet is preferred and which crystal plane plays a critical role in the graphitization process. Figure 3.1b shows selected (100), (110), and (111) planes of both Co and Co_2C, and the DFT calculation

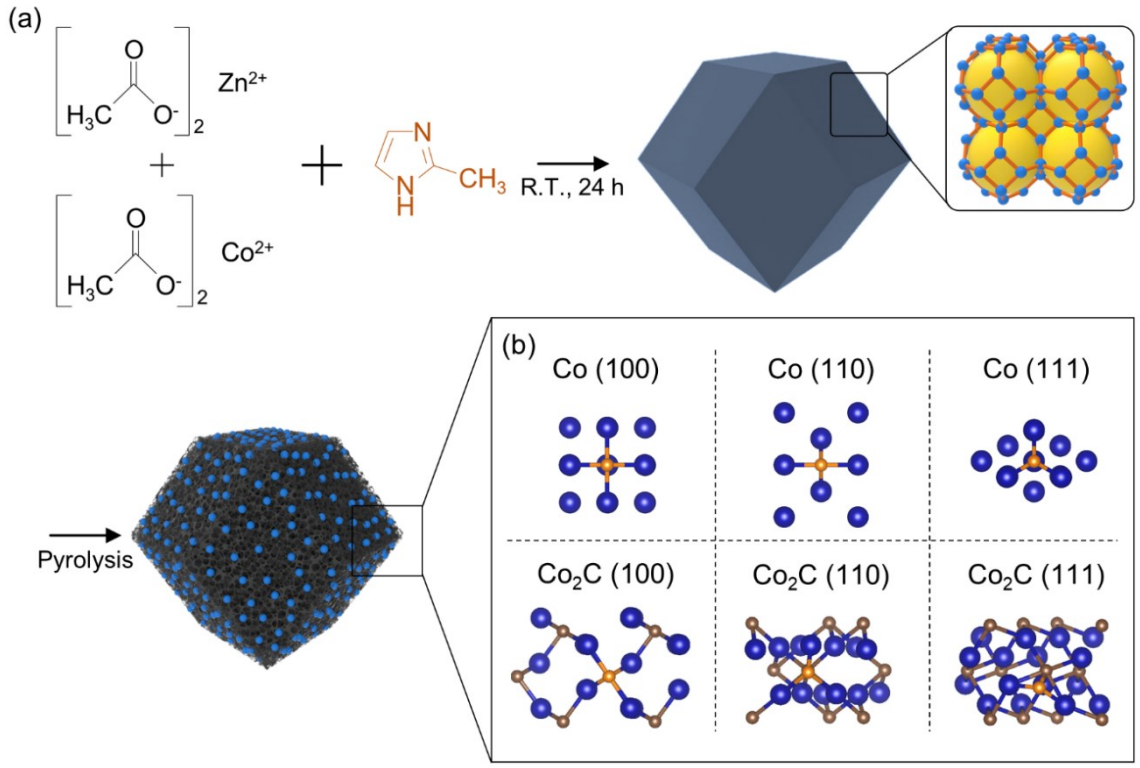

Figure 3.1. The schematic illustration of overall experimental procedures. (b) atomic arrangements for C atom adsorption on Co (100), Co (110), Co (111), Co_2C (100), Co_2C (110), and Co_2C (111), as determined by the DFT calculations.

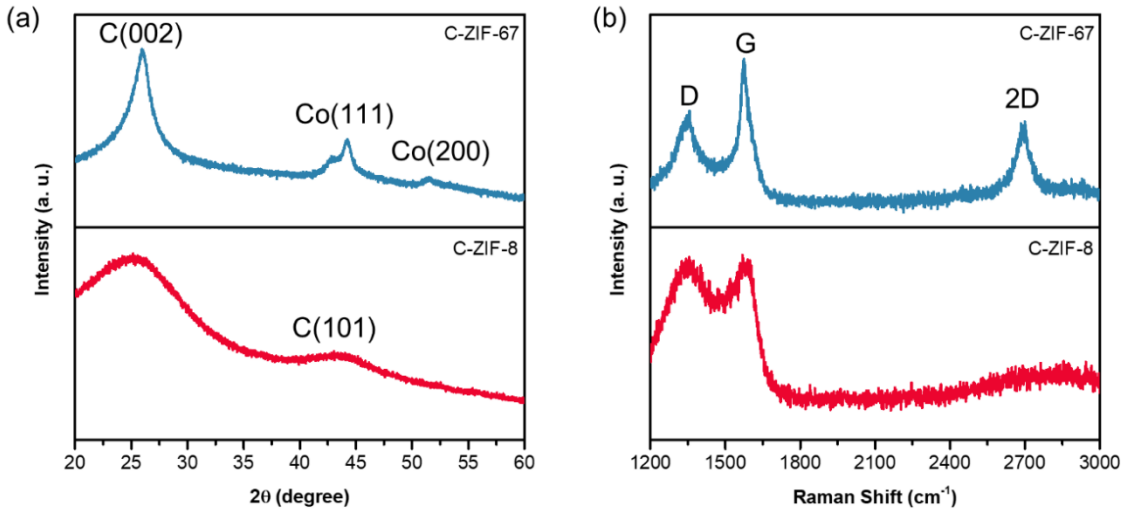

Figure 3.2. (a) XRD patterns of C-ZIF-8 and C-ZIF-67. (b) Raman spectra of C-ZIF-8 and C-ZIF-67.

results are summarized in Table 1. The (111) planes of Co and Co_2C would be predominantly observed in the carbon materials derived from ZIF structures containing

Co, since these crystal planes have the lowest surface energy, which agrees with peak index values confirmed by XRD.

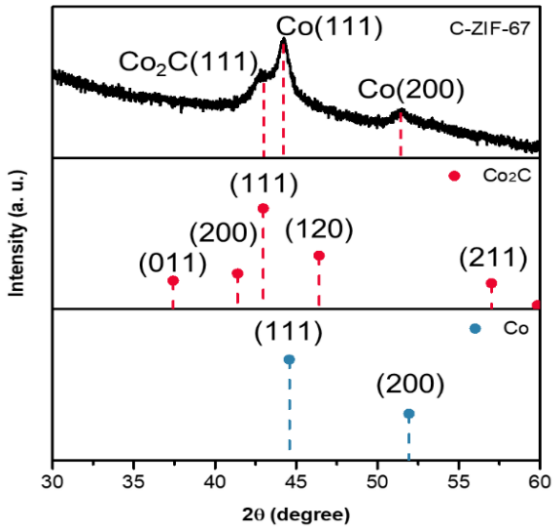

Figure 3.3. XRD pattern of C-ZIF-67, showing that it is composed of Co and Co_2C.

In the case of C adsorption, however, the (111) crystal planes are the least preferred due to the unsaturated C atom, which has three coordination numbers. C atoms are much more easily adsorbed on the (100) planes of Co and Co_2C than on the (110) or (111) planes and have four-fold coordination lowering the adsorption energy. Furthermore, Co metal is expected to play an essential role in C adsorption, the first step of graphitization, because Co planes show relatively low C adsorption energies compared to Co_2C planes. Briefly, the Co ions in the ZIF structure are reduced to Co metal during the pyrolysis [26], and some of the Co metal can be transformed into Co_2C by absorbing the dissociated carbon atoms. These Co species aggregate to reduce crystal planes are predominantly exposed. Also, the agglomerated Co and Co_2C NPs act as efficient catalysts to form graphitic carbon because dissociated carbon atoms are easily adsorbed on certain crystal facets.

Table 3.1. Calculated surface energy of Co and Co2C planes with low surface index values and adsorption energy of a C atom from the DFT calculations.

Crystal plane		Surface energy (eV $Å^{-2}$)	Adsorption energy of C atom (eV $Å^{-2}$)
Co	(100)	0.1680	-9.4041
	(110)	0.1700	-8.7136
	(111)	0.1357	-8.3091
Co_2C	(100)	0.1741	-8.1435
	(110)	0.1821	-7.5861
	(111)	0.1738	-5.8163

This process allows the formation of the basic units for graphitization, and all bimetallic ZIFs turn into graphitic carbon through the above process. Thus, all bimetallic ZIF-derived carbons tend to consist of graphitic carbon structures, as confirmed by XRD and Raman spectroscopy (figure 3.4).

3.3.2. The size effect of Co nanocatalyst

Even though all bimetallic ZIF-derived carbon materials show graphitic structures, only C-BZ1 contains a large amount of CNTs on its surface, whereas C-BZ3 have few CNTs (figure 3.5a). The Co NPs and their surroundings were thoroughly investigated through transmission electron microscopy (TEM) analysis to elucidate the CNT growth mechanism. As shown in figure 3.5b, the size of Co metal particles in the C-BZ1 is estimated to be about 13 nm, and the (111) facets are mainly exposed. The fast Fourier transform (FFT) pattern of Co metal in figure 3.5c also confirms that the (111) crystal plane, which has the lowest surface energy, is dominant because the small NPs tend to significantly reduce the surface energy. Thus, the Co NPs in the C-BZ1 would be less active towards adsorbing carbon atoms because of the exposed stable crystal facets. figure 3.5d suggests, however, that the Co metal particles in C-BZ3 are

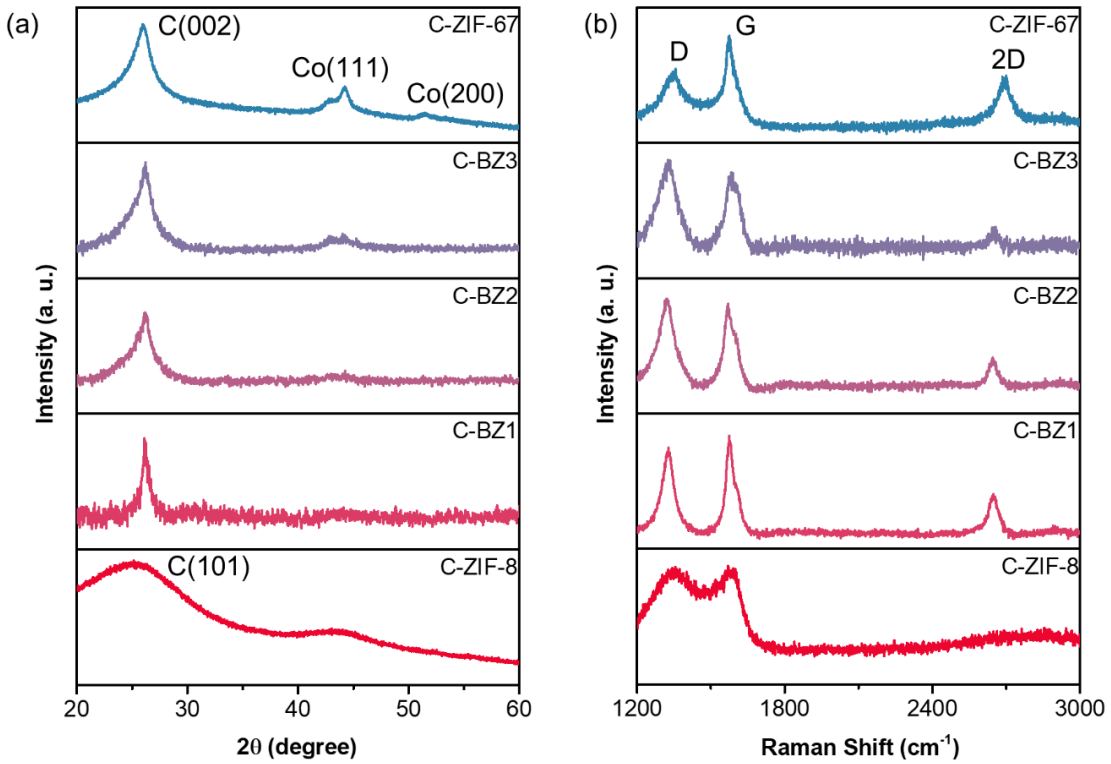

Figure 3.4. (a) XRD patterns of all as-prepared carbonized ZIFs. (b) Raman spectra of all as-prepared carbonized ZIFs.

much larger than the Co metal particles in C-BZ1. Furthermore, this Co metal exhibits the (001) and (220) crystal facets, which are relatively less stable but more catalytically active. According to the FFT pattern of this Co metal, it consists of (111) planes besides the (001) and (220) facets (figure 3.5e).

This suggests that the active facets of Co NPs in the C-BZ3 can facilitate the adsorption of the dissociated carbon atoms, and these Co NPs easily and faster form the graphitic carbon around the Co NPs. Thus, we can infer that this phenomenon mainly results from the size of the Co NPs, and this size difference is mainly caused by the ratio of Zn to Co ions in the bimetallic ZIFs. Additionally, the size of catalysts would affect the diffusion mode of dissociated carbon atoms during the carbonization process. The carbon sources in the case of the large Co particles arrive at the catalytic active sites by bulk diffusion, while surface diffusion is dominant at the small Co NPs [25]. This difference of diffusion mode also contributes the difference of growth. Unfortunately,

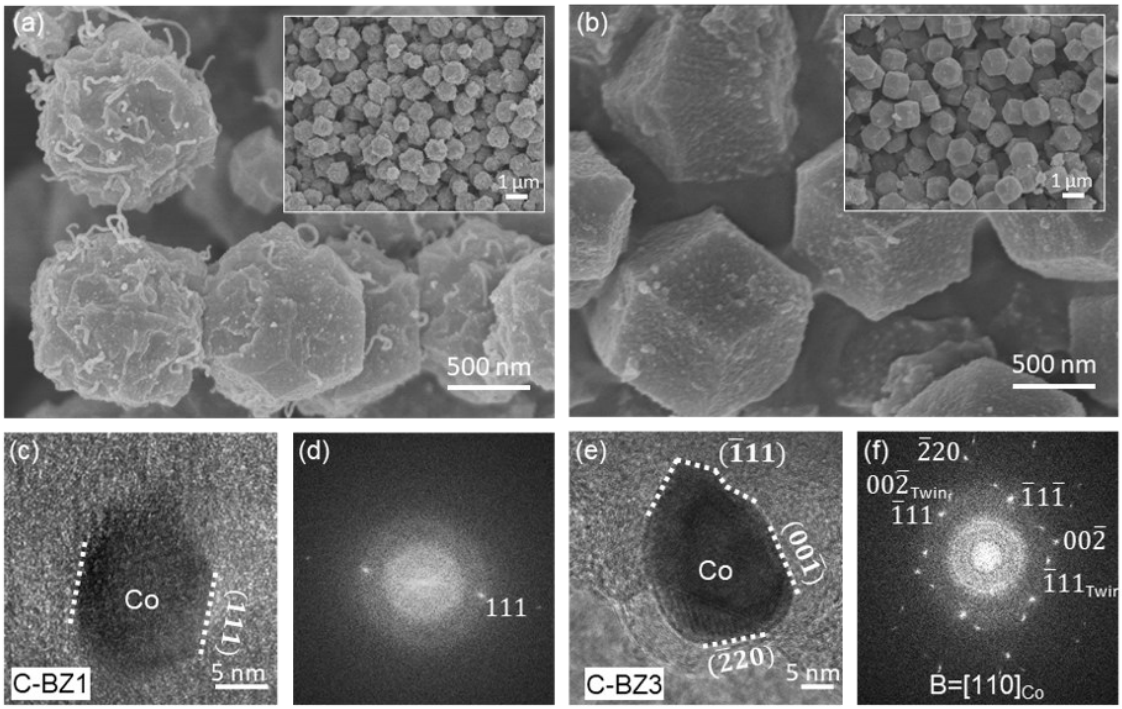

Figure 3.5. (a) The low-magnification and high-magnification (inset) SEM images of C-BZ1 and C-BZ3 particles. High-resolution TEM (HRTEM) image of Co NP in (b) C-BZ1 and (d) C-BZ3. The corresponding FFT pattern in (c) C-BZ1 and (e) C-BZ3. Scales bars in (a) and (b) 500 nm. (Inset: 1 μm). Scale bars in (b) and (d) 5 nm

Co_2C, which was also considered at DFT calculation, is not easily investigated by our TEM analysis because Co has low C solubility at room temperature [27].

Figure 3.6a shows the high-angle annular dark field (HAADF) image of a CNT and a Co NP in C-BZ1. The Co NP is brighter than the surrounding C structure due to its high atomic number. The CNT that has grown is a multiwalled CNT about 10 nm in diameter (figure 3.6b). The C-BZ3 has a Co NP about 2 times larger compared to one in C-BZ1 (figure 3.6c). As shown in figure 3.6d, the Co NP is covered by multilayers of graphitic shell. Thus, the size of the Co NPs, mainly caused by the difference in the amount of Co, is a critical factor that alters the activities of Co catalysts, as illustrated in figure 3.6e. BZ-1 has a small amount of Co compared to BZ-3, and small Co NPs form during pyrolysis. These small Co NPs induce CNT growth based on the catalytic active sites of the Co NPs. In BZ-3, however, a larger amount of Co atoms exists in the structure

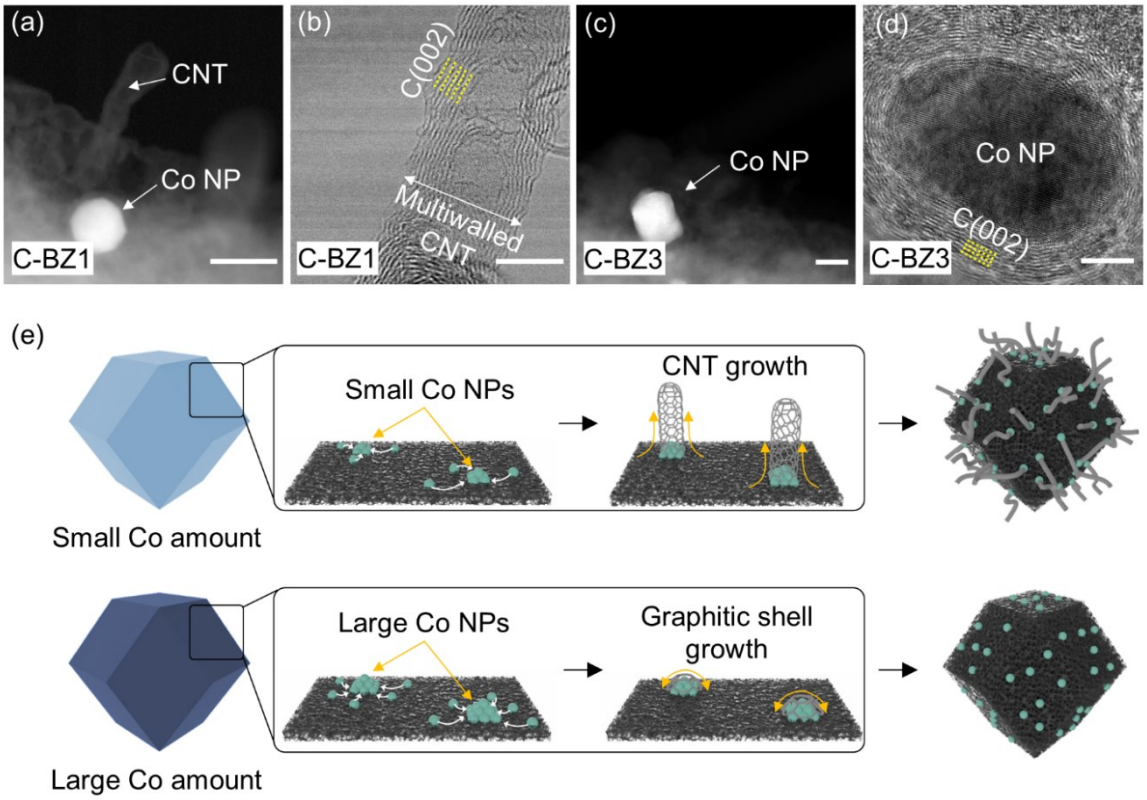

Figure 3.6. (a) XRD patterns of all as-prepared carbonized ZIFs. (b) Raman spectra of all as-prepared carbonized ZIFs. High-angle annular dark field – scanning TEM (HAADF-STEM) images of (a) C-BZ1 and (c) C-BZ3. HRTEM images of (b) a CNT in C-BZ1 and (d) graphitic shells in C-BZ3. (e) Schematic illustration of the dependence of the CNT growth mechanism on the size of Co catalyst NPs. Scale bars in (a) and (c): 20 nm. Scale bars in (b) and (d): 5 nm.

and results in larger Co NPs. These relatively large Co particles do not catalyze the CNTs growth but catalyze the graphitic shell growth.

3.3.3. The physical properties

The critical effect of CNTs grown on porous carbon materials is particularly prominent for their electrical properties. The Co NPs trigger the graphitization, and thus, more graphitic structures appear according to the increase in the amount of Co. This results in a huge improvement in the electrical conductivity, which shows an increasing tendency from ZIF-8 to ZIF-67, as shown in figure 3.7a.

The carbon material derived from ZIF-8 is made up of amorphous carbon, and thus, it exhibits the lowest electrical conductivity among all the carbonized ZIFs. On the contrary, the ZIF-67-derived carbon shows around 6 times higher electrical conductivity than ZIF-8-derived carbon. In the case of C-BZ1, however, it provides exceptionally high electrical conductivity, which is about 80 times higher than the electrical conductivity of carbonized ZIF-8 and even 12 times higher than the electrical conductivity of carbonized ZIF-67. Even though C-BZ1 contains the smallest amount

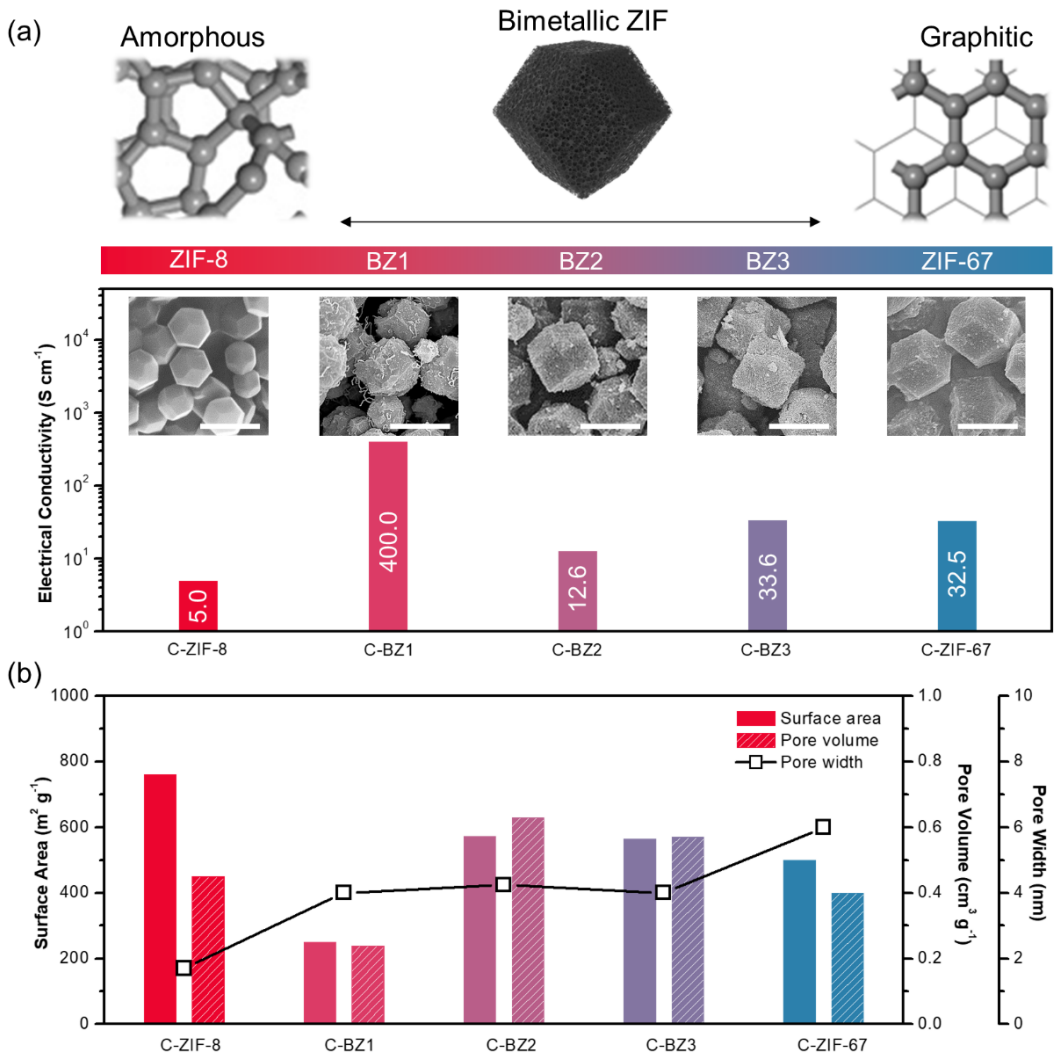

Figure 3.7. (a) The powder conductivity of all carbonized ZIFs at 47.75 MPa. (b) Porous characteristics of all carbonized ZIF materials. Scale bars in SEM images in (a): 1 μm. The overall pressure dependences of electrical conductivities are summarized in Figure 3.8.

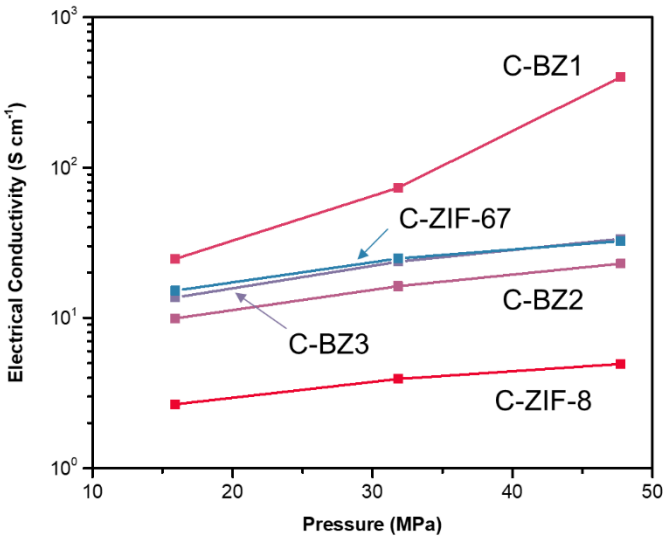

Figure 3.8. Pressure dependence of the electrical conductivity of all as-prepared carbonized ZIFs.

of Co among the bimetallic ZIFs, it contains many CNTs on its surface. This large amount of CNTs enhances the electrical junctions between particles, which reduces the electrical resistance between particles. The particle size effect on the electrical conductivity can be also considered, but it is almost negligible. This is because all the carbonized ZIFs show similar particle sizes (figure 3.9).

Therefore, graphitization triggered by Co species improves the electrical conductivity. Meanwhile, CNTs grown on the surfaces under appropriate conditions give rise to a dramatic increase in desirable electrical properties. Lastly, all bimetallic ZIF-derived carbon nanoarchitectures show outstanding porous structures with high pore volumes and large surface areas (figure. 3.7b). The pore size tends to be increased according to contain more Co. Specifically, ZIF-8-derived carbon shows microporous structures, whereas mesoporous structures are observed in porous carbon materials derived from Co-containing ZIFs. In case of C-BZ1, the pore volume and surface area are slightly reduced, but the structure still shows splendid porous structure.

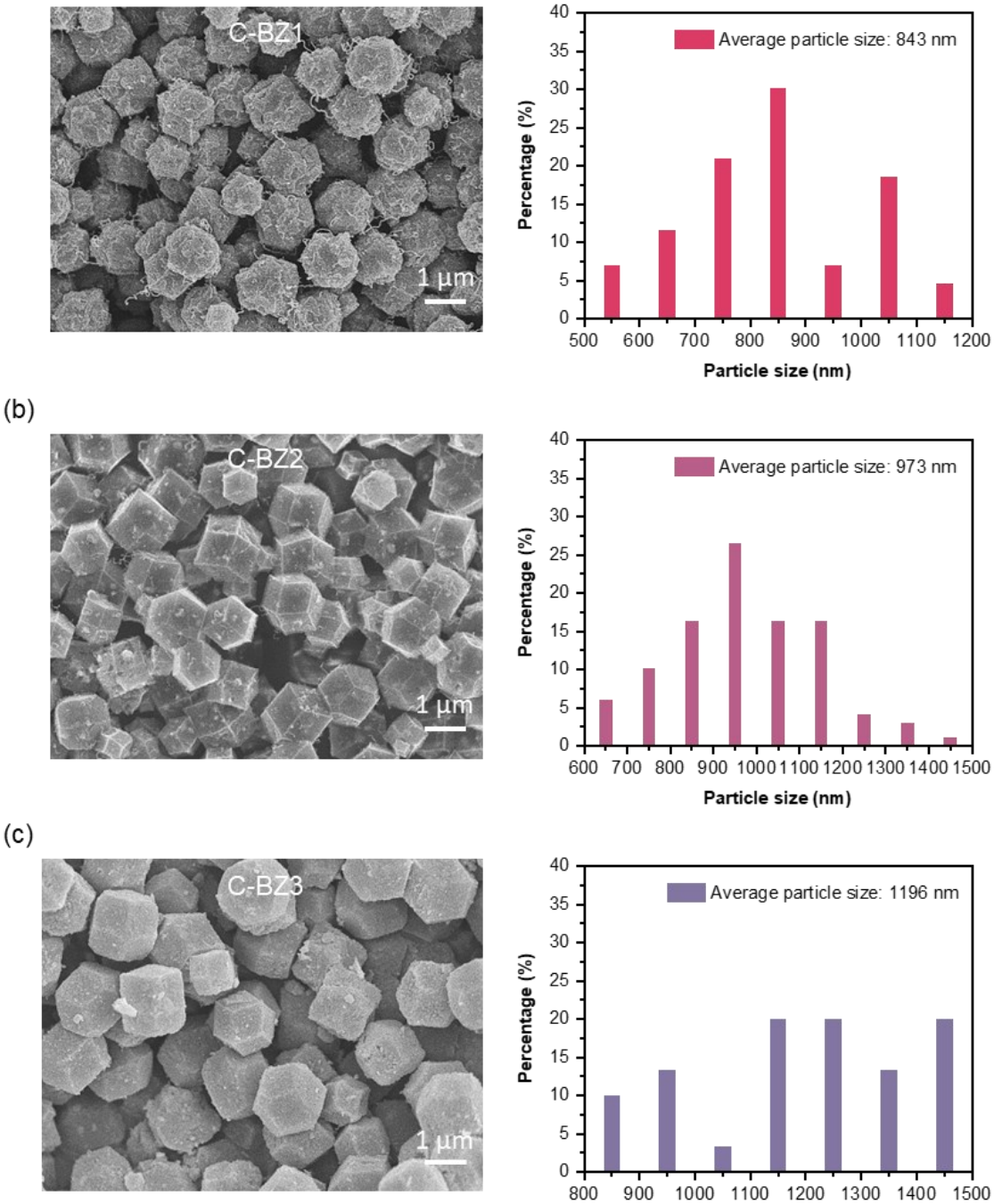

Figure 3.9. Particle size distributions of C-BZ1, C-BZ2, and C-BZ3. Scale bars: 1 µm.

3.4. Conclusion

Bimetallic ZIF-derived carbon materials were strategically prepared to understand the factors affecting CNT growth. In this system, the role of Co NPs as catalysts was proved to induce graphitization during pyrolysis, and the sizes of the Co

particles provided insight into the CNT growth mechanism. The CNT-grown bimetallic ZIF-derived carbon materials exhibited exceptionally high electrical conductivity, and this kind of highly conductive porous carbon material can be expected to be applied in a variety of electrochemical storage applications.

3.5. References

[1] Y. Hyeon, J. Lee, H. Qutaish, S.A. Han, S.H. Choi, S.W. Moon, M.-S. Park, D. Whang, J.H. Kim, Lithium metal storage in zeolitic imidazolate framework derived nanoarchitectures, Energy Storage Mater. 33 (2020) 95-107.

[2] J. Kim, J. Lee, J. Yun, S.H. Choi, S.A. Han, J. Moon, J.H. Kim, J.-W. Lee and M.-S. Park, Functionality of dual-phase lithium storage in a porous carbon host for lithium-metal anode, Adv. Funct. Mater. 30 (2020) 1910538.

[3] K. Jayaramulu, D.P. Dubal, B. Nagar, V. Ranc, O. Tomanec, M. Petr, K.K.R. Datta, R. Zboril, P. Gomez-Romero and R.A. Fischer, Ultrathin hierarchical porous carbon nanosheets for high-performance supercapacitors and redox electrolyte energy storage, Adv. Mater. 30 (2018) 1705789.

[4] J. Kim, C. Young, J. Lee, Y.-U. Heo, M.-S. Park, M.S.A. Hossain, Y. Yamauchi and J.H. Kim, Nanoarchitecture of MOF-derived nanoporous functional composites for hybrid supercapacitors, J. Mater. Chem. A 5 (2017) 15065-15072.

[5] J. Lee, J. Kim and T. Hyeon, Recent progress in the synthesis of porous carbon materials, Adv. Mater. 18 (2006) 2073-2094.

[6] Y. Yang, K. Chiang and N. Burke, Porous carbon-supported catalysts for energy and environmental applications: A short review, Catal. Today 178 (2011) 197-205.

[7] H.-C. Zhou and S. Kitagawa, Metal–organic frameworks (MOFs), Chem. Soc. Rev. 43 (2014) 5415-5418.

[8] A. Schoedel, Z. Ji and O.M. Yaghi, The role of metal–organic frameworks in a carbon-neutral energy cycle, Nat. Energy 1 (2016) 16034.

[9] B. Li, H.-M. Wen, Y. Cui, W. Zhou, G. Qian and B. Chen, Emerging multifunctional metal–organic framework materials, Adv. Mater. 28 (2016) 8819-8860.

[10] R.R. Salunkhe, Y.V. Kaneti, J. Kim, J.H. Kim and Y. Yamauchi, Nanoarchitectures for metal–organic framework-derived nanoporous carbons toward supercapacitor applications, Acc. Chem. Res. 49 (2016) 2796-2806.

[11] T. Fujigaya, Development of thermoelectric conversion materials using carbon nanotube sheets, Bull. Chem. Soc. Jpn. 2 (2019) 400-408.

[12] D.G. Papageorgiou, Z. Li, M. Liu, I.A. Kinloch and R.J. Young, Mechanisms of mechanical reinforcement by graphene and carbon nanotubes in polymer nanocomposites, Nanoscale 12 (2020) 2228-2267.

[13] K.S. Park, Z. Ni, A.P. Cote, J.Y. Choi, R. Huang, F.J. Uribe-Romo, H.K. Chae, M. O'keeffe and O.M. Yaghi, Exceptional chemical and thermal stability of zeolitic imidazolate frameworks, Proc. Natl. Acad. Sci. U.S.A. 103 (2006) 10186-10191.

[14] B. Chen, Z. Yang, Y. Zhu and Y. Xia, Zeolitic imidazolate framework materials: recent progress in synthesis and applications, J. Mater. Chem. A 2 (2014) 16811-16831.

[15] W. Chaikittisilp, M. Hu, H. Wang, H.-S. Huang, T. Fujita, K.C.-W. Wu, L.-C. Chen, Y. Yamauchi and K. Ariga, Nanoporous carbons through direct carbonization of a zeolitic imidazolate framework for supercapacitor electrodes, Chem. Commun. 48 (2012) 7259-7261.

[16] K. Zhou, B. Mousavi, Z. Luo, S. Phatanasri, S. Chaemchuen and F. Verpoort, Characterization and properties of Zn/Co zeolitic imidazolate frameworks vs. ZIF-8 and ZIF-67, J. Mater. Chem. A 5 (2017) 952-957.

[17] J. Tang, R.R. Salunkhe, H. Zhang, V. Malgras, T. Ahamad, S.M. Alshehri, N. Kobayashi, S. Tominaka, Y. Ide, J.H. Kim and Y. Yamauchi, Bimetallic metal-organic frameworks for controlled catalytic graphitization of nanoporous carbons, Sci. Rep. 6 (2016) 30295.

[18] S.A. Han, J. Lee, K. Shim, M. Shahabuddin, J.-W. Lee, S.-W. Kim, M.-S. Park and J.H. Kim, Strategically designed zeolitic imidazolate frameworks for controlling the degree of graphitization, Bull. Chem. Soc. Jpn. 91 (2018) 1474-1480.

[19] J. Kim, C. Young, J. Lee, M.-S. Park, M. Shahabuddin, Y. Yamauchi and J.H. Kim, CNTs grown on nanoporous carbon from zeolitic imidazolate frameworks for supercapacitors, Chem. Commun. 52 (2016) 13016-13019.

[20] A. Azhar, Y. Li, Z. Cai, M.B. Zakaria, M.K. Masud, M.S.A. Hossain, J. Kim, W. Zhang, J. Na, Y. Yamauchi and M. Hu, Nanoarchitectonics: a new materials horizon for Prussian blue and its analogues 4 (2019) 875-904.

[21] Q. Wang and D. Astruc, State of the art and prospects in metal-organic framework (MOF)-based and MOF-derived nanocatalysis, 120 (2020) 1438-1511.

[22] H. Ago, Y. Ito, N. Mizuta, K. Yoshida, B. Hu, C.M. Orofeo, M. Tsuji, K.-I. Ikeda and S. Mizuno, Epitaxial chemical vapor deposition growth of single-layer graphene over cobalt film crystallized on sapphire, ACS Nano 4 (2010) 7407-7414.

[23] G. Amato, High temperature growth of graphene from cobalt volume: effect on structural properties, Materials 11 (2018) 257.

[24] E. Kim, H. An, H. Jang, W.-J. Cho, N. Lee, W.-G. Lee, J. Jang, Growth of few-layer graphene on a thin cobalt film on a Si/SiO_2 substrate, Chem. Vap. Deposition 17 (2011) 9-14.

[25] Y. Hu, L. Zhu, Y. Peng, J. Fu, X. Deng, J. Zhang, H. Zhang, C. Guan, A. Karim and X. Zhang, Atomic self-reconstruction of catalyst dominated growth mechanism of graphite structures, ChemCatChem 12 (2020) 1316-1324.

[26] J. Meng, C. Niu, L. Xu, J. Li, X. Liu, X. Wang, Y. Wu, X. Xu, W. Chen, Q. Li, Z. Zhu, D. Zhao, L. Mai, General oriented formation of carbon nanotubes from metal–organic frameworks, J. Am. Chem. Soc. 139 (2017) 8212-8221.

[27] K. Ishida and T. Nishizawa, The C-Co (carbon-cobalt) system, J. Phase Equil. 12 (1991) 417-424.

CHAPTER 4 . GROWTH MECHANISM OF LITHIUM CLUSTERS ON THE SURFACE OF POROUS CARBON FRAMEWORK FOR LITHIUM METAL BATTERIES

4.1. Introduction

Daily developments on portable devices and electric vehicles have increased in parallel with the demand for high energy density demand to expand their electrochemical energy storage capabilities.[1-4] Utilizing a Lithium (Li) metal as an anodic material has recently garnered much attention due to their remarkable theoretical capacity (3860 mAh g^{-1}), low negative electrochemical potential (-3.04 V vs. standard hydrogen electrode), and low density (0.53 g cm^{-3}).[4, 5] The utilization of metallic Li anodes remains challenging, however, and has many limitations that can undermine battery performance and safety.[5-7] This is due to the high reactivity and enormous volume changes of Li, which result in a non-uniform and continuous formation of the solid electrolyte interphase (SEI), inevitable Li dendritic growth, and dead Li. [8-12]

To suppress Li dendritic growth and guide uniform Li deposition, many studies have suggested employing three-dimensional (3D) constructed porous carbon hosts. [5, 13-16] This strategy has shown reduced local current density as well as enormous volume change accommodation. [4, 17] Nevertheless, the fact that carbon materials suffer from poor lithiophilicity leads to significant nucleation barriers and upper surface electrodeposition of Li metal. Hence, a more detailed understanding of the

electrodeposition mechanism on the surface of the carbon material is required to provide insights into the factors responsible for enhancing lithiophilicity and Li growth during plating and stripping. [18-23]

Zeolitic imidazolate framework-derived carbons (denoted as ZIF-C) have received considerable attention as Li host materials owing to their ease of functionalization with different heteroatoms to facilitate reversible Li-metal storage during cycling. [2, 6, 24, 25] Our previous studies showed that incorporating metal ions (Co and Zn) can promote the storage capability of ZIF-C. The result when both Co and Zn were incorporated was a material denoted as bimetallic ZIF-C (BZIF-C). More specifically, the electrical conductivity of BZIF-C can aid continuous electron transport and limit electrode polarization. In addition, the large surface area and the pore network of BZIF-C can mitigate the local current density of the electrode and maintain its electrochemical stability. [17, 26-28]

The complexity of the nucleation and growth mechanisms during Li electrodeposition mainly arises from the chemical composition of the BZIF-C. [29-31] As mentioned earlier, the BZIF-C framework consists of controllable heteroatoms and metals that act as seeds to allow selective nucleation and uniform Li metal deposition. [32-34] In other words, the primary nucleation of the Li seeds on BZIF-C can be associated with the adsorption energy of the nearby Li ions. To the best of our knowledge, the relationship between its initial heterogeneous nucleation and the growth of the Li metal is still insufficiently understood. [35-38]

In this chapter, we study the growth mechanism of Li clusters during Li plating and stripping. By considering nitrogen heteroatoms and cobalt in the carbon framework, the density functional theory (DFT) and experimental results are systematically compared.

We further verify the local electronic structure and adsorption of Li ions from the viewpoints of Li deposition for next-generation Li metal batteries.

4.2 Experimental section

4.2.1 DFT calculations

Density functional theory (DFT) calculations was performed to simulate the Li adatom processes by implementing the Vienna Ab Initio Simulation Package (VASP) using projector augmented wave (PAW) pseudopotentials.[39] To calculate the formation energy and charge density difference, defective graphite with Li was created via the Perdew Burke Ernzerhof (PBE) approach as a function of the generalized gradient approximation (GGA).[40] The adsorption energy of Li was computed in all possible regions at which Li was estimated to be adsorbed and according to the formerly adsorbed Li atoms. The k-point mesh was set at 3 × 3 × 1 to sample the Brillouin zone in the Monkhorst Pack scheme, with an energy cut-off of 700 eV established for the plane wave reference point in the standard computational parameters. Optimizing the full geometry was based on achieving full atomic relaxation until the forces for every atom were below 0.01 eV $Å^{-1}$. The doping effect itself was identified in a sufficiently large structure that was individually investigated for each defect type using a single area. The pyridinic and pyrrolic unit cells had 254 carbon atoms and 1 nitrogen atom, while the Co-N4 had 250 carbon atoms, 4 nitrogen atoms, and 1 cobalt atom. The algorithm of Henkelman et al.[41] was used to estimate the net charge of dopant elements in each structure, which was defined as the most stable structure when Li was adsorbed.

4.2.2 Material preparation

The synthesis of the BZIF-C material primarily involved two solutions. The first solution was made of 2.43 M 2-methyl imidazole in 50 ml deionized water (DI). The second solution was made of 0.23 M cobalt acetate and 0.12 M zinc acetate dissolved in 50 ml DI water. The two solutions were mixed continuously with a magnetic stirrer for about 15 min and then stored at room temperature for 24 hours. The resulting precipitate was collected and washed thoroughly with DI water. After that, the powder was thermally dehydrated in a drying oven overnight at 60 °C. Carbonization of the BZIF powder was conducted in Ar atmosphere at 1000 °C with a heating rate of 2 °C per minute for four hours. The resultant BZIF-C was then collected and thoroughly washed three times with 1 M HCl. Finally, the BZIF-C was activated at 100°C for 12 hours in a vacuum oven.

4.2.3 Structural characterization

A transmission electron microscope (TEM) with energy dispersive X-ray spectroscopy (EDS) and s field-emission scanning electron microscope (FE-SEM) were utilized to examine the elemental mapping and morphology of BZIF-C. X-ray photoelectron spectroscopy (XPS) and X-ray diffraction (XRD) with monochromatic Cu Kα radiation ($\lambda = 1.54056$ A) were both used to investigate the chemical composition and the crystal structure of the BZIF-C, respectively. A porosity analyzer was used to determine the total surface areas of the materials. The electrical properties of the materials were determined using a powder measurement system.

4.2.4 Electrochemical measurements

To fabricate the anode, the previously prepared BZIF-C powder (80 wt%), a conducting agent (Super P, 10 wt%), and a binder (poly-vinylidene fluoride, PVdF, 10 wt%) were mixed to create a slurry in an N-methyl-2-pyrrolidone (NMP) solution.

The slurry was deposited on a thin Cu current collector and left in a vacuum oven overnight at 120 °C to evaporate the solvent. Then, it was pressed at 200 kg cm^{-2}. The half-cells were constructed by employing Li metal (200 μm) as the counter electrode inside a CR2032 coin-type cell. Around (100μl) of electrolyte consisted of 1 M lithium bis(trifluoromethanesulfonyl)imide (LiTFSI) in dioxolane-dimethyl ether (DOL-DME; 50:50 v/v), with 1 wt% $LiNO_3$ as an additive was added. Furthermore, full cells were assembled with a commercial $LiFePO_4$ (LFP) cathode and then cycled at different current density values in the voltage range of 2.5–4.0 V.

4.3 Results and discussion

4.3.1 BZIF-C framework

The structural morphology of BZIF-C (Co/Zn-N-graphitic carbon) was confirmed by SEM images, as shown in Figure 4.1(a) and (b) in the Supporting Information. A rhombic dodecahedral morphology was observed with an average particle size of 700 nm. Detailed high resolution (HR)-TEM and EDS mapping also confirmed the degree of crystallinity and the chemical components (Figure 4.1(c)). The main elements of BZIF-C consisted of C, N, Co, and O. Note that the Zn had evaporated during the carbonation process due to its low evaporation temperature of 850ºC.

In addition, the XRD pattern and Raman spectrum verified the presence of graphitic carbon (Figure 4.2(a-b)). Given that the electrical conductivity of BZIF-C is essential to limit electrode polarization and ensure continuous electron transport, it was measured at different applied pressures (Figure 4.2(c)). The electrical conductivity linearly increased as a function of pressure, from 10 S cm^{-1} at 15 MPa to 32 S cm^{-1} at 65 MPa.

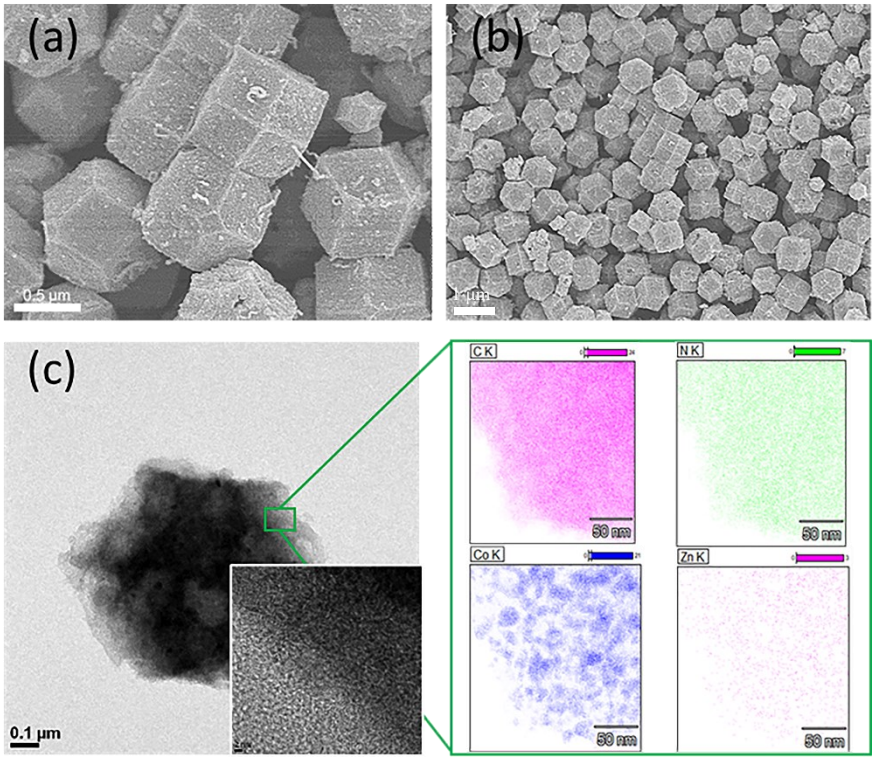

Figure 4.1. (a) and (b) Scanning electron microscope (SEM) images showing the morphology of BZIF-C. (c) Transmission electron microscope (TEM) and high-resolution (HR)-TEM images of BZIF-C with corresponding energy dispersive X-ray spectroscopy (EDX) elemental mapping images in the green box. Scale bars of EDX are 50 nm.

throughout the pore channels. For this purpose, Brunauer Emmett Teller (BET) measurements were carried out. The specific surface area, average pore volume, and pore width were estimated to be 565.2 m^2 g^{-1}, 0.5 cm^3 g^{-1}, and 5 nm, respectively, as shown in Figure 4.2(d) and (e). The BZIF-C mainly featured mesoporous structure.

The Li affinity of the BZIF-C is controlled by its surface chemistry. To elucidate the surface analysis of BZIF-C, XPS was conducted, as shown in Figure 4.3(a-c). The XPS spectrum exhibits Co peaks at 793.9 eV and 778.9 eV, indicating the presence of metallic Co nanoparticles (Co NPs). On the other hand, the Co^{2+} and Co^{3+} peaks represent the oxidation of the Co NP surfaces. The C 1s spectrum shows two peaks, with the C-N peak appears at 285.5 eV, indicating N doping in defects in the BZIF-C

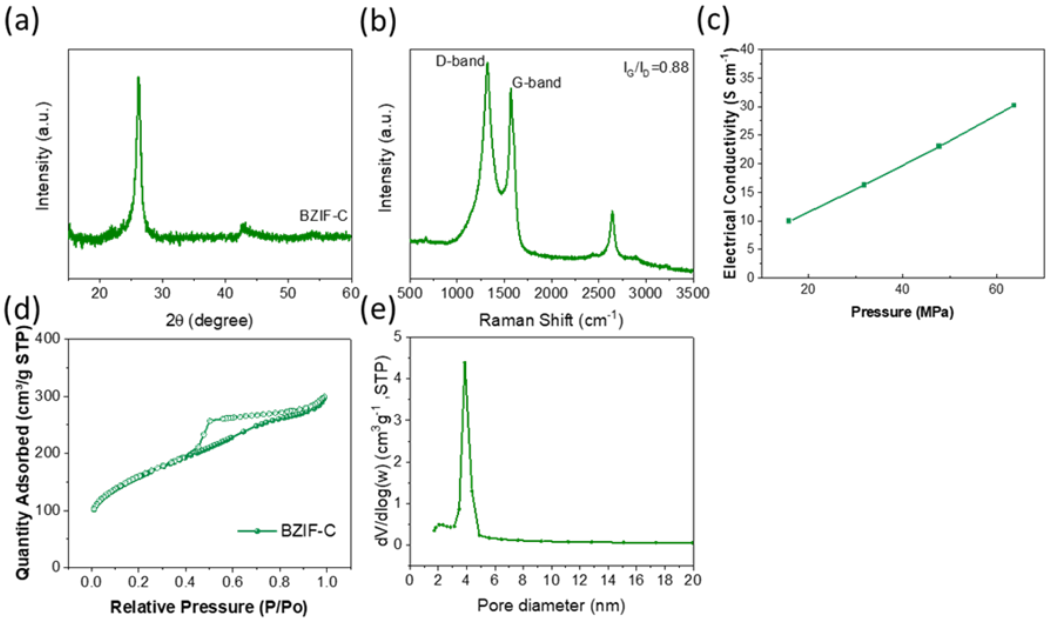

Figure 4.2. (a) XRD pattern and (b) Raman spectrum of BZIF-C. (c) Electrical conductivity of BZIF-C under compressed conditions with different pressures. (d) and (e) N2 adsorption/desorption isotherm and average pore diameter, respectively.

structure. These N defects are quaternary N (401.2 eV), pyrrolic N (400.0 eV), and pyridinic N (398.8eV). These N dopants play an effective role in enhancing the Li affinity of BZIF-C.

4.3.2 DFT Calculations

During Li plating and stripping, different types of Li growth on the surface of BZIF-C were induced, as shown in Figure 4.5(a). The mass transfer of Li starts with the Li ion migration toward the electrode surface and shedding off the solvent molecules to reduce themselves and be transformed into Li adatoms. Subsequently, the Li adatoms diffuse onto the anode surface until they are adsorbed by lithiophilic sites (denoted as heteroatoms). Following that, the Li adatoms form clusters and grow in an axial/ vertical direction, as shown in Figure 4.5(a).

By considering a single Li atom (Figure 4.4(a) and (b)), the DFT calculations show that the relatively weak formation energy value between the Li atom and pristine carbon (-0.140 eV) is because the carbon atoms exist in stable six-membered rings with saturated electron orbitals, so no extra electrons are present to adsorb the Li atom. Interestingly, quaternary N, which has positive adsorption energy of 0.40 eV, remains connected to three carbon atoms in the stable six-membered ring. In this case, the N atom participates in the formation of the π bond, which increases local charge densities and improves electrical conductivity. Hence, such heteroatom types as well as pristine carbon can render high specific interfacial energy and large nucleation barriers, which initiate

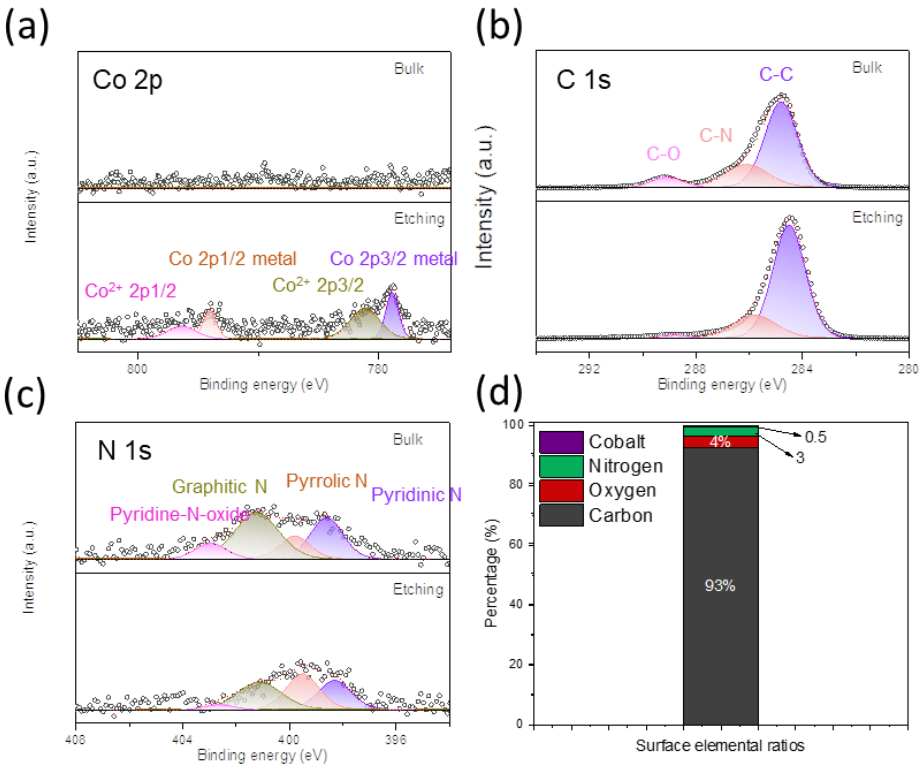

Figure 4.3. (a)-(c) XPS spectra of the BZIF-C measured before and after etching of the sample: Co 2p (a), C 1s (b), and N 1s (c). (d) The surface elemental ratio of the elements is based on the XPS results.

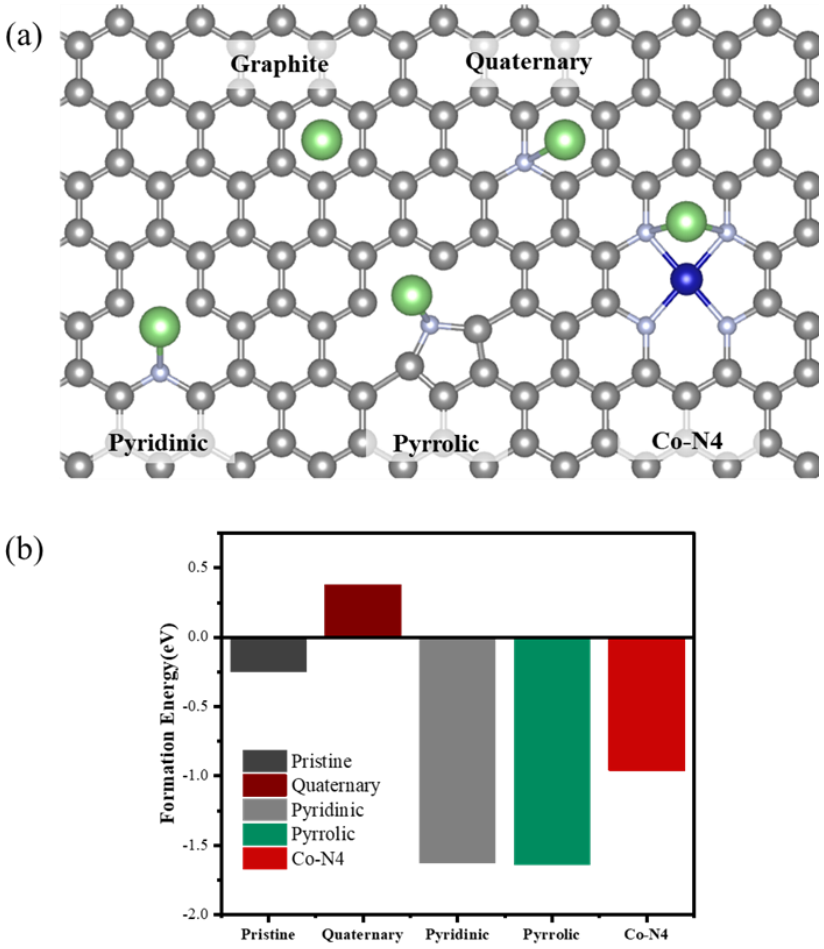

Figure 4.4. (a) Schematic illustration of lithiation sites in graphite and different types of N doped graphite structure: Graphite Quaternary, Pyridinic, Pyrrolic, Co-N4. (b)Formation energies of the Li_1 adsorption on the pristine graphite and on four different defect structures.

unwanted failure mechanisms. For this reason, the pristine carbon and quaternary N can be negligible in the subsequent calculations.

A pyridinic N atom in a six-carbon member ring is co-planar (Figure 4.4(a) and (b)). It conjugates with the π bond and provides an extra electron, while it remains connected to two carbon atoms, offering negative formation energy of -1.741 eV. A pyrrolic N, on the other hand, is a member of a five-carbon member ring connected to two carbon atoms (Figure 4.4(a) and (b)). In such structures, the pyrrolic N atom acts as a Lewis base by providing a lone pair of electrons that can strongly adsorb the Li^+ (Lewis acid)

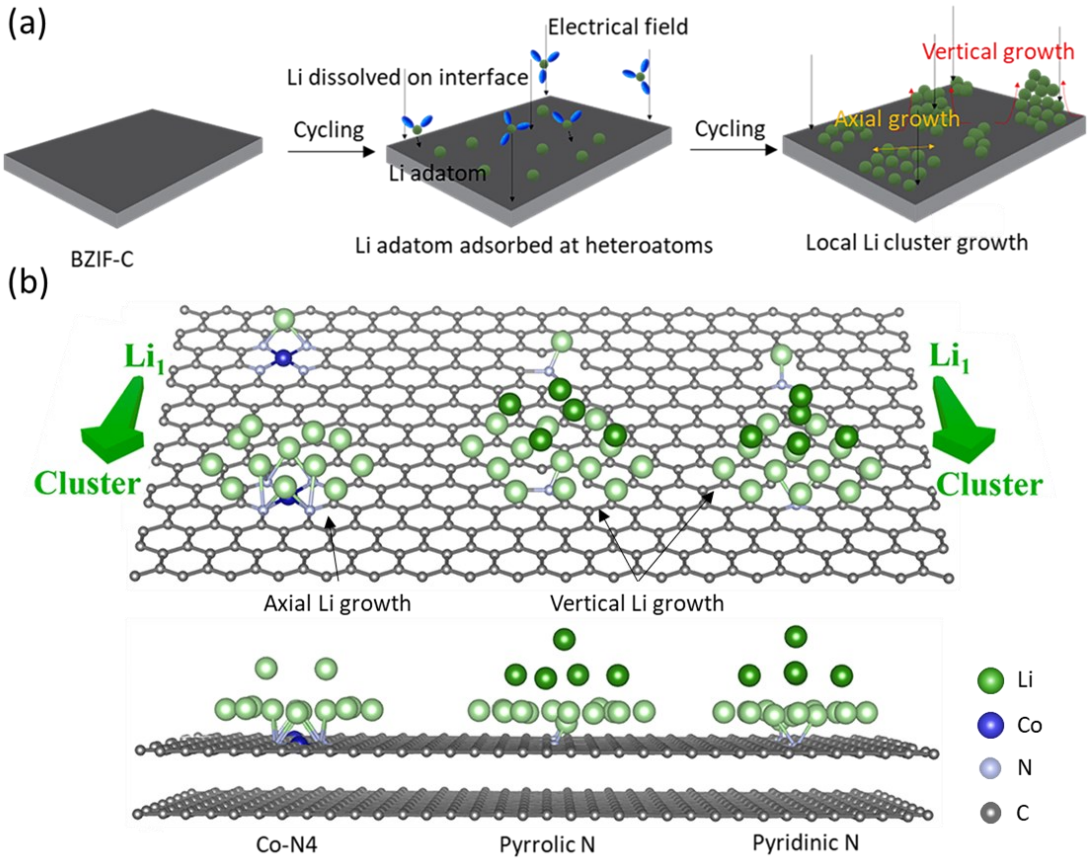

Figure 4.5. (a) Schematic representation of the deposition and growth during the Li plating process. First, Li sheds off the solvent molecules and transforms into Li adatom. Then, the Li cluster forms vertical/axial growth based on the heteroatom type. (b) The structure of Li intercalation from Li_1 to Li clusters (Li metal) with three types of nitrogen doping in graphite defects.

with a formation energy of -1.740 eV. The Co-N4 bond is found to delocalize electrons to neighboring carbon atoms, which enhance the electronegativity of the surface and the interaction between the Li and Co-N4 doped graphite with a Li formation energy of (-0.824 eV).

Li deposition on pyridinic N, pyrrolic N, and Co-N4 can be considered by understanding the behavior of these heteroatoms with respect to a cluster of Li adatoms. Thus, the correlation between the formation energy and the deposition behavior of a single Li atom on a cluster of Li atoms needs to be understood and predicted, as illustrated in Figure 4.5(b), 4.6(a) (atomic configurations) and Figure 4.7(a) (values).

While the low formation energies of pyridinic N and pyrrolic N provide a favorable nucleation process, excessive adsorption of Li adatoms can occur, creating potential centers for Li aggregation and vertical growth (i.e., dendritic growth). In contrast, the predicted deposition of Li atoms with Co-N4 heteroatoms introduces planar growth on the surface of graphitic carbon. This behavior can be explained by the most stable state of Li deposition for each heteroatom type, which defines the morphology of Li growth, regardless of the formation energy value. In other words, the delocalization of the charge in Co-N4 enhances the electronegativity of the surrounding carbon atoms, which allows them to adsorb Li adatoms. Note that nitrogen defects in pyridinic N and pyrrolic

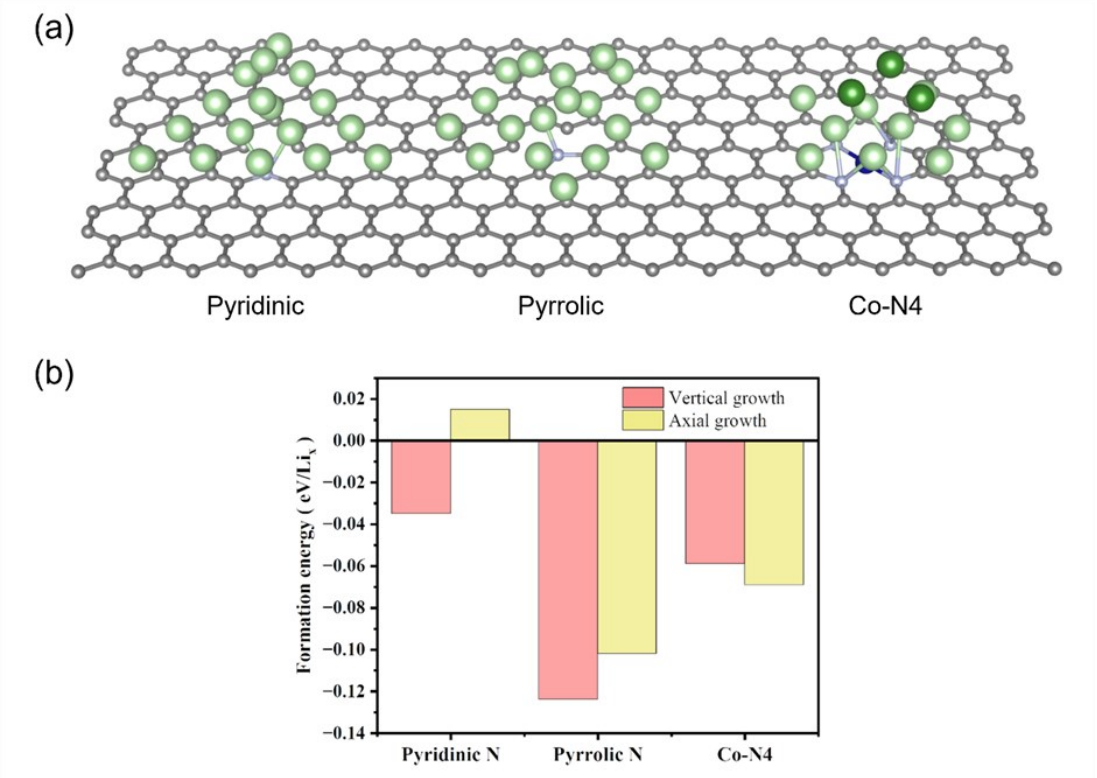

Figure 4.6. (a) Another possibility of atomic configuration of Li growth, showing axial Li growth on pyridinic N and pyrrolic N and vertical Li growth on Co-N4 structure. (b) The formation energy obtained from Figure 4.5(b) and Figure 4.6(a) to compare which of the two Li growth forms (axial or vertical) is more likely to occur on pyridinic N, pyrrolic N and Co-N4 structures. In Co-N4, the formation energy for vertical growth is smaller than that of the axial growth, leading to a tendency for axial Li growth.

N promote congregation on the defect sites only.

Figure 4.8(a – c) and Figure 4.7(a) show the atom-by-atom deposition morphology and the change in the formation energy for the different heteroatoms. The trend shows a

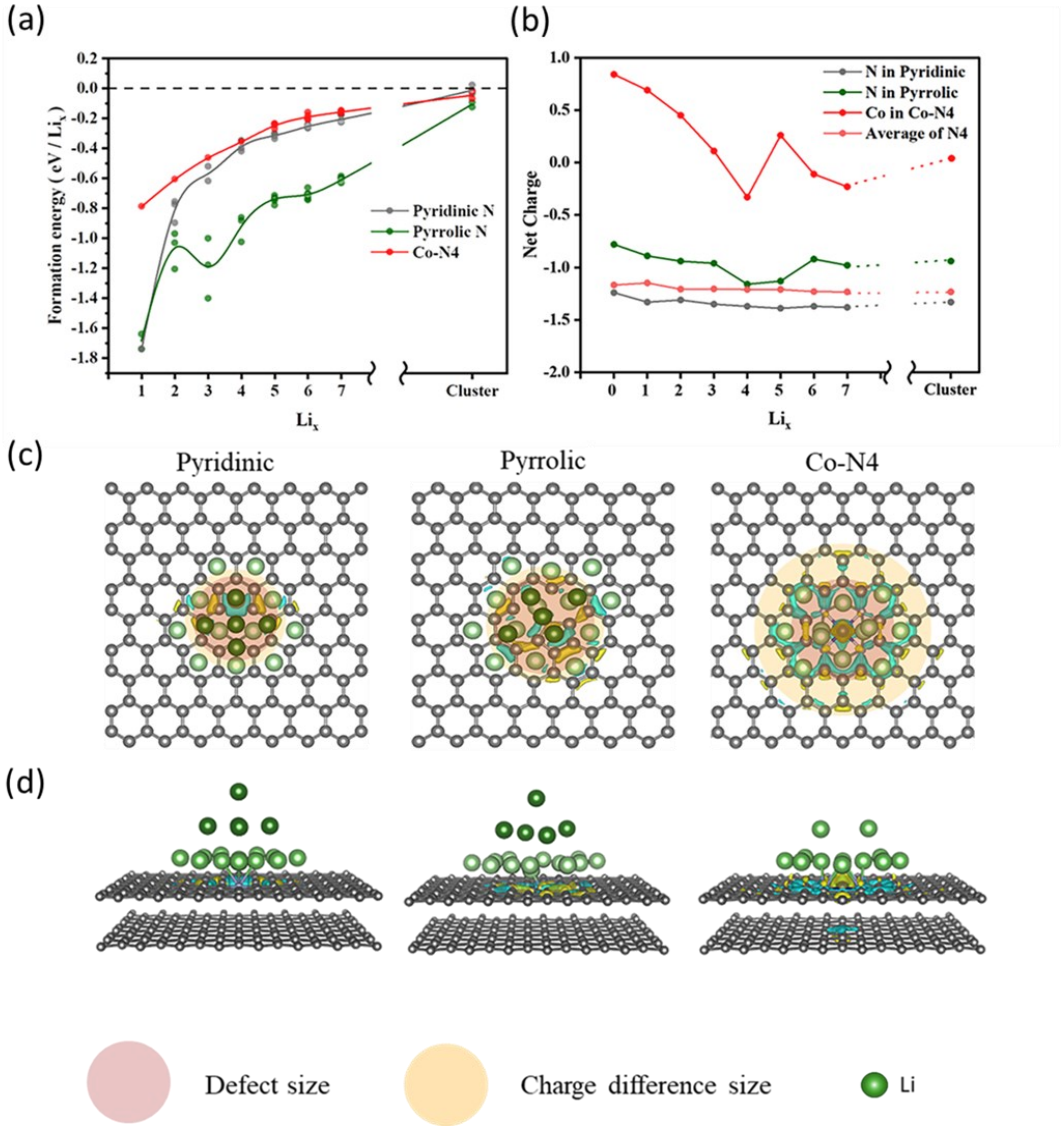

Figure 4.7. (a) The formation energy by the number of Li ions in a cluster and the different sites for Li in three different types of N-doped graphite. (b) Bader net charge of nitrogen and cobalt by number of Li in N-doped graphite. (c) Size of charge density difference and defect size in the form of Li clusters and (d) side views. The red/yellow areas represent the defect/charge density difference sizes, respectively.

sharp increase in the formation energy with additional Li adatoms from one to four in the case of pyridinic N and pyrrolic N, increasing up to 1.35 and 0.8 eV/atom respectively. In the case of Co-N4, however, the change in the formation energy was

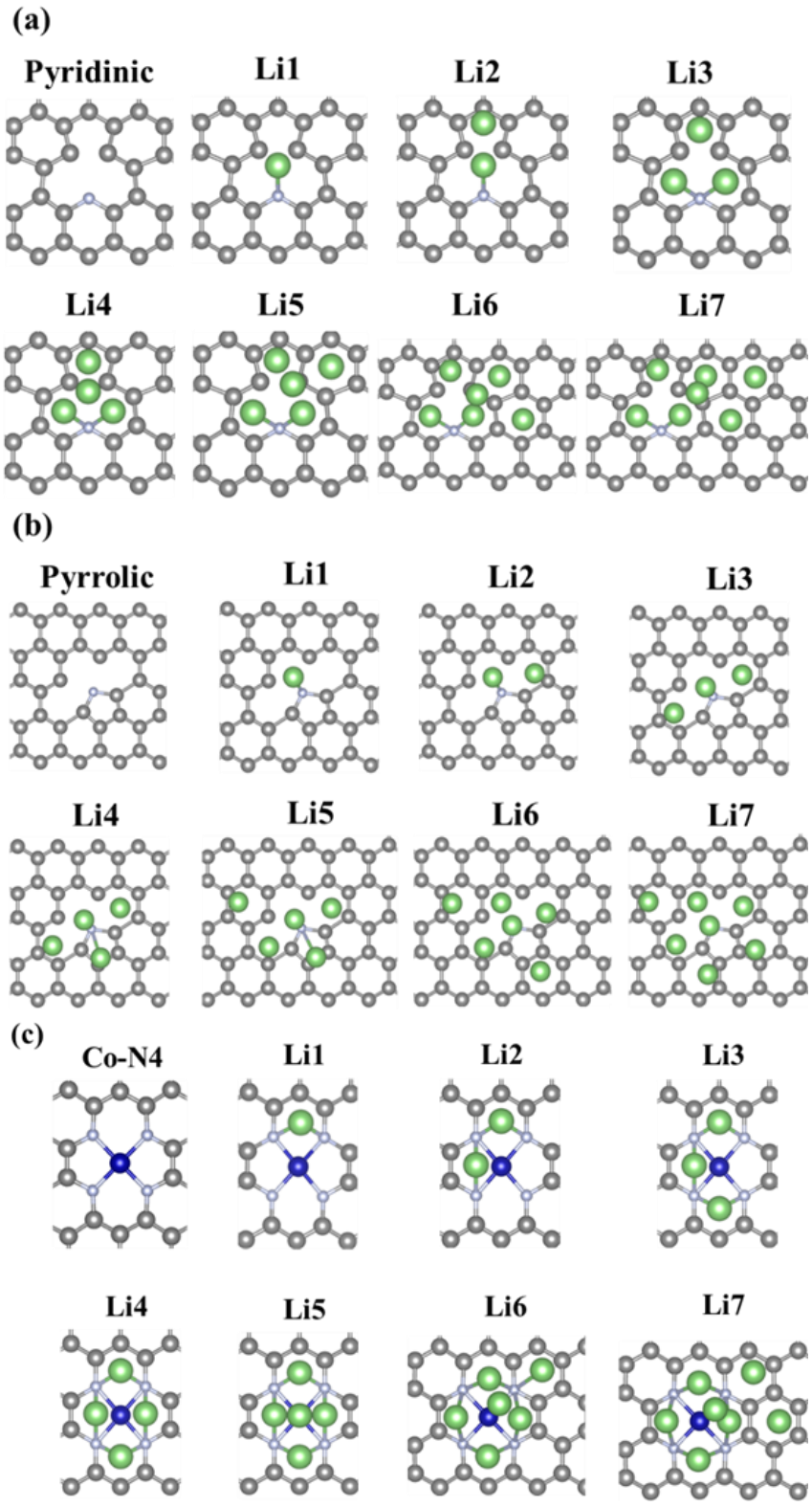

Figure 4.8. (a)-(c) Local structure of lithiation step by number of Li adatoms in stable sites of n/Co doped graphite.

relatively much lower (0.4 eV/atom) in early stage lithiation. This is due to the wider charge distribution among neighboring carbon atoms, as illustrated in Figure 4.7(c) and

(d). In detail, the Co-N4 reduces the Coulombic repulsion between the Li atoms themselves by storing the electrons from Li adatoms. With further lithiation, the formation energies saturate at -0.1 eV, indicating a Li cluster on Co-N4, as confirmed by the Bader net charge analysis, as shown in Figure 4.7(b). The N atoms show almost constant values in net charge: -1.4 (N in pyridinic defect), -0.9 (N in pyrrolic defect) and -1.2 (N4 in Co-N4) with every additional Li adatom, in which the N atoms in the pyridinic and pyrrolic defects act as Lewis bases to adsorb Li^+ (Lewis acid). The N atoms in pyridinic and pyrrolic defects have limits in terms of receiving transferred electrons after the formation of an Li adatom. Electron storage was observed in Co with additional Li adatoms from one to four, while the N4 in Co-N4 also acts as a Lewis base for the adsorption of Li^+ with a saturated net charge (3rd orbital of Co is occupied by lithiation).

It was confirmed that Co plays an active role in reacting with not just a single Li but also with a Li cluster. Furthermore, the charge density difference in Co-N4 calculated by Eq. 1 shows delocalized electron configurations as follows:

$$\rho_{diff} = \rho_{Li_x/BZIF-C} - \left(\rho_{BZIF-C} + \rho_{Li_x}\right) \quad (1)$$

Where, ρ_{diff} is the charge density difference between Li adsorption on Co-N4 doped graphite and on N doped graphite. Figure 4.7(c) and (d) and Figure 4.9(a – c) show the iso-surfaces of charge density difference marked by the yellow circles and the defect areas marked by red circles. Pyridinic N and pyrrolic N show localized electron hybridization with Li adatoms owing to the limits of charge storage on C and N frameworks. In each case, the defect size marked by the red circle and the iso-surface of charge density difference marked by the yellow circle both correspond to a size like that of the area of the circle. This can result in the aggregation of more Li adatoms onto

the same defect site, leading to vertical growth (dendritic growth) on pyridinic N and pyrrolic N, as confirmed in Figure 4.5. It is to be noted that delocalized electron configurations in Co-N4 were observed with Li axial growth in Figure 4.7(c) and (d). The difference in area between the defect size and that of the charge density difference of Co-N4 is relatively wider compared to the other defects. These results confirm that

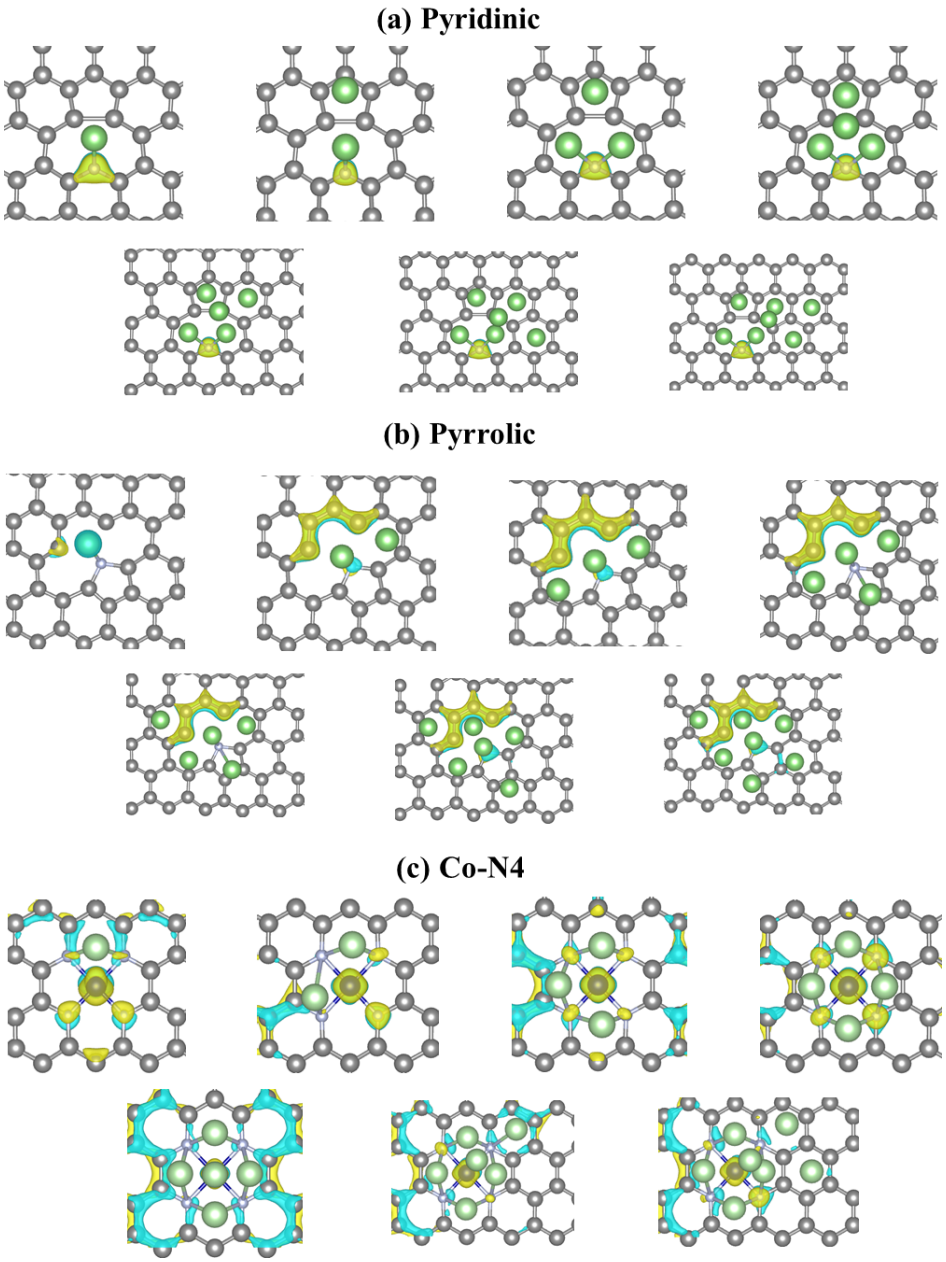

Figure 4.9. Charge density differences when Lis are stored step by step in pyridinic (a), pyrrolic (b), and Co-N4(c) defects.

Co contributes to wide charge transfer within its carbon matrix and enables Li adsorptions with electrons received from Li adatoms. Our calculations elucidate that the Co heteroatom not only leads to the axial growth of Li clusters, but also provides a higher capacity to accommodate Li over the entire graphitic structure.

4.3.3 Experimental Verification

To validate the theoretical results mentioned earlier, we characterized the electrochemical performance of two types of anode materials: (i) BZIF-C and (ii) Cu foil (as a reference). The Li affinity of the anodic materials was firstly evaluated based on the nucleation overpotentials at different applied current densities with a constant charge capacity of 2 mAh cm^{-2} (Figure 4.10(a-c)). The presented data is in line with the main findings of this study, which support the role of lithophilic sites in BZIF-C in maintaining a lower nucleation overpotential with increasing current density. This behavior can be further explained by referring to the classical nucleation and growth theory, which states that, at high current densities, the driving force for electro-crystallization relies on reaction, charge transfer, diffusion, and crystallization overpotentials. Under low current densities, however, the last of these plays the most significant role in the as-obtained nucleation overpotential, which is mainly governed by the Li affinity (heterogeneous nucleation energy barrier) of the anode surface.

Given that investigating the effects of the other driving forces is beyond the scope of this study, we focused on our results at low current densities (0.2 and 0.4 mA cm^{-2}) to relate the Li affinity of the anodic material to its cycling performance. For both current density values, Cu foil anode showed poor Li affinity represented by its arc behavior throughout the cycles (Figure 4.10(d) and (e)). More specifically, the reason behind this significant change in overpotential can be related to the accumulated dead Li on the surface, creating winding pathways for Li^+ ions transport and giving rise to a greater

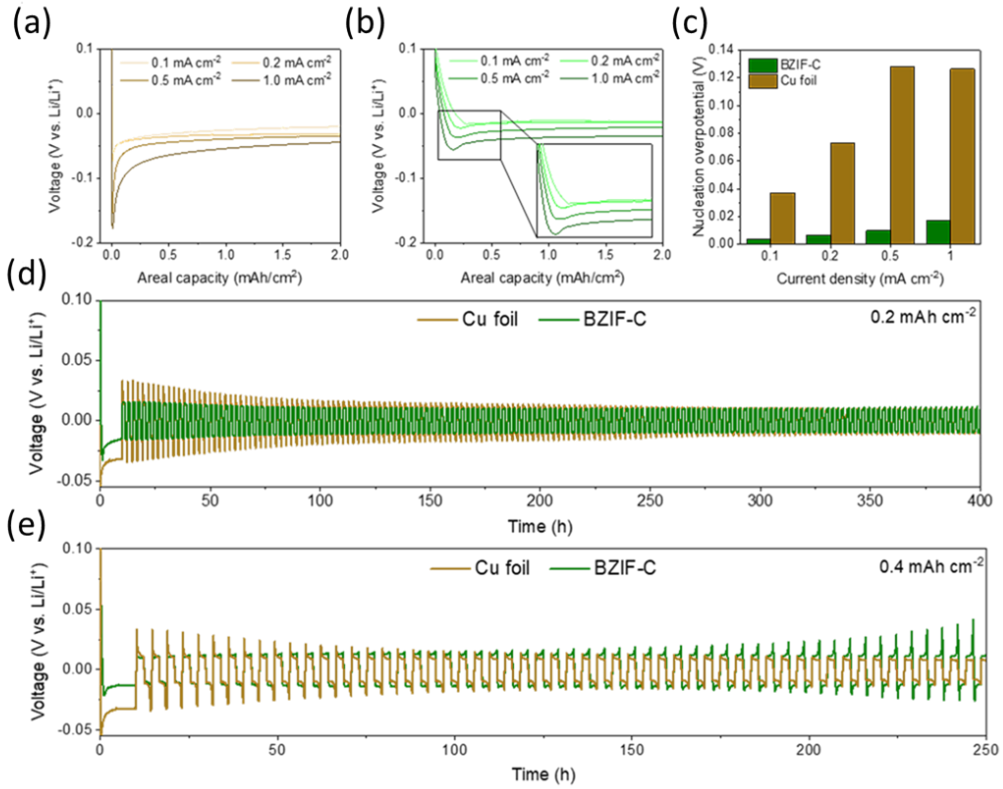

Figure 4.10. (a) and (b) Voltage hysteresis observations in first cycle charging with the areal capacity of 2 mAh cm^{-2} at different current densities. (c) Nucleation overpotential comparison between BZIF-C and Cu foil at different current densities. (d) and (e) Voltage profiles with cycling of the BZIF-C and Cu foil electrodes at 0.2 mA cm^{-2} with different charge/discharge capacities of 0.2 mAh cm^{-2} and 0.4 mAh cm^{-2}, respectively.

concentration gradient. This is supported by the detailed SEM images in Figure 4.11(a) and (b) collected at 0.4 mA cm^{-2} after cycling, which shows a cross-sectional view of the two anode types highlighting clear dendritic growth.

At 0.2 mA cm^{-2}, the galvanostatic voltage profile during cycling of BZIF-C shows almost stable cycling over 400 hours owing to its higher Li affinity as well as its large pore volumes in which metallic Li can be stored (Figure 4.10(d) and (e)). This is because Co-N4 heteroatoms in BZIF-C enable high reversibility and stable Li storage, as suggested by the earlier findings from the DFT calculations. Furthermore, at 0.4 mA cm^{-2}, the voltage profile of BZIF-C was also stable over 150 hours, followed by a slight

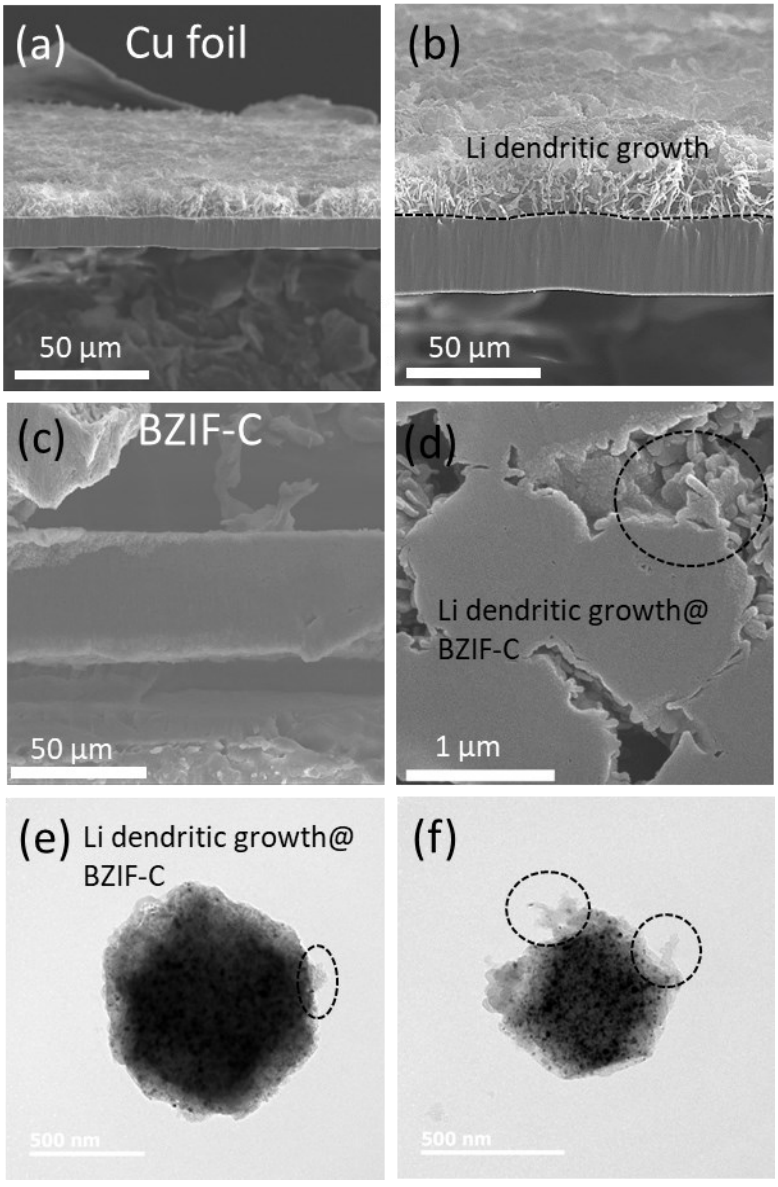

Figure 4.11. Microscopic observations of Li-metal plated Cu foil and BZIF-C. (a) and (b) SEM images of the Cu foil electrode. (c) and (d) SEM of the BZIF-C electrode. (e) and (f) TEM of the BZIF-C.

arcing behavior that gradually increased afterward. This could be related to the aforementioned theoretical assumptions that predict an agglomeration of Li onto pyridinic N and pyrrolic N sites, as evidenced by SEM and TEM (Figure 4.11(d-f)), inducing dendritic Li growth with increasing amounts of Li. This is also explained by the relatively high N content compared to the very low Co content on the surface of BZIF-C, as indicated by the EDS mapping and calculated percentage of the surface elemental ratio of XPS shown in Figure 4.3(d).

Despite the occurrence of Li agglomeration in BZIF-C at relatively high current densities, the practical deposition behavior of Li is not always well represented by half-cell measurements. Thus, the reliability of using BZIF-C in a full cell was examined at various current densities, 0.2, 0.4, and 0.6 mA cm^{-2}, for 100 cycles. Commercially available $LiFePO_4$ (LFP) was employed as the cathode, operating in the voltage range of 2.5-4.0 V. The XPS spectra in Figure 4.12(a) show the main components of the solid electrolyte interphase (SEI), indicating the formation of the LiF-rich SEI. As demonstrated in our previous study, the LiF-rich SEI exhibits favorable properties, such as a low diffusion barrier, superior electronic insulation, and protection against parasitic reactions.[42] Figure 4.12(b) shows the galvanostatic charge and discharge profiles at different current densities for the first cycle of full-cells employing BZIF-C anodes. Among the different current densities, the electrode at 0.2 mA cm^{-2} showed the highest capacity value of 140 mAh g^{-1}, due to the better Li-ion accessibility and reversibility. Figure 4.12(c) shows the cycling performance for LFP || BZIF-C cells at an areal capacity of 0.6 mAh cm^{-2} and different current densities. It was found that the LFP || BZIF-C_0.2 mA cm^{-2} cell notably shows a small decrease in the specific capacity from 140 mAh g^{-1} down to 125 mAh g^{-1} over the course of cycling with a capacity retention of 89% after 100 cycles. In addition, both the LFP || BZIF-C_0.4 mA cm^{-2} and the LFP

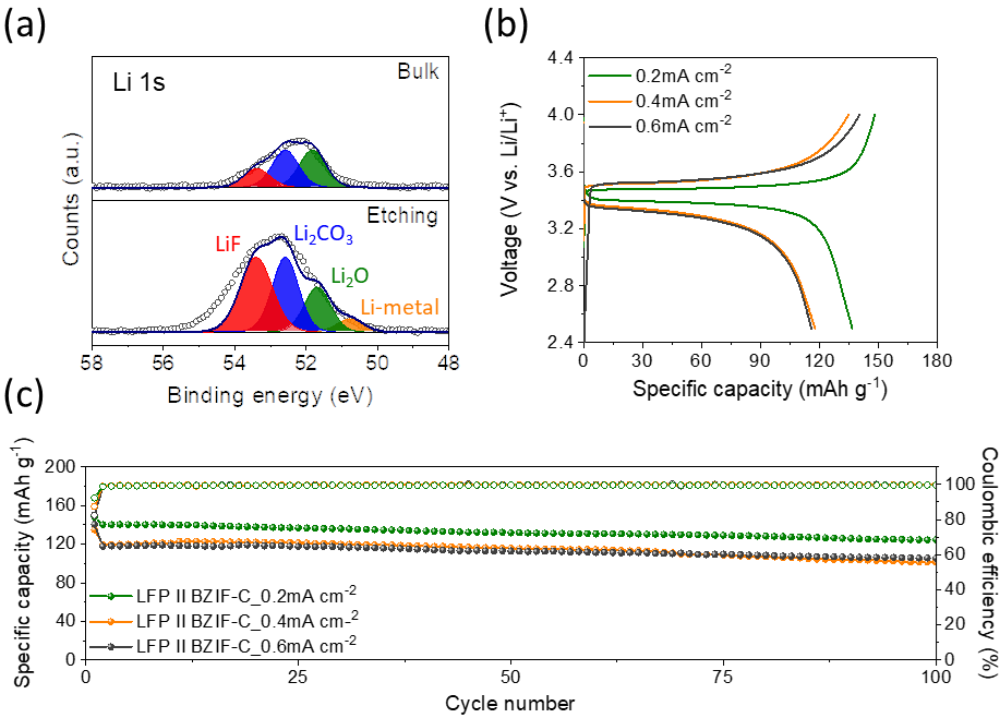

Figure 4.12. (a) Elemental components on the surface of the BZIF-C anode after Li-plating analyzed by X-ray photoelectron spectroscopy (XPS). (b) The first cycle charge-discharge plots of BZIF-C in conjunction with lithium iron phosphate (LFP) cathode at different current densities, and (c) full-cell performance of BZIF-C anode at different current densities.

|| BZIF-C_0.6 mA cm^{-2} cells showed almost the same decrease in the specific capacity, which begins at around 118 mAh g^{-1} with a capacity retention of 88 % and 86%, respectively. Based on the theoretical and experimental findings, we conclude that Co-N4 provides a favorable bond that enables stable Li adsorption. Other investigated heteroatoms, such as pyridinic N and pyrrolic N, disturb the electrochemical performance of the anode, especially at high current densities. Therefore, future iterations of this work can include BZIF-C functionalization with other heteroatoms to enhance its surface chemistry.

4.4 Conclusion

A comprehensive understanding of the deposition behavior of Li adatoms on the surface of the carbon host framework is theoretically demonstrated and experimentally correlated. We found that the N heteroatoms tend to induce Li dendritic growth, while the Co-N4 heteroatoms induce the desired axial Li growth. This is because the Co-N4 heteroatoms can enhance the charge transfer from the metal dopants to the carbon matrix, leading to an electrically rich environment of neighboring carbon and nitrogen atoms. This is well aligned with the experimental results, showing that BZIF-C exhibits significant cycling stability at low areal capacity. while increasing the areal capacity results in less stability and dendritic growth. Such a performance was explained by the relatively small amount of Co-N4 heteroatoms compared to other heteroatoms, as confirmed by XPS and EDS analysis.

Our work is expected to offer a perspective on the understanding of the Li growth mechanism, as well as provide a fundamental framework for designing anodic BZIF-C materials with high-performance. Due to the complexity of the Li adsorption mechanism and the various factors that can influence the growth of Li clusters, however, additional scientific exploration is necessary. This exploration should encompass surface morphology, electrolyte materials and concentration, solvent selection, operating temperature, and cycling duration, among other factors. These variables can impact the number of active sites, solubility and mobility of Li-ions, permeability of the SEI layer, and electrode stability. Therefore, optimizing these variables are crucial for the development of high-performance battery.

4.5 References

(1) Jin, C.-B.; Shi, P.; Zhang, X.-Q.; Huang, J.-Q. Advances in carbon materials for stable lithium metal batteries. *New Carbon Materials* **2022**, *37* (1), 1-24.

(2) Han, S. A.; Qutaish, H.; Lee, J. W.; Park, M. S.; Kim, J. H. Metal-organic framework derived porous structures towards lithium rechargeable batteries. *EcoMat* **2022**, *5* (2), e12283.

(3) Roberts, A. D.; Li, X.; Zhang, H. Porous carbon spheres and monoliths: morphology control, pore size tuning and their applications as Li-ion battery anode materials. *Chemical Society Reviews* **2014**, *43* (13), 4341-4356.

(4) Li, T.; Liu, H.; Shi, P.; Zhang, Q. Recent progress in carbon/lithium metal composite anode for safe lithium metal batteries. *Rare Metals* **2018**, *37* (6), 449-458.

(5) Qutaish, H.; Han, S. A.; Rehman, Y.; Konstantinov, K.; Park, M.-S.; Kim, J. H. Porous carbon architectures with different dimensionalities for lithium metal storage. *Science and Technology of Advanced Materials* **2022**, *23* (1), 169-188.

(6) Shin, H. R.; Yun, J.; Eom, G. H.; Moon, J.; Kim, J. H.; Park, M.-S.; Lee, J.-W.; Dou, S. X. Mechanistic and nanoarchitectonics insight into Li–host interactions in carbon hosts for reversible Li metal Storage. *Nano Energy* **2022**, *95*, 106999.

(7) Yoshino, A. The lithium-ion battery: Two breakthroughs in development and two reasons for the Nobel Prize. *Bulletin of the Chemical Society of Japan* **2022**, *95* (1), 195-197.

(8) Han, S. A.; Qutaish, H.; Park, M. S.; Moon, J.; Kim, J. H. Strategic approaches to the dendritic growth and interfacial reaction of lithium metal anode. *Chemistry–An Asian Journal* **2021**, *16* (24), 4010-4017.

(9) Zou, P.; Sui, Y.; Zhan, H.; Wang, C.; Xin, H. L.; Cheng, H.-M.; Kang, F.; Yang, C. Polymorph evolution mechanisms and regulation strategies of lithium metal anode under multiphysical fields. *Chemical Reviews* **2021**, *121* (10), 5986-6056.

(10) Zhang, L.; Zhu, C.; Yu, S.; Ge, D.; Zhou, H. Status and challenges facing representative anode materials for rechargeable lithium batteries. *Journal of Energy Chemistry* **2022**, *66*, 260-294.

(11) Wang, Q.; Liu, B.; Shen, Y.; Wu, J.; Zhao, Z.; Zhong, C.; Hu, W. Confronting the challenges in lithium anodes for lithium metal batteries. *Advanced Science* **2021**, *8* (17), 2101111.

(12) Wang, J.; Ge, B.; Li, H.; Yang, M.; Wang, J.; Liu, D.; Fernandez, C.; Chen, X.; Peng, Q. Challenges and progresses of lithium-metal batteries. *Chemical Engineering Journal* **2021**, *420*, 129739.

(13) Zhang, X.; Yang, Y.; Zhou, Z. Towards practical lithium-metal anodes. *Chemical Society Reviews* **2020**, *49* (10), 3040-3071.

(14) Luo, Z.; Qiu, X.; Liu, C.; Li, S.; Wang, C.; Zou, G.; Hou, H.; Ji, X. Interfacial challenges towards stable Li metal anode. *Nano Energy* **2021**, *79*, 105507.

(15) Ruan, P.; Liang, S.; Lu, B.; Fan, H. J.; Zhou, J. Design strategies for high-energy-density aqueous zinc batteries. *Angewandte Chemie* **2022**, *134* (17), e202200598.

(16) Hosaka, T.; Komaba, S. Development of nonaqueous electrolytes for high-voltage K-ion batteries. *Bulletin of the Chemical Society of Japan* **2022**, *95* (4), 569-581.

(17) Hyeon, Y.; Lee, J.; Qutaish, H.; Han, S. A.; Choi, S. H.; Moon, S. W.; Park, M.-S.; Whang, D.; Kim, J. H. Lithium metal storage in zeolitic imidazolate framework derived nanoarchitectures. *Energy Storage Materials* **2020**, *33*, 95-107.

(18) Ye, H.; Xin, S.; Yin, Y. X.; Guo, Y. G. Advanced porous carbon materials for high-efficient lithium metal anodes. *Advanced Energy Materials* **2017**, *7* (23), 1700530.

(19) Chen, X.; Chen, X.-R.; Hou, T.-Z.; Li, B.-Q.; Cheng, X.-B.; Zhang, R.; Zhang, Q. Lithiophilicity chemistry of heteroatom-doped carbon to guide uniform lithium nucleation in lithium metal anodes. *Science advances* **2019**, *5* (2), eaau7728.

(20) Zhong, Y.; Zhou, S.; He, Q.; Pan, A. Architecture design principles for stable electrodeposition behavior-towards better alkali metal (Li/Na/K) anodes. *Energy Storage Materials* **2022**, *45*, 48-73.

(21) Ghazi, Z. A.; Sun, Z.; Sun, C.; Qi, F.; An, B.; Li, F.; Cheng, H. M. Key aspects of lithium metal anodes for lithium metal batteries. *Small* **2019**, *15* (32), 1900687.

(22) Li, H.; Dong, W.; Li, C.; Barakat, T.; Sun, M.; Wang, Y.; Wu, L.; Wang, L.; Xia, L.; Hu, Z.-Y. Three-dimensional ordered hierarchically porous carbon materials for high performance Li-Se battery. *Journal of Energy Chemistry* **2022**, *68*, 624-636.

(23) Park, S. J.; Yang, S. Y.; Han, S. A.; Choi, Y. J.; Kim, T.; Park, M.-S.; Kim, J. H.; Kim, K. J. Two-in-one separator capturing and reutilizing polysulfides for high performance lithium-sulfur batteries. *Chemical Engineering Journal* **2023**, 141620.

(24) Choi, S. H.; Hyeon, Y.; Shin, H. R.; Eom, G. H.; Pham, H. T. T.; Whang, D.; Kim, S. Y.; Lee, J.-W.; Kim, J. H.; Park, M.-S. Critical role of surface craters for improving the reversibility of Li metal storage in porous carbon frameworks. *Nano Energy* **2021**, *88*, 106243.

(25) Qutaish, H.; Lee, J.; Hyeon, Y.; Han, S. A.; Lee, I.-H.; Heo, Y.-U.; Whang, D.; Moon, J.; Park, M.-S.; Kim, J. H. Design of cobalt catalysed carbon nanotubes in bimetallic zeolitic imidazolate frameworks. *Applied Surface Science* **2021**, *547*, 149134.

(26) Lee, J.; Choi, S. H.; Qutaish, H.; Hyeon, Y.; Han, S. A.; Heo, Y.-U.; Whang, D.; Lee, J.-W.; Moon, J.; Park, M.-S. Structurally stabilized lithium-metal anode via surface chemistry engineering. *Energy Storage Materials* **2021**, *37*, 315-324.

(27) Qutaish, H.; Suh, J. H.; Han, S. A.; Kim, S.; Park, M.-S.; Kim, J. H. Regulation of ionic conductivity and lithium affinity of porous carbon framework in Li metal batteries through oxidized nitrogen groups. *Applied Surface Science* **2022**, *605*, 154757.

(28) Shin, H. R.; Kim, S.; Park, J.; Kim, J. H.; Park, M.-S.; Lee, J.-W. Electrode-Level Strategies Enabling Kinetics-Controlled Metallic Li Confinement by the Heterogeneity of Interfacial Activity and Porosity. *Energy Storage Materials* **2023**.

(29) Qian, L.; Zheng, Y.; Or, T.; Park, H. W.; Gao, R.; Park, M.; Ma, Q.; Luo, D.; Yu, A.; Chen, Z. Advanced Material Engineering to Tailor Nucleation and Growth towards Uniform Deposition for Anode-Less Lithium Metal Batteries. *Small* **2022**, *18* (50), 2205233.

(30) Liu, H.; Cheng, X.-B.; Jin, Z.; Zhang, R.; Wang, G.; Chen, L.-Q.; Liu, Q.-B.; Huang, J.-Q.; Zhang, Q. Recent advances in understanding dendrite growth on alkali metal anodes. *EnergyChem* **2019**, *1* (1), 100003.

(31) Cheng, X.-B.; Zhang, R.; Zhao, C.-Z.; Zhang, Q. Toward safe lithium metal anode in rechargeable batteries: a review. *Chemical reviews* **2017**, *117* (15), 10403-10473.

(32) Chen, X. R.; Zhao, B. C.; Yan, C.; Zhang, Q. Review on Li deposition in working batteries: from nucleation to early growth. *Advanced Materials* **2021**, *33* (8), 2004128.

(33) Ren, Q.; Wang, H.; Lu, X. F.; Tong, Y. X.; Li, G. R. Recent progress on MOF-derived heteroatom-doped carbon-based electrocatalysts for oxygen reduction reaction. *Advanced Science* **2018**, *5* (3), 1700515.

(34) Li, C.; Dong, S.; Tang, R.; Ge, X.; Zhang, Z.; Wang, C.; Lu, Y.; Yin, L. Heteroatomic interface engineering in MOF-derived carbon heterostructures with built-in electric-field effects for high performance Al-ion batteries. *Energy & Environmental Science* **2018**, *11* (11), 3201-3211.

(35) Hu, A.; Zhou, M.; Lei, T.; Hu, Y.; Du, X.; Gong, C.; Shu, C.; Long, J.; Zhu, J.; Chen, W. Optimizing redox reactions in aprotic lithium–sulfur batteries. *Advanced Energy Materials* **2020**, *10* (42), 2002180.

(36) Rao, X.; Lou, Y.; Zhong, S.; Wang, L.; Li, B.; Xiao, Y.; Peng, W.; Zhong, X.; Huang, J. Strategies for Dendrite-Free lithium metal Anodes: A Mini-review. *Journal of Electroanalytical Chemistry* **2021**, *897*, 115499.

(37) Lee, S. W.; Choi, B. J.; Eom, T.; Han, J. H.; Kim, S. K.; Song, S. J.; Lee, W.; Hwang, C. S. Influences of metal, non-metal precursors, and substrates on atomic layer deposition processes for the growth of selected functional electronic materials. *Coordination Chemistry Reviews* **2013**, *257* (23-24), 3154-3176.

(38) Chang, H.; Park, M.-S.; Kim, J. H.; Moon, J. Defect mediated lithium adsorption on graphene-based silicon composite electrode for high capacity and high stability lithium-ion battery. *Journal of Electroanalytical Chemistry* **2023**, 117179.

(39) Kresse, G.; Furthmüller, J. Efficient iterative schemes for ab initio total-energy calculations using a plane-wave basis set. *Physical review B* **1996**, *54* (16), 11169.

(40) Perdew, J. P.; Burke, K.; Ernzerhof, M. Generalized gradient approximation made simple. *Physical review letters* **1996**, *77* (18), 3865.

(41) Henkelman, G.; Arnaldsson, A.; Jónsson, H. A fast and robust algorithm for Bader decomposition of charge density. *Computational Materials Science* **2006**, *36* (3), 354-360.

(42) Lee, J.; Park, M.-S.; Kim, J. H. Stabilizing Li-metal host anode with LiF-rich solid electrolyte interphase. *Nano Convergence* **2021**, *8* (1), 1-8.

CHAPTER 5 . REGULATION OF IONIC CONDUCTIVITY AND LITHIUM AFFINITY OF POROUS CARBON FRAMEWORK IN LI METAL BATTERIES THROUGH OXIDIZED NITROGEN GROUPS

5.1. Introduction

During the past decade, lithium-ion batteries (LIBs) have become a primary power source for a wide range of electrical devices owing to their high energy density, durability, and environmental friendliness [1]. However, current LIBs still suffer from their limited capacity to store electrochemical energy because of the limitations of their storage mechanism (i.e. intercalation). Unfortunately, they are not suitable for powering long-range electric vehicles (EVs) at this moment due to their lengthy charging cycle and short operating time [3].

Lithium (Li) is deemed to be one of the most promising anode materials for LIBs owing to its lightweight (0.53 g cm-3), high theoretical specific capacity (3860 mAh g-1), and low redox potential compared to other alkali metals (-3.04 V vs. standard hydrogen electrode) [2-5]. The fact that Li is highly reactive as well as being susceptible to dendritic growth and infinite volume changes, however, limits its applicability as an anode material [6, 7]. To address these issues, porous carbon materials have been designed and utilized as three-dimensional host materials to accommodate metallic Li, thus increasing the safety and stability of the anode. Nevertheless, the chemical

composition of the porous carbon materials can typically affect the Li affinity and the composition of the solid electrolyte interphase (SEI) [2, 3, 6-9].

Theoretically, three basic parameters, in terms of the chemical composition of the host material, are considered to improve the lithium affinity of anode material, including electronegativity, charge transfer, and local dipoles [7, 10]. The key findings suggest that some functional groups increase the Li nucleation overpotential while others provide high electronegativity towards Li, which results in a lower nucleation barrier. Modifying the local dipole parameter by co-doping is another strategy to enhance Li affinity. Finally, it was found that the charge transfer plays a critical role in decreasing the nucleation barrier energy, where a charge transfer of 0.9 e^- is the threshold for increasing the binding energy [5, 10]. On the other hand, the chemical composition of the porous carbon affects the heterogeneous phases of the SEI itself [7, 11]. The critical role of the SEI revolves around maintaining a stable battery performance, which is governed by the ionic conductivity and mechanical strength of the SEI. More specifically, the morphology of Li deposits relies on the Li^+ transference number, as it was found that a dense and thick deposition morphology is associated with a high Li^+ transference number [12, 13]. In contrast, an SEI with low ionic conductivity induces irregular deposition of metallic Li with loosely packed dendritic structures. The composition of the SEI also has a significant impact on its structural modulus. For example, a lack of LiF and Li_2CO_3 creates a weak SEI that is easier to fracture at weak points [4, 11, 13, 14].

In this chapter, we further improved a porous carbon host derived from a bimetallic zeolitic imidazolate framework (ZIF) composed of ZIF-8 and ZIF-67. The porous carbon (denoted as BZIF-C-F) was functionalized by utilizing HNO_3 to enhance the wettability of the anode through enrichment in nitrogen (N) and improving the ionic

conductivity of the SEI in comparison with a non-functionalized porous carbon (denoted as BZIF-C). We found that BZIF-C-F became functionalized with oxidized nitrogen groups, which catalyzed Li_3N within the SEI, thus improving the ionic conductivity. BZIF-C-F also demonstrated an enhanced Li affinity compared to its non-functionalized counterpart. Even though $LiNO_3$ as an additive in the electrolyte is known to improve ionic conductivity, the cell performance is not maximized. In this chapter, the nitrogen-rich porous carbon host was realized through HNO_3 treatment.

5.2. Materials and methods

5.2.1. Synthesis of BZIF-C

A 50 ml of 2.43 M of 2-methylimidizole in deionized (DI) water was prepared as solution (A). 25 ml of solution (B) was made up of cobalt acetate dissolved in DI water with a concentration of 0.231 M. 25 ml of solution (C) was made up of zinc acetate dihydrate dissolved in DI water (0.116 M). Solutions B and C were mixed and stirred for 5 min. After that, solution A was added to the mixture with continuous stirring for 15 min. The resulting solution was stored at room temperature overnight. The purple precipitate was collected and washed 5 times with DI water and methanol. Then, it was dried in an oven overnight at 60 ℃. The BZIF powder was carbonized at 1000 ℃ with a heating rate of 2 ℃ min^{-1} for 5 hours in an N_2 environment. The resulted BZIF-C was then collected and washed with 1 M HCl two times. Finally, the BZIF-C was dried at 100 ℃ inside a vacuum oven overnight.

5.2.2. Functionalized BZIF-C

1 g of BZIF-C was added to a 100 ml solution consisting of 1 M nitric acid and was stirred for 48 h at room temperature. After that, the BZIF-C was collected and washed with DI water and methanol several times. The functionalized BZIF-C was then

dried and activated under vacuum at 100 ºC for 24 h. The final product (BZIF-C-F) was then collected.

5.2.3. Characterization

The microstructures and morphology of BZIF-C and BZIF-C-F were investigated utilizing field-emission scanning electron microscopy (FE-SEM), and transmission electron microscopy (TEM) in addition to energy dispersive spectroscopy (EDS). X-ray diffraction (XRD) with monochromatic Cu Kα radiation (λ= 1.54056 A), Raman spectroscopy, and X-ray photoelectron spectroscopy (XPS) were all used to examine the crystal structure and chemical composition of the materials. The total pore volumes and surface areas of the materials were calculated with a porosity analyzer. A powder resistivity measurement system was used to obtain the electrical properties of the materials.

5.2.4. Electrochemical measurements

Both the BZIF-C and the BZIF-C-F (80 wt%) were converted into slurries to fabricate the electrodes, in addition to a conducting agent (Super P, 10 wt%) and a binder (poly-vinylidene fluoride, PVdF, 10 wt%) in an N-methyl-2-pyrrolidone (NMP) solution. The slurries were casted onto a thin Cu current collector and dried overnight under vacuum at 120 ℃. Then, they were pressed at 200 kg cm^{-2}. CR2032 coin-type cells were constructed with Li metal foil as the counter electrode. The separator was polyethylene membrane, and the electrolyte consisted of 1 M Li bis(trifluoromethanesulfonyl) imide (LiTFSI) in dioxolane-dimethyl ether (DOL-DME; 50:50 v/v), including 1 wt% $LiNO_3$ as an additive. In addition, full cells were assembled with a commercial $LiFePO_4$ (LFP) cathode and then cycled with a current density of 0.2 mA cm^{-2} in the voltage range of 2.5−4.0 V.

5.2.5. Calculations

The lithium storage mechanism could be estimated according to the following equations:

$$i(v) = i_{\text{cap}} + i_{\text{diff}} = av^b, \qquad (1)$$

$$log\ i(v) = log\ a + b\ log\ v, \qquad (2)$$

where i is the current, v is the scan rate, and a and b are adjustable parameters. Parameter b is determined from the slope of the linear plot of log i versus log v and is used to provide kinetic information about the electrochemical reactions. When the b value approaches 1, it means contributions from fast near-surface activities, such as fast surface redox reactions and charging/discharging of electric double layer capacitors (EDLCs). When the b value is close to 0.5, it means slow semi-infinite diffusion-controlled faradaic processes that occur in the bulk. The smaller the b value is, the larger the contribution from diffusion-controlled intercalation processes will be, while the capacitive contribution increases with increasing b value. If the b-value is between 0.5 and 1, the process is controlled by the synergic effect of the electrochemical process and the capacitive process.

5.3. Results and discussion

Figure 5.1 and figure 5.2 demonstrate the rhombic dodecahedral shape of the BZIF-C and BZIF-C-F particles, with an average particle size of around 650 nm in both samples. The energy dispersive spectroscopy (EDS) results on the BZIF-C and BZIF-C-F indicate the presence of carbon, nitrogen, cobalt, and zinc elements. Note that the content of nitrogen in BZIF-C-F is obviously richer than in BZIF-C. The microstructures of both samples were confirmed via X-ray diffraction (XRD) patterns.

Figure. 5.3(a) shows a significant peak located at 2θ = 26.5°, which corresponds to the (002) planes of graphitic carbon. The Raman spectra in Figure 5.3(b) demonstrate two characteristic signals of defect-rich carbon, which are the D-band at 1343 cm^{-1} and the G-band at 1594 cm^{-1}. In addition, BZIF-C-F shows higher electrical conductivity compared to BZIF-C at different applied pressures, as shown in figure 5.3(c), and the difference reaches one order of magnitude at 20 MPa.

The N_2 adsorption curves in figure 5.4(a) of BZIF-C and BZIF-C-F present typical type-IV isotherms, from which the pore volume, Brunauer-Emmett-Teller (BET) surface area, and average pore radius were obtained to be 0.47 $cm^3\ g^{-1}$, 565.2 $m^2\ g^{-1}$, and 3.7 nm, respectively (figure 5.4b-c). It was found that there was a non-significant microstructure or morphological change for porous carbon hosts before and after functionalization. To investigate the change in heteroatoms after functionalization and

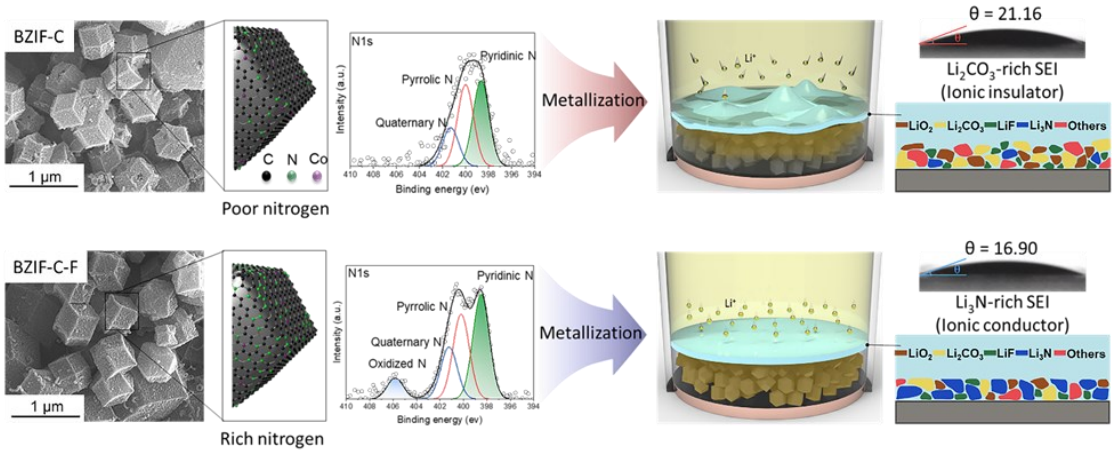

Figure 5.1. Scanning electron microscope (SEM) images showing the morphology of BZIF-C and BZIF-C-F. The enlarged schematic illustrations demonstrate the main elements on the surfaces of these materials. The XPS spectra show the main difference between the two samples. The schematic illustrations on the right show the behaviour of the functionalized material compared to its non-functionalized counterpart in terms of Li affinity and deposition uniformity.

the effect of that on the wettability of the anode, X-ray photoelectron spectroscopy (XPS) analysis was further conducted on both BZIF-C and BZIF-C-F.

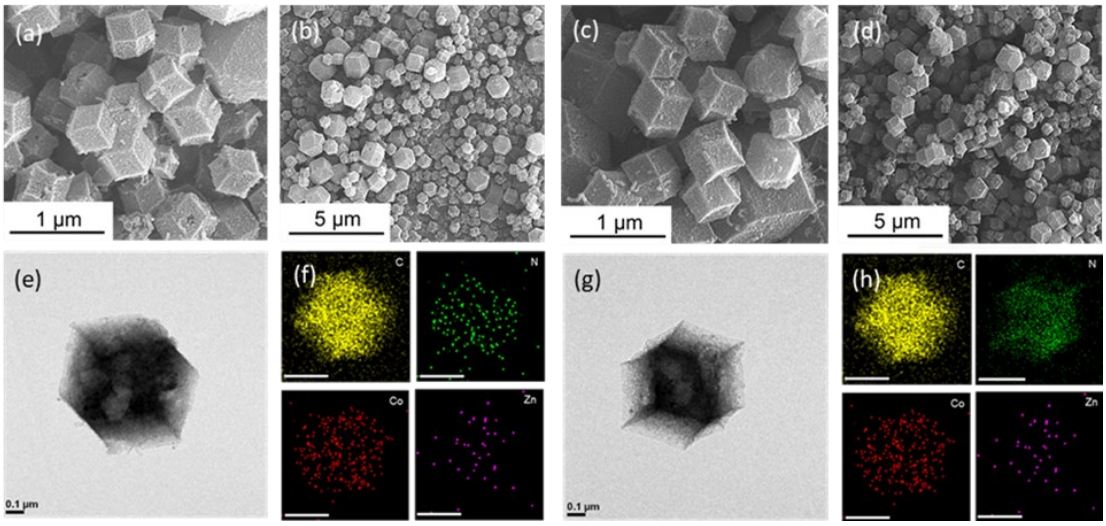

Figure 5.2. SEM images of (a-b) BZIF-C and (c -d) BZIF-C-F. TEM and EDS mapping images of (e-f) BZIF-C and (g-h) BZIF-C-F, showing the elemental content in the material. EDX scale bars are 500 nm.

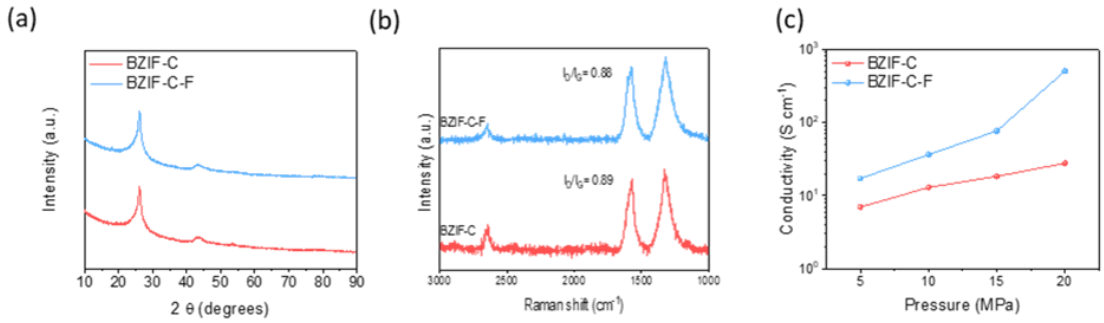

Figure 5.3. (a) XRD spectra, (b) Raman spectra, (C) electrical conductivity.

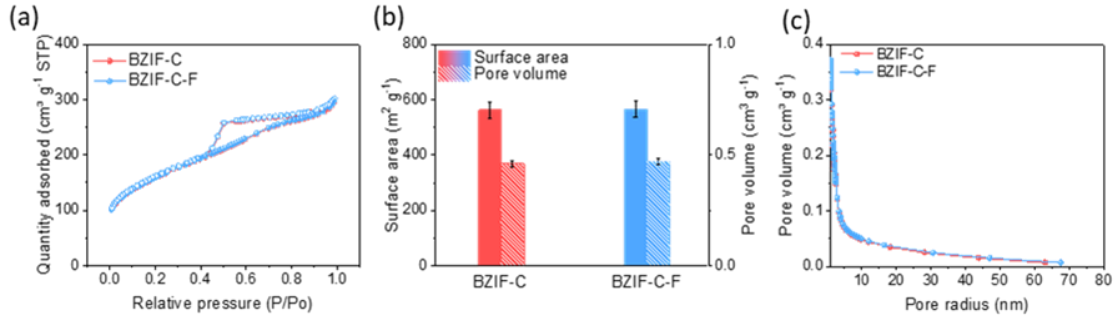

Figure 5.4. (a) N2 adsorption-desorption isotherms, (b) specific surface area and pore volume, and (c) pore size distribution of BZIF-C and BZIF-C-F.

Table 5.1 shows that the areal ratios for both BZIF-C and BZIF-C-F are nearly equal in terms of carbon (95%), oxygen (3%), cobalt (0.06%), and zinc (0.02%). Notably, nitrogen is 0.95% for BZIF-C and 2.22% for BZIF-C-F, which is in good agreement with the EDS results. For further investigation, the XPS spectra of N 1s were analyzed, showing three typical peaks of pyridinic N (398 eV), pyrrolic N (400 eV), and quaternary N (401 eV).

It should be noted that only BZIF-C-F shows an additional peak at 406 eV, indicating the presence of oxidized nitrogen, as shown in figure 5.1 and figure 5.5(a-b). In contrast, the ratios of functional groups in BZIF-C and BZIF-C-F were very similar, as shown in figure 5.5(c-d). The heteroatom dopants in the carbon planes act as active sites to accommodate Li^+ in a pseudocapacitive manner. According to our previous studies [15-17], the formation energy for Li adsorption can be further lowered by enhancing the Li affinity of ZIF surfaces, using both N and Co dopants. More specifically, Co-N (i.e., CoN_x) bonds have been found to delocalize electrons to the neighboring C atoms, which enhances the electronegativity of the surface and the interaction between the Li^+ and Co-N doped graphitic carbon. Additionally, the pyridinic N atom in the six-carbon-

Table 5.1. The areal ratios (%) of different elements utilizing XPS analysis.

Elements	BZIF-C	BZIF-C-F
Carbon	95.52	94.85
Oxygen	3.45	2.84
Nitrogen	0.95	2.22
Cobalt	0.05	0.07
Zinc	0.03	0.02

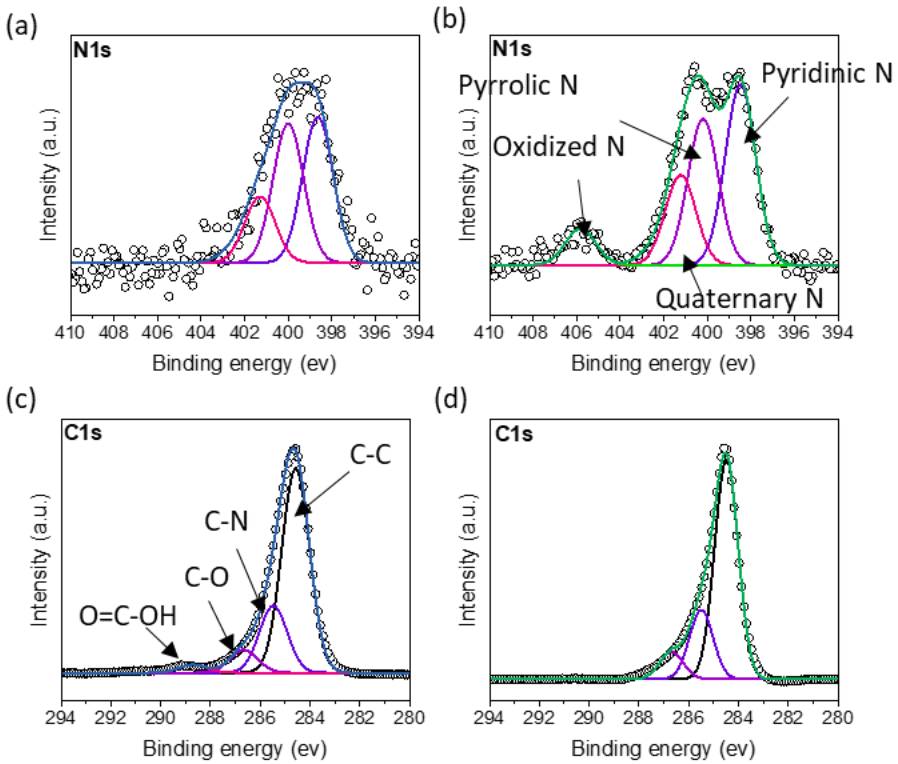

Figure 5.5. XPS analysis of N 1s spectra of (a) BZIF-C and (b) BZIF-C-F electrodes, and C 1s spectra of (c) BZIF-C and (d) BZIF-C-F.

member ring is co-planar, and it conjugates with the π bond to provide an extra electron, as it remains connected to two carbon atoms. It should be noted that the pyrrolic N is a member in the five-carbon ring connected to two carbon atoms. Therefore, the pyrrolic N atom acts as a Lewis base by providing a lone pair of electrons that can strongly adsorb the Li^+ (Lewis acid) [10, 18].

To validate the aforementioned results, wettability measurements were conducted for both BZIF-C and BZIF-C-F. The result indicates a slight improvement in the wettability of the BZIF-C-F compared to the BZIF-C, for which the contact angle decreased from 21.16° to 16.90° (figure 5.1).

This result indicates that the lithiophilicity of the surface of BZIF-C-F can be enhanced by introducing the oxidized nitrogen groups. In terms of the electrochemical performance, the nucleation overpotential curves for BZIF-C and BZIF-C-F were

compared at different current densities. They exhibit delayed and rounded peak shapes (figure 5.6(a) and figure 5.7(a-b)) which are primarily attributed to the lithiation reactions associated with carbon materials and the deposition of metallic Li (below 0 V vs. Li/Li^+) on the surfaces of both samples.

During the Li plating, both sample types showed a significant difference in nucleation overpotential especially for the current densities of 0.1 and 0.2 mA cm^{-2} (figure 5.7(c)). The relative decrease in nucleation overpotential for BZIF-C-F at different current densities aligns well with the wettability results. The reason behind such enhancement is based on the functionalization of chemical composition of the surface with oxidized

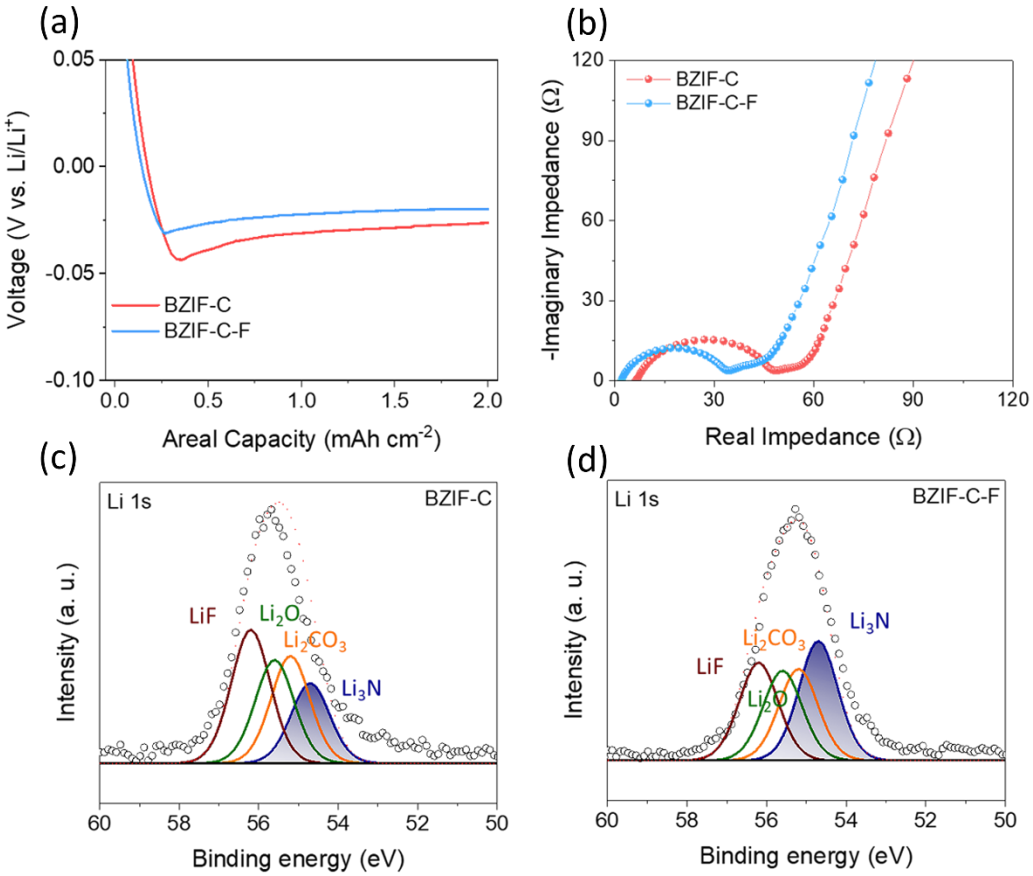

Figure 5.6. (a) Voltage hysteresis observations of both samples in the first cycle charging with an areal capacity of 2 mAh cm-2. (b) Nyquist plots of both samples showing diffusion and resistance elements. XPS spectra of Li 1s for (c) BZIF-C and (d) BZIF-C-F.

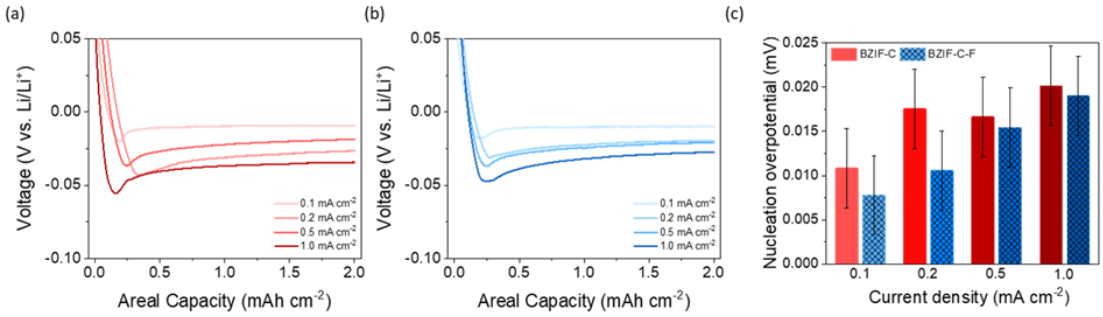

Figure 5.7. Galvanostatic voltage profiles of both samples charged to 2.0 mAh cm-2 of the first cycle at different current densities for (a) BZIF-C and (b) BZIF-C-F. (c) Overpotential required to nucleate metallic Li for Li plating for both samples.

N. The AC-impedance of both BZIF-C and BZIF-C-F anodes was measured during Li plating. The Nyquist plots in figure 5.6(b) show recognizable straight lines at nearly 45° to the y-axis in both samples at low frequencies, corresponding to the diffusion behavior at the interface. The BZIF-C-F anode exhibits a lower charge-transfer resistance (Rct, 33 Ω) compared to the BZIF-C (Rct, 47 Ω), which facilitates faster Li^+ transport. This can be explained by the significant enhancement in the chemical composition of the surface, allowing more accommodation of Li metal owing to the extra N dopant.

Furthermore, it was found that Co nanoparticles play a critical role in forming an LiF-rich SEI for uniform Li deposition [19]. This study builds on this prior finding by furtherly doping with oxidized N groups to enhance the wettability with respect to lithium. This was validated by the XPS analysis, as shown in figure 5.6(c-d), to demonstrate the main components of both BZIF-C and BZIF-C-F electrodes after charging to 2 mAh cm^{-2} at a current density of 0.2 mA cm^{-2}. Given that the electrolyte contains $LiNO_3$ as an additive, it decomposes to Li_3N and Li_2O at the SEI during cycling. It is well known that Li_3N is the key component to enhance the ionic conductivity of Li^+ in the SEI [20, 21]. More interestingly, the presence of oxidized N groups in the case of BZIF-C-F induces more Li_3N catalysis in the SEI, as shown in the

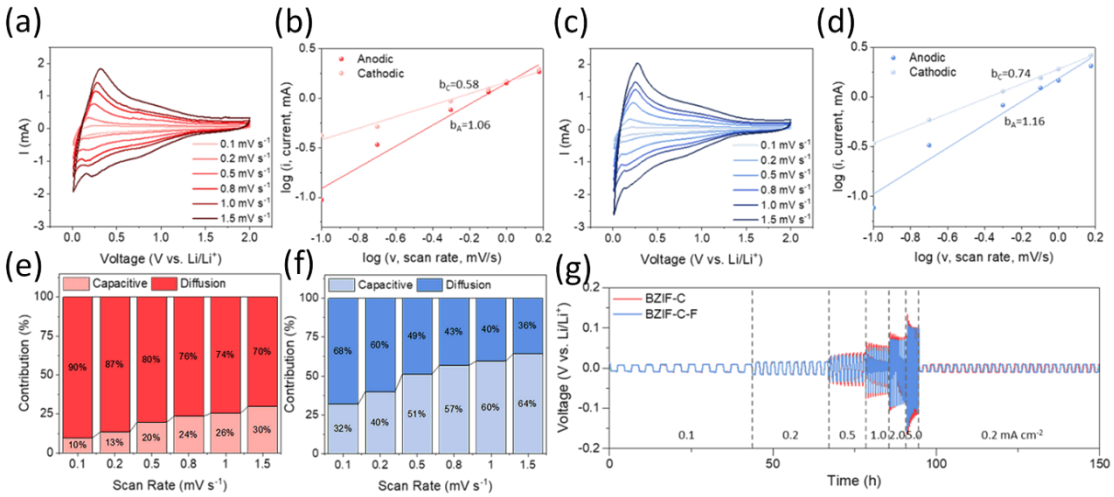

Figure 5.8. (a) CV curves at various scan rates from 0.1 to 1.5 mV s^{-1} of BZIF-C. (b) Log (i) versus log (v) plots of the anodic and cathodic current response of BZIF-C. (c) CV curves at various scan rates from 0.1 to 1.5 mV s^{-1} of BZIF-C-F. (d) Log (i) versus log (v) plots of the anodic and cathodic current response of BZIF-C-F. Contribution percentages of the capacitive and the diffusion-controlled charge as functions of the scan rate for (e) BZIF-C and (f) BZIF-C-F. (g) Voltage profiles of BZIF-C and BZIF-C-F at different current densities of 0.1, 0.2, 0.5, 1.0, 2.0, and 5 mA cm^{-2} with charge and discharge areal capacity of 0.2 mAh cm^{-2}.

XPS analysis. In figure 5.6(d), the Li_3N shows a significant peak at 54.7 eV, which stabilizes the interface and leads to a uniform Li deposition. While BZIF-C exhibits richer LiF and Li_2CO_3 contents, at 56.2 eV and 55.2 eV, respectively, than in BZIF-C-F, its ionic conductivity remains an issue due to the lower Li_3N content. As a result, the SEI of BZIF-C is more susceptible to uneven Li deposition, dead Li, and dendritic Li growth.

Electrochemical kinetic analysis of the cyclic voltammograms (CVs) provides further insights into the reaction mechanisms and the overall electrochemical performance of the anodes. Figure 5.8(a) and (c) shows the CV curves of BZIF-C and BZIF-C-F as functions of the scan rate (0.1-1.5 mV s^{-1}), whereas the slope of the log of a particular peak current plotted versus the log of the scan rate represents the parameter b (figure 5.8(b) and (d)). A pure capacitive contribution is indicated by b = 1 and a pure diffusion

contribution by b = 0.5. The linear fits show that the BZIF-C-F exhibits a relatively steeper slope than BZIF-C with slightly higher b values (b_A = 1.16 and 1.06, b_C = 0.74 and 0.58, respectively, where A and C stand for anodic and cathodic, respectively). This indicates that the electrochemical reactions in BZIF-C-F are primarily governed by the capacitive processes originating from fast near-surface activities. For example, the capacitive contribution of BZIF-C-F (59.6%) at 1.0 mV s^{-1} is 34% higher than that of BZIF-C (25.6%), as shown in figure 5.9(a-b).

The diffusion behavior in the electrode is mostly undesirable, as it also leads to slow charge storage and only short-term cyclability [22]. The diffusion-controlled intercalation processes and capacitive processes are quantitively plotted in figure 5.8(e-f), showing the percentage of each contribution as a function of scan rate. It should be noted that there is a tendency of the capacitive capacity ratio to increase with the scan rate from 0.1 to 1.5 mV s^{-1}. The increasing capacitive contribution can be ascribed to the high specific surface area and abundant active sites, which furthermore may be responsible for the excellent rate capabilities. The high proportion of capacitive behavior of the BZIF-C-F electrode could be attributed to the improved Li affinity arising from the oxidized N groups and the higher ionic conductivity of the SEI.

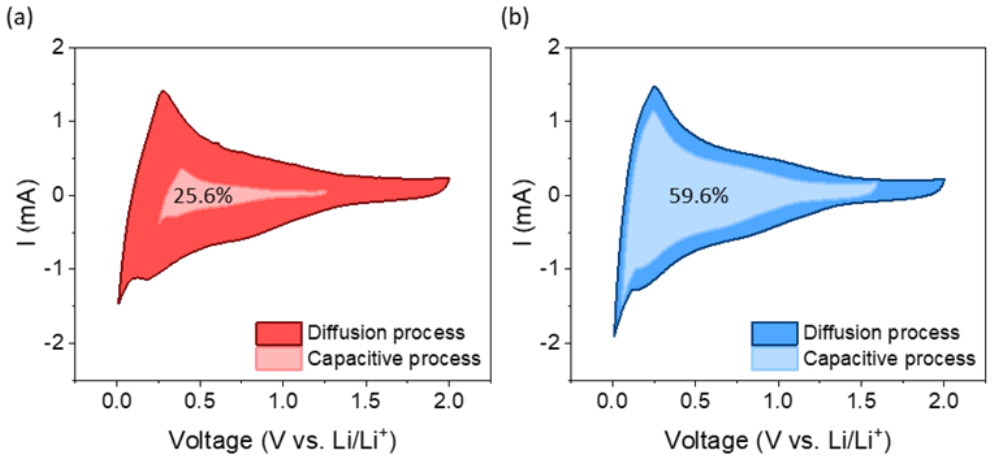

Figure 5.9. CV curves collected at a scan rate of 1.0 mV s-1, showing the capacitive contribution percentages of (a) BZIF-C and b) BZIF-C-F.

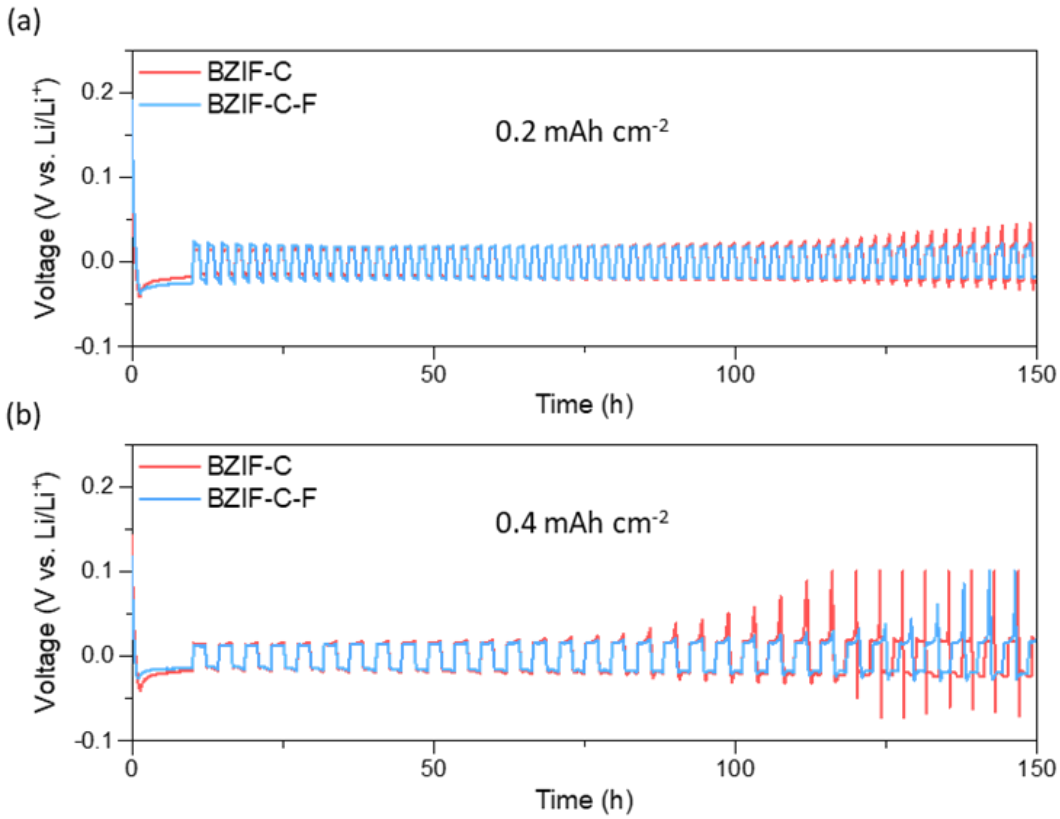

Figure 5.10. Voltage profiles of BZIF-C and BZIF-C-F electrodes at current density of 0.2 mA cm^{-2} with different areal capacities of (a) 0.2 mAh cm^{-2} and (b) 0.4 mAh cm^{-2}.

This is clearly demonstrated in the stability assessment of the material, where the rate capability was investigated at different current densities of 0.1, 0.2, 0.5, 1, 2, and 5 mA cm^{-2} after being charged initially up to 2 mAh cm^{-2} (figure 5.8(g)). At low current densities ($\leq$ 0.2 mA cm^{-2}), both BZIF-C and BZIF-C-F exhibited similar galvanostatic cycling voltage profiles. When the current density increased above 0.5 mA cm^{-2}, however, BZIF-C showed higher overpotentials compared to BZIF-C-F. While both BZIF-C and BZIF-C-F maintained stable cycling when the current density was returned to 0.2 mA cm^{-2}, the voltage profiles in figure 5.10(a-b) demonstrate a significant overpotential for BZIF-C at the current density of 0.2 mA cm^{-2} with different areal capacities. Unlike BZIF-C, BZIF-C-F showed a relatively more stable cycling performance at different areal capacities.

The reliability of BZIF-C-F in practice was examined with a full cell, using a commercial $LiFePO_4$ (LFP) cathode in the voltage range of 2.5-4.0 V. Figure 5.11(a) shows the cycling performance of full BZIF-C and BZIF-C-F cells for 100 cycles at a constant current density of 0.2 mA cm^{-2} and an areal capacity of 0.6 mAh cm^{-2}. It was found that the specific capacity of the BZIF-C full cell deteriorated significantly down to 88 mAh g^{-1}, with capacity retention of 64% after 100 cycles, while the BZIF-C-F full cell showed a relatively slower decrease in reversible capacity with a capacity retention of 89%. The Coulombic efficiency, on the other hand, remained at stable 100% over the 100 cycles, but with some disturbance after 65 cycles in the case of the full cell with BZIF-C.

Figure 5.11(c) and (f) compares the galvanostatic charge-discharge profiles for the first cycle at different current densities of full-cells employing BZIF-C and BZIF-C-F anodes. These results align with the prior findings that BZIF-C-F behavior was governed by the capacitive processes, which allows quick charge storage and long-term cyclability. Figure 5.12 supports these findings, as it shows that when the reversible capacities were finally recovered to 0.2 mA cm^{-2}, neither the BZIF-C nor the BZIF-C-F electrodes could recover their original specific capacity recorded at 0.2 mA cm^{-2}. The loss in capacity retention for BZIF-C-F, however, was much smaller (from 99% to 91%) than that of BZIF-C (from 97% to 84%). Transmission electron microscope (TEM) images were collected at the beginning of cycling and at the end of cycling for comparison. It was found that there was a significant difference between BZIF-C (figure 4d) and BZIF-C-F (figure 4g) at the end of cycling, as some lithium dendrites and dead lithium were observed on the surface of BZIF-C compared to the smooth surface and retained morphology of BZIF-C-F.

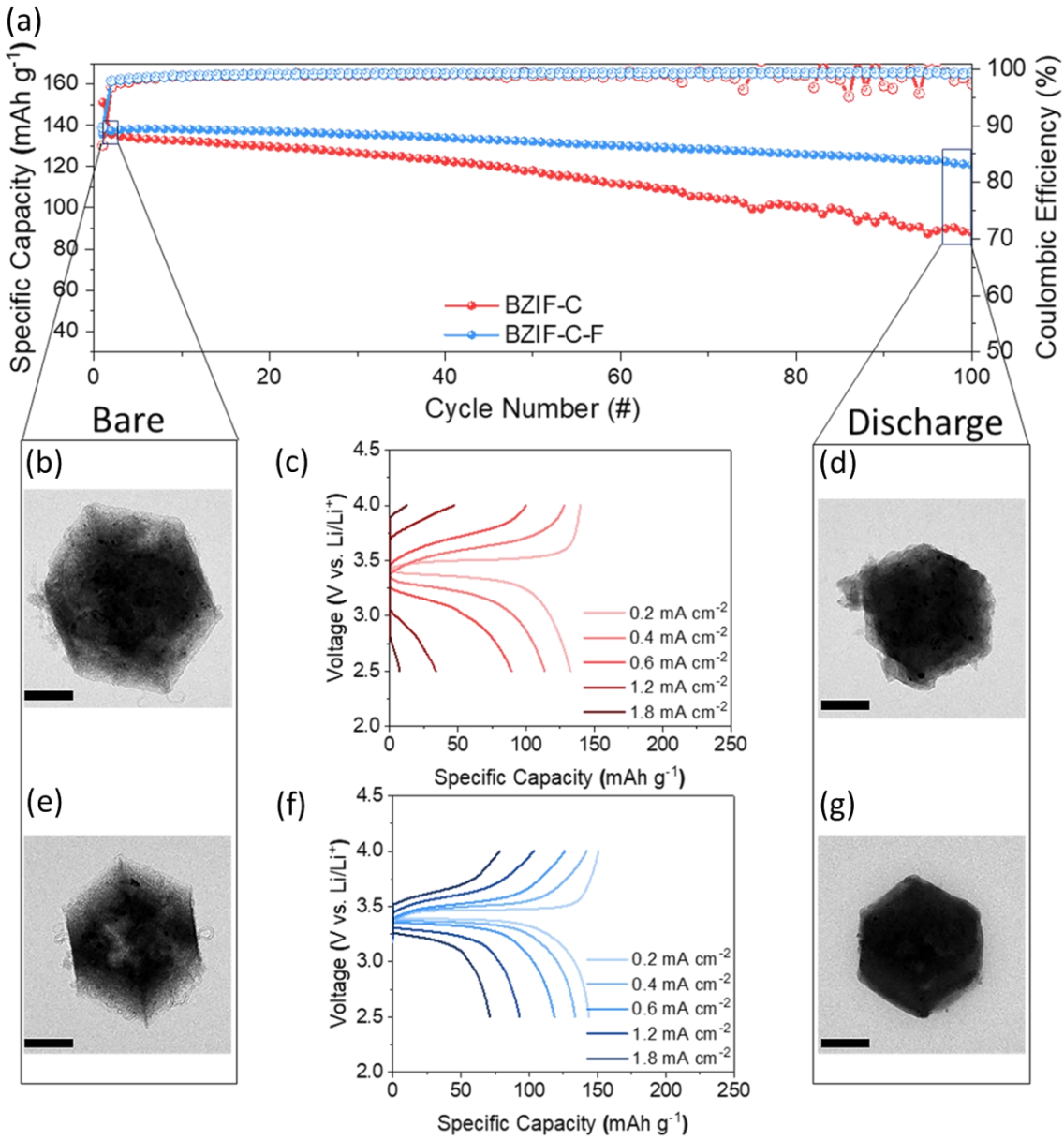

Figure 5.11. (a) Full-cell performance of BZIF-C-F and BZIF-C anodes utilizing lithium iron phosphate (LFP) cathode at a current density of 0.2 mAh cm^{-1}. The first cycle charge-discharge plots of (c) BZIF-C and (f) BZIF-C-F at different current densities. The TEM images show the morphology of the fresh samples before charging and after discharging at the end of cycling: (b, d) BZIF-C and (e, g) BZIF-C-F. All scale bars are 200 nm.

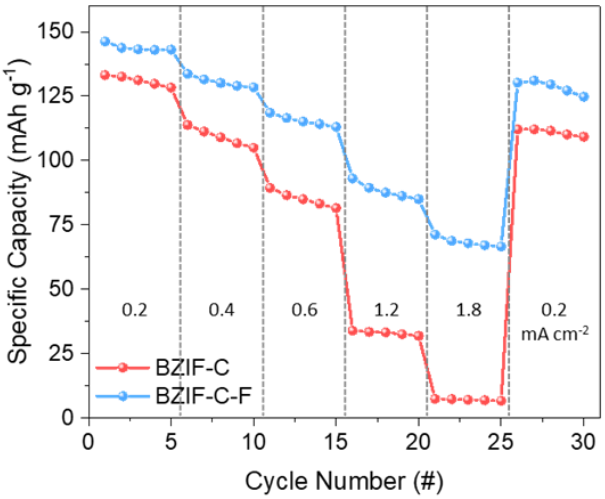

Figure 5.12. Rate capability of both samples at different applied current densities.

5.4. Conclusion

In conclusion, we found that our mesoporous carbon framework became functionalized with oxidized nitrogen groups (BZIF-C-F), which catalyzed Li_3N within the SEI, thus improving the ionic conductivity. BZIF-C-F also demonstrated an enhanced Li affinity compared to its non-functionalized counterpart, which was validated by the electrochemical and microscopic characterizations.

5.5. References

[1] A. Yoshino, The Lithium-ion Battery: Two Breakthroughs in Development and Two Reasons for the Nobel Prize. Bull. Chem. Soc. Jpn., 95 (2022) 195-197.

[2] S.A. Han, H. Qutaish, M.S. Park, J. Moon, J.H. Kim, Strategic approaches to the dendritic growth and interfacial reaction of lithium metal anode, Chem. Asian J., 16 (2021) 4010-4017.

[3] Y. Hyeon, J. Lee, H. Qutaish, S.A. Han, S.H. Choi, S.W. Moon, M.-S. Park, D. Whang, J.H. Kim, Lithium metal storage in zeolitic imidazolate framework derived nanoarchitectures, Energy Stor. Mater., 33 (2020) 95-107.

[4] T. Li, H. Liu, P. Shi, Q. Zhang, Recent progress in carbon/lithium metal composite anode for safe lithium metal batteries, Rare Met., 37 (2018) 449-458.

[5] C.-B. Jin, P. Shi, X.-Q. Zhang, J.-Q. Huang, Advances in carbon materials for stable lithium metal batteries, New Carbon Mater., 37 (2022) 1-24.

[6] J. Lee, S.A. Han, H. Qutaish, L.K. Shrestha, K. Ariga, J.H. Kim, Zeolitic Imidazolate Framework-Derived Nanoarchitectures for Lithium Metal Storage Medium, General Chemistry, 6 (2020) 190011.

[7] H. Qutaish, S.A. Han, Y. Rehman, K. Konstantinov, M.-S. Park, J. Ho Kim, Porous carbon architectures with different dimensionalities for lithium metal storage, Sci. Technol. Adv. Mater., 23 (2022) 169-188.

[8] H. Qutaish, J. Lee, Y. Hyeon, S.A. Han, I.-H. Lee, Y.-U. Heo, D. Whang, J. Moon, M.-S. Park, J.H. Kim, Design of cobalt catalysed carbon nanotubes in bimetallic zeolitic imidazolate frameworks, Appl. Surf. Sci., 547 (2021) 149134.

[9] H.R. Shin, J. Yun, G.H. Eom, J. Moon, J.H. Kim, M.-S. Park, J.-W. Lee, S.X. Dou, Mechanistic and nanoarchitectonics insight into Li–host interactions in carbon hosts for reversible Li metal Storage, Nano Energy, 95 (2022) 106999.

[10] X. Chen, X.-R. Chen, T.-Z. Hou, B.-Q. Li, X.-B. Cheng, R. Zhang, Q. Zhang, Lithiophilicity chemistry of heteroatom-doped carbon to guide uniform lithium nucleation in lithium metal anodes, Sci. Adv., 5 (2019) eaau7728.

[11] W. Liu, P. Liu, D. Mitlin, Review of emerging concepts in SEI analysis and artificial SEI membranes for lithium, sodium, and potassium metal battery anodes, Adv. Energy Mater., 10 (2020) 2002297.

[12] H. Ye, S. Xin, Y.X. Yin, Y.G. Guo, Advanced porous carbon materials for high-efficient lithium metal anodes, Adv. Energy Mater., 7 (2017) 1700530.

[13] R.D. Deshpande, D.M. Bernardi, Modeling solid-electrolyte interphase (SEI) fracture: coupled mechanical/chemical degradation of the lithium ion battery, J. Electrochem. Soc., 164 (2017) A461.

[14] Y. Guo, H. Li, T. Zhai, Reviving lithium-metal anodes for next-generation high-energy batteries, Adv. Mater., 29 (2017) 1700007.

[15] S.H. Choi, Y. Hyeon, H.R. Shin, G.H. Eom, H.T.T. Pham, D. Whang, S.Y. Kim, J.-W. Lee, J.H. Kim, M.-S. Park, Critical role of surface craters for improving the reversibility of Li metal storage in porous carbon frameworks, Nano Energy, 88 (2021) 106243.

[16] G.H. Eom, S.A. Han, J.H. Suh, J.H. Kim, M.-S. Park, Enriched Cavities to ZIF-8-Derived Porous Carbon for Reversible Metallic Lithium Storage, ACS Appl. Energy Mater., 4 (2021) 14520-14525.

[17] J. Yun, B.-K. Park, E.-S. Won, S.H. Choi, H.C. Kang, J.H. Kim, M.-S. Park, J.-W. Lee, Bottom-up lithium growth triggered by interfacial activity gradient on porous framework for lithium-metal anode, ACS Energy Lett., 5 (2020) 3108-3114.

[18] J. Lee, S.H. Choi, H. Qutaish, Y. Hyeon, S.A. Han, Y.-U. Heo, D. Whang, J.-W. Lee, J. Moon, M.-S. Park, Structurally stabilized lithium-metal anode via surface chemistry engineering, Energy Stor. Mater., 37 (2021) 315-324.

[19] J. Lee, M.-S. Park, J.H. Kim, Stabilizing Li-metal host anode with LiF-rich solid electrolyte interphase, Nano Converg., 8 (2021) 1-8.

[20] S. Liu, X. Ji, N. Piao, J. Chen, N. Eidson, J. Xu, P. Wang, L. Chen, J. Zhang, T. Deng, An inorganic-rich solid electrolyte interphase for advanced lithium-metal batteries in carbonate electrolytes, Angew. Chem. Int. Ed., 60 (2021) 3661-3671.

[21] Z. Piao, P. Xiao, R. Luo, J. Ma, R. Gao, C. Li, J. Tan, K. Yu, G. Zhou, H.M. Cheng, Constructing a Stable Interface Layer by Tailoring Solvation Chemistry in Carbonate

Electrolytes for High-Performance Lithium-Metal Batteries, Adv. Mater., 34 (2022) 2108400.

[22] J. Wang, J. Polleux, J. Lim, B. Dunn, Pseudocapacitive contributions to electrochemical energy storage in TiO2 (anatase) nanoparticles, J. Phys. Chem. C, 111 (2007) 14925-14931.

CHAPTER 6 . CONCLUSIONS AND FUTURE DIRECTIONS

6.1. Conclusion

A significant aspect of this doctoral research focused on creating Zeolitic Imidazolate Frameworks-derived Carbon (ZIF-C) as 3D host materials for Li-metal anodes. The rationale for selecting ZIF-C in this thesis is not only its versatility in tailoring constituent geometry, size, and functionality to meet specific application requirements but also its remarkable properties such as robust mechanical strength, extensive surface area and pore volume, and sufficient electrical conductivity, which make it a promising candidate for cost-effective practical applications. Nonetheless, these host materials might face challenges related to poor Li wettability, causing substantial nucleation barriers and surface electrodeposition of Li metal. This, in turn, can lead to dendritic growth and safety concerns.

Herein, this thesis provides a comprehensive understanding of ZIF-C surface chemistry and structure through theoretical and experimental characterization. Initially, we investigated the effect of varying the ratios of metallic contents (Co/Zn) in ZIF-C to achieve remarkable porous structures with high pore volumes and large surface areas. We found that the pore size tends to increase with Co content, where mesoporous structures are observed in porous carbon materials derived from Co-containing ZIFs. The major contribution and novelty has been the improvement of Li adsorption via mesoporous and microporous structures which exploits the balance between Li ion diffusion and adsorption. Additionally, at a certain size of Co content, carbon nanotubes could be catalyzed which hugely impact the electrical properties of the materials.

To further emphasize the impact that this bimetallic combination of Co/Zn on Li deposition behavior, we theoretically demonstrated and experimentally correlated the plating mechanism of Li on the surface of the carbon host framework. We found that the N heteroatoms tend to induce Li dendritic growth, while the Co-N4 heteroatoms induce the desired axial Li growth. This suggests that the surface chemistry of the host material plays an important role in the deposition behavior, hence optimizing the content of heteroatoms is highlighted.

Building on these conclusions, we proceeded with surface functionalization as a technique to increase electronegativity towards Li and decrease the Li nucleation overpotential. From that, we functionalized ZIF-C with oxidized nitrogen groups, which demonstrated an enhanced Li affinity compared to its non-functionalized counterpart, which was validated by the electrochemical and microscopic characterizations. The functionalized ZIF-C also catalyzed Li_3N within the SEI, thus improving its ionic conductivity and electrochemical performance.

6.2. Limitations and Future Directions

This dissertation presents an innovative approach to comprehending the lithium growth mechanism and establishes a foundational structure for the development of high-performance anodic ZIF-C host materials. A multitude of challenges persist and necessitate extensive research and enhancement. Owing to the complexity of lithium adsorption processes and the various factors influencing lithium cluster growth, additional scientific investigation is imperative. Factors to be considered encompass surface topology, electrolyte composition and concentration, solvent selection, operational temperature, and cycling duration. These elements have the potential to modify the number of active sites, lithium-ion solubility and mobility, solid electrolyte

interphase (SEI) layer permeability, and electrode stability. Consequently, the optimization of these factors is essential for the creation of superior battery materials. Moreover, comprehensive experimental and theoretical investigations focusing on the SEI formation mechanism is needed, as the SEI layer significantly contributes to the mitigation of further side reactions between the electrolyte and the anode and facilitates uniform lithium deposition through the regulation of ion flux towards the collector.

The lithiophilicity of porous carbon constitutes a crucial parameter that can enhance the deposition and nucleation behavior of lithium metal, thereby enhancing stability and extending the battery life. Consequently, fundamental parameters relating to the host material's chemical composition should be considered to elevate the lithium affinity of the anode material, encompassing electronegativity, charge transfer, and local dipoles. The principal findings indicate that certain functional groups increase the lithium nucleation overpotential, while others confer heightened electronegativity towards lithium, resulting in a reduced nucleation barrier. Altering the local dipole parameter via co-doping represents another approach to achieve high lithium affinity. Furthermore, it has been determined that charge transfer plays a critical role in reducing the nucleation barrier energy, with a charge transfer of 0.9 electrons serving as the threshold for the enhancement of binding energy.

Finally, the need for higher energy density results in a greater demand to further lower the material density of the utilized carbon host at the anode. More importantly, cost-effective synthesis approaches need to be assessed for the manufacture of these composites in order to facilitate the product translation and future process development. A particular mention is the emerging interest in carbon derived from various sources, such as biomass, polymers, and even waste. These alternative sources of carbon offer a sustainable and cost-effective approach to materials synthesis, aligning with global initiatives to reduce

environmental impact. Their utilization not only contributes to the development of effective energy storage devices but also promotes a circular economy by turning waste streams into valuable resources. By addressing these critical areas, we will be paving the way for the next generation of energy storage solutions, characterized by increased efficiency, safety, and sustainability.

APPENDIX A: LIST OF ABBREVIATIONS & SYMBOLS

Abbreviations

0D	Zero-dimensional
1D	One-dimensional
2D	Two-dimensional
2-MIM	2-methylimidazolate
3D	Three-dimensional
BET	Brunauer-Emmett-Teller
BJH	Barrett-Joyner-Halenda
BZIF-C	Bimetallic ZIF-carbon
CB	Carbon black
CE	Coulombic efficiency
CNTs	Carbon nanotubes
CV	Cyclic voltammetry
DFT	Density functional theory
FE-SEM	Field Emission Scanning Electron Microscopy
GO	Graphene oxide

LAB	Lithium air battery
LIB	Lithium-ion battery
LMB	Lithium metal battery
LSB	Lithium sulfur battery
MOFs	Metal organic frameworks
OCV	Open circuit voltage
PCF	Porous carbon framework
rGO	Reduced graphene oxide
SEI	Solid electrolyte interphase
TEM	Transmission electron microscope
TGA	Thermogravimetric analysis
VASP	Vienna Ab-initio Simulation Package
vs.	Versus
XPS	X-ray photoelectron spectroscopy
XRD	X-ray diffraction
PAN	polyacrylonitrile
PCF	porous carbon framework
ZIF	Zeolitic imidazolate framework
GCF	graphitized carbon fibers

Symbols

ΔG_{het}^{*}	Energy barrier for heterogeneous nucleation
$s(\theta)$	Shape factor
ΔG_{hom}^{*}	Energy barrier for homogeneous nucleation
$d\varepsilon_{ij}^{e}$	Elastic strain
E	Young's modulus
v	Poisson's ratio
σ_{kk}	Diagonal components of stress
δ_{ij}	Kronecker delta
$\dot{\lambda}$	Scalar coefficient
Ω	Partial molar volume
c	Normalized Li concentration
D	Li diffusion coefficient
α	Constant to determine the thickness of phase boundary
ρ_{diff}	Charge density difference
e	Electric charge
D	Ambipolar diffusion coefficient
C	Li^{+} concentration in the electrolyte
J	Effective current density

μ_{a}	Anionic mobility
μ_{Li}	Li-ion mobility
$\partial C/\partial x$	Change in ionic concentration
L	Inter-electrode distance
τ	Sand's time
t_a	Anionic transference number
J_{cc}	Critical current density
J_{lim}	Diffusion-limited current density
γ	Surface tension
ΔP	Pressure difference
R_1	Orthogonal curvature radii
R_2	Orthogonal curvature radii
Q_{Li}	Volumetric capacity of Li
V	Pore volume
$Q_{theortical,g}$	Theoretical gravimetric capacity
Q_c	Theoretical volumetric capacity of carbon
m_c	Mass of carbon framework
m_{Li}	Mass of Li metal

APPENDIX B: LIST OF FIGURES, TABLES & NOTES

Figure 1.1. Schematic diagram showing the history and development direction of secondary batteries, with the inset showing the energy densities of the different types.

Table 1.1. Journal articles for the thesis compilation.

Figure 2.1. Schematic illustration of the failure mechanisms that occur in Li metal anode; Infinite volume expansion of Li metal causes instability of SEI and induces mechanical stresses that destroy the integrity of the anode. Extremely thick SEI layer causes high interfacial impedance. The dendritic growth forms in various dendritic structures, such as trees and whiskers. The further extension of these Li dendrites can lead to a loss in their electric contact with the anode during stripping, resulting in "dead Li". Furthermore, long dendrites can cause short circuits.

Figure 2.2. a) Schematic illustration showing the early stages of Li dendritic growth at different current densities. [44] b) The different types of Li dendritic growth and their interactions with a nanoporous alumina separator under different current density conditions. AAO: anodic aluminium oxide. [54]

Figure 2.3. The main regimes of the initial stage behavior of Li nucleation and growth. a) Above the black bold curve, there is a zone of stable Li growth. Below the blue curve is the undesirable Li growth zone. The solid grey curves represent the fixed incubation times. The dotted grey curves highlight the initial velocities of Li nucleation. [58] b) Schematic illustration of the size and density of Li nuclei deposited on Cu current collectors at different nucleation overpotentials. [59]

Figure 2.4. a) Schematic representation of the effects of different pore sizes on Li deposition behavior. [71] b) The hollow carbon nanospheres act as a scaffold to stabilize the SEI layer. The scanning electron microscopy (SEM) image on the right displays no dendritic growth after Li deposition. [74] c) Schematic illustration of the behavior of Li plating on an electrical conductivity-controlled 3D host and a 3D conductive host. The SEM images present different views of the pristine partially reduced graphene oxide –graphene foam (PrGO–GF)/Cu electrode. [89] d) LiF-rich SEI formation on Co-ZIF-C electrode stabilizes the cycling performance. The SEM image shows no dendritic growth after cycling. [90]

Figure 2.5. a) Schematic illustration of how lithiophilic pores within a suitable host material can store the Li-metal. When the sum of the half angle of the cavity and the contact angle of the nucleus on the substrate is below 90°, the energy barrier will be zero. [15] b) Typical voltage profile of galvanostatic Li deposition (black) and double pulse potentiostatic Li deposition (red). [59] c) Modelling of heteroatom-doped carbon versus pristine graphene model. The bar chart below is a summary of the calculated binding energy between different heteroatom-doped carbons and a Li atom. [91]

Figure 2.6. a) SEM images showing the morphology of the pristine GCF, intercalated GCF, and GCF charged up to 2 mAh cm^{-2}. The galvanostatic discharge profile with inset schematic diagrams of lithium behavior during cycling is shown below. All scale bars in (a) are 10 μm. [95] b) The schematic illustration on the left shows that the pristine carbon is not Li-wetting, but after being functionalized with heteroatoms, it becomes superwetting. The schematic illustration on the right side shows that, after functionalizing graphitized fiber carbon (GFC) with amine groups, it becomes superwetting, and the Li grows axially. The cycling performance and CE of Li-

C||NMC622 and Li||NMC622 cells, demonstrating long-term cycling. An SEM image of amine functionalized GFC shows smooth growth of Li. [96]

Table 2.1. Electrochemical performances of Li-metal anodes utilizing 1D carbon-based frameworks.

Figure 2.7. a) Schematic illustration of the axial growth of Li on an rGO substrate. The red dashed lines are the graphene zigzag lattice directions. The electrochemical performance of the rGO demonstrates the stability of the symmetrical cell up to 500 hours SEM images of the rGO show the axial growth of the Li metal. Scale bars in (a) are 100 μm and all scale bars in insets are 50 μm. [99] b) Schematic illustration of different doped heteroatoms in the graphene. The middle bar chart illustrates the binding energy calculated between the Li atom and different functional groups. The schematic illustration below and inset SEM image show the smooth Li growth. The right-side schematic shows the total electron density (blue) of isolated atoms on graphene and pyrrolic-N. The red regions indicate less electron density. [100]

Table 2.2 Electrochemical performances of Li-metal anodes utilizing 2D carbon-based frameworks.

Figure 2.8. a) Schematic illustration of NGCF, with the SEM image showing the smooth Li deposition without dendritic growth. The graph below presents the difference in CE between NGCF and Cu current collector at areal capacity of 2 mAh cm^{-2} during Li plating/stripping. [101] b) Schematic illustration of the Li deposition behaviour on the Zn/N@amorphous carbon and Co/N@graphitic carbon. The transmission electron microscope (TEM) images show the morphology of the Li deposits. The schematic diagram below shows the charge densities and the charge transfer behaviour on the N-doped carbon and Co-N co-doped carbon. The voltage profiles of the

Zn/N@amorphous carbon and Co/N@graphitic carbon are on the right, and their cycling performances are at the bottom. Scale bares in (b) are 50 nm. [103]

Table 2.3 Electrochemical performances of Li-metal anodes utilizing 3D carbon-based frameworks.

Figure 2.9. a) A voltage profile of galvanostatic Li deposition on a copper substrate at 10 μA cm^{-2}. The inset schematic shows the mechanism of Li nucleation. The right-side voltage profile is of galvanostatic Li deposition on a gold substrate at 10 μA cm^{-2}. The inset schematic diagram demonstrates how the solid solution buffer layer of Au is dissolved in Li and reduces the nucleation energy. [104] b) Voltage profiles of various materials with some Li solubility compared to materials with negligible Li solubility. [104]

Figure 2.10. a) Schematic illustration and an SEM image that show the Au nanoparticles inside hollow carbon spheres followed by Li growth after cycling. The right-side images present the nucleation overpotential of the hollow carbon. The inset schematics and SEM images show the Au nanoparticles inside the hollow carbon and the smooth Li deposition compared to a carbon shell. Below are the electrochemical performances of different electrodes when cycled in alkyl carbonate electrolyte. Scale bare for TEM in (a) is 100 nm and all scale bares for inset SEM images are 10 μm. [104] b) Schematic illustration showing the Li deposition behaviour on the Ag@CMFs. The schematic on the top right explains the Li deposition process on Ag@CMFs. The middle schematics model the Ag, Cu, graphene, and nitrogen-doped carbons. A summary of the calculated binding energies of Li atom with Cu, Ag, graphene, and nitrogen-doped carbons is also shown (middle right side). The bottom graph shows the electrochemical performances of the Cu, Ag@CMFs and CMFs at 1 mA cm^{-2}. [106]

Table 2.4. Electrochemical performances of Li-metal anodes utilizing carbon-based nanocomposite frameworks. NPs stands for nanoparticles.

Figure 2.11. A brief history of research on the application of MOFs in Li batteries.

Figure 2.12. (a) TEM image of 2D MOF nanosheet and schematic diagram of the structure. (b) SEM images of the surface and cross-sectional (lower inset) morphologies of bare Cu electrode with 1.0 mAh cm^{-2} Li deposition at a current density of 0.5 mA cm^{-2}. (c) SEM images of the surface and cross-sectional (lower inset) morphologies of Cu-MOF electrode with 1.0 mAh cm^{-2} Li deposition at a current density of 0.5 mA cm^{-2}. The supper insets of c and d are photographs of the electrodes. (d) Cycling performances of bare Cu electrode and Cu-MOFs electrode at the current density of 2 mA cm^{-2} with a lithiation capacity of 1 mAh cm^{-2}.[113]

Figure 2.13. (a) Schematic illustration showing dual-phase Li storage in a porous carbon framework (PCF) structure. Li metal is stored in the pores of PCF, and Li ions are intercalated on the PCF surface. (b) Cross-sectional SEM images of Super-P obtained after charging to 1.0 mAh cm^{-2}. (c) Cross-sectional SEM images of PCF-E obtained after charging to 1.0 mAh cm^{-2}. (d) Cycling performances of Super-P and PCF-E at a constant capacity of 0.2 mAh cm^{-2} at 0.2 mA cm^{-2}.[141]

Figure 2.14. (a) Surface structures of porous carbon framework (PCF) and structure with surface craters (SC-PCF). (b) Schematic illustrations showing the ion transport, which was used to calculate the MacMullin numbers of PCF and SC-PCF electrodes. (c) The Li plating and stripping behavior of PCF and SC-PCF electrodes.[128]

Table 2.5. Summary of recent studies in which MOFs or MOF derived materials were applied as host materials for LMBs.

Figure 3.7. (a) The powder conductivity of all carbonized ZIFs at 47.75 MPa. (b) Porous characteristics of all carbonized ZIF materials. Scale bars in SEM images in (a): 1 μm. The overall pressure dependences of electrical conductivities are summarized in Figure 3.8.

Figure 3.8. Pressure dependence of the electrical conductivity of all as-prepared carbonized ZIFs.

Figure 3.9. Particle size distributions of C-BZ1, C-BZ2, and C-BZ3. Scale bars: 1 μm.

Figure 4.1. (a) and (b) Scanning electron microscope (SEM) images showing the morphology of BZIF-C. (c) Transmission electron microscope (TEM) and high-resolution (HR)-TEM images of BZIF-C with corresponding energy dispersive X-ray spectroscopy (EDX) elemental mapping images in the green box.

Figure 4.2. (a) XRD pattern and (b) Raman spectrum of BZIF-C. (c) Electrical conductivity of BZIF-C under compressed conditions with different pressures. (d) and (e) N_2 adsorption/desorption isotherm and average pore diameter, respectively.

Figure 4.3. (a)-(c) XPS spectra of the BZIF-C measured before and after etching of the sample: Co 2p (a), C 1s (b), and N 1s (c). (d) The surface elemental ratio of the elements is based on the XPS results.

Figure 4.4. (a) Schematic illustration of lithiation sites in graphite and different types of N doped graphite structure: Graphite Quaternary, Pyridinic, Pyrrolic, Co-N4. (b)Formation energies of the Li_1 adsorption on the pristine graphite and on four different defect structures.

Figure 4.5. (a) Schematic representation of the deposition and growth during the Li plating process. First, Li sheds off the solvent molecules and transform into Li adatom.

Then, the Li cluster form vertical/axial growth based on the heteroatom type. (b) The structure of Li intercalation from Li_1 to Li clusters (Li metal) with three types of nitrogen doping in graphite defects.

Figure 4.6. (a) Another possibility of atomic configuration of Li growth, showing axial Li growth on pyridinic N and pyrrolic N and vertical Li growth on Co-N4 structure. (b) The formation energy obtained from Figure 4.5(b) and Figure 4.6(a) to compare which of the two Li growth forms (axial or vertical) is more likely to occur on pyridinic N, pyrrolic N and Co-N4 structures. In Co-N4, the formation energy for vertical growth is smaller than that of the axial growth, leading to a tendency for axial Li growth.

Figure 4.7. (a) The formation energy by the number of Li ions in a cluster and the different sites for Li in three different types of N-doped graphite. (b) Bader net charge of nitrogen and cobalt by number of Li in N-doped graphite. (c) Size of charge density difference and defect size in the form of Li clusters and (d) side views. The red/yellow areas represent the defect/charge density difference sizes, respectively.

Figure 4.8. (a)-(c) Local structure of lithiation step by number of Li adatoms in stable sites of n/Co doped graphite.

Figure 4.9. Charge density differences when Lis are stored step by step in pyridinic (a), pyrrolic (b), and Co-N4(c) defects.

Figure 4.10. (a) and (b) Voltage hysteresis observations in first cycle charging with the areal capacity of 2 mAh cm^{-2} at different current densities. (c) Nucleation overpotential comparison between BZIF-C and Cu foil at different current densities. (d) and (e) Voltage profiles with cycling of the BZIF-C and Cu foil electrodes at 0.2 mA cm^{-2} with different charge/discharge capacities of 0.2 mAh cm^{-2} and 0.4 mAh cm^{-2}, respectively.

Figure 4.11. Microscopic observations of Li-metal plated Cu foil and BZIF-C. (a) and (b) SEM images of the Cu foil electrode. (c) and (d) SEM of the BZIF-C electrode. (e) and (f) TEM of the BZIF-C.

Figure 4.12. (a) Elemental components on the surface of the BZIF-C anode after Li-plating analyzed by X-ray photoelectron spectroscopy (XPS). (b) The first cycle charge-discharge plots of BZIF-C in conjunction with lithium iron phosphate (LFP) cathode at different current densities, and (c) full-cell performance of BZIF-C anode at different current densities.

Figure 5.1. Scanning electron microscope (SEM) images showing the morphology of BZIF-C and BZIF-C-F. The enlarged schematic illustrations demonstrate the main elements on the surfaces of these materials. The XPS spectra show the main difference between the two samples. The schematic illustrations on the right show the behaviour of the functionalized material compared to its non-functionalized counterpart in terms of Li affinity and deposition uniformity.

Figure 5.2. SEM images of (a-b) BZIF-C and (c -d) BZIF-C-F. TEM and EDS mapping images of (e-f) BZIF-C and (g-h) BZIF-C-F, showing the elemental content in the material.

Figure 5.3. (a) XRD spectra, (b) Raman spectra, (C) electrical conductivity.

Figure 5.4. (a) N_2 adsorption-desorption isotherms, (b) specific surface area and pore volume, and (c) pore size distribution of BZIF-C and BZIF-C-F.

Table 5.1. The areal ratios (%) of different elements utilizing XPS analysis

Figure 5.5. XPS analysis of N 1s spectra of (a) BZIF-C and (b) BZIF-C-F electrodes, and C 1s spectra of (c) BZIF-C and (d) BZIF-C-F.

Figure 5.6. (a) Voltage hysteresis observations of both samples in the first cycle charging with an areal capacity of 2 mAh cm^{-2}. (b) Nyquist plots of both samples showing diffusion and resistance elements. XPS spectra of Li 1s for (c) BZIF-C and (d) BZIF-C-F.

Figure 5.7. Galvanostatic voltage profiles of both samples charged to 2.0 mAh cm^{-2} of the first cycle at different current densities for (a) BZIF-C and (b) BZIF-C-F. (c) Overpotential required to nucleate metallic Li for Li plating for both samples.

Figure 5.8. (a) CV curves at various scan rates from 0.1 to 1.5 mV s^{-1} of BZIF-C. (b) Log (i) versus log (v) plots of the anodic and cathodic current response of BZIF-C. (c) CV curves at various scan rates from 0.1 to 1.5 mV s^{-1} of BZIF-C-F. (d) Log (i) versus log (v) plots of the anodic and cathodic current response of BZIF-C-F. Contribution percentages of the capacitive and the diffusion-controlled charge as functions of the scan rate for (e) BZIF-C and (f) BZIF-C-F. (g) Voltage profiles of BZIF-C and BZIF-C-F at different current densities of 0.1, 0.2, 0.5, 1.0, 2.0, and 5 mA cm^{-2} with charge and discharge areal capacity of 0.2 mAh cm^{-2}.

Figure 5.9. CV curves collected at a scan rate of 1.0 mV s^{-1}, showing the capacitive contribution percentages of (a) BZIF-C and b) BZIF-C-F.

Figure 5.10. Voltage profiles of BZIF-C and BZIF-C-F electrodes at current density of 0.2 mA cm^{-2} with different areal capacities of (a) 0.2 mAh cm^{-2} and (b) 0.4 mAh cm^{-2}.

Figure 5.11. (a) Full-cell performance of BZIF-C-F and BZIF-C anodes utilizing lithium iron phosphate (LFP) cathode at a current density of 0.2 mAh cm^{-1}. The first cycle charge-discharge plots of (c) BZIF-C and (f) BZIF-C-F at different current densities. The TEM images show the morphology of the fresh samples before charging

and after discharging at the end of cycling: (b, d) BZIF-C and (e, g) BZIF-C-F. All scale bars are 200 nm.

Figure 5.12. Rate capability of both samples at different applied current densities.

APPENDIX C: LIST OF PUBLICATIONS & AWARDS

1. **Qutaish, H**., Chang, H., Suh, J.H., Han, S.A., Yum, H.Y., Park, M.S., Moon, J. and Kim, J.H., 2023. Growth Mechanism of Lithium Clusters on the Surface of Porous Carbon Framework for Lithium Metal Batteries. *ACS Materials Letters*, *5*(6), pp.1593-1600.

2. Park, S., Chaudhary, R., Han, S.A., **Qutaish, H**., Moon, J., Park, M.S. and Kim, J.H., 2023. Ionic conductivity and mechanical properties of the solid electrolyte interphase in lithium metal batteries. *Energy Mater.*, *3*, p.300005.

3. Han, S.A., **Qutaish, H.,** Lee, J.W., Park, M.S. and Kim, J.H., 2023. *Metal-organic framework derived porous structures towards lithium rechargeable batteries.* EcoMat, *5*(2), p.e12283.

4. **Qutaish, H.**, Suh, J., Han, S.A., Kim, S., Park, M.S. and Kim, J.H., 2022. *Regulation of ionic conductivity and lithium affinity of porous carbon framework in Li metal batteries through oxidized nitrogen groups.* Applied Surface Science, 605, p.154757.

5. **Qutaish, H.**, Han, S.A., Rehman, Y., Konstantinov, K., Park, M.S. and Ho Kim, J., 2022. *Porous carbon architectures with different dimensionalities for lithium metal storage*. Science and Technology of Advanced Materials, *23*(1), pp.169-188.

6. Rehman, Y., **Qutaish, H.**, Kim, J.H., Huang, X.F., Alvi, S. and Konstantinov, K., 2022. *Microenvironmental Behaviour of Nanotheranostic Systems for Controlled Oxidative Stress and Cancer Treatment.* Nanomaterials, *12*(14), p.2462.

7. Rehman, Y., **Qutaish, H.**, Kim, J.H., Huang, X.F. and Konstantinov, K., 2022. *Nanoarchitectonics of (110) directed polyethylene glycol stabilized cerium nanoparticles for UV filtering applications*. Journal of Materials Science, *57*(27), pp.12848-12864.

8. Al-Attafi, K., Nattestad, A., **Qutaish, H.**, Park, M.S., Shrestha, L.K., Ariga, K., Dou, S.X. and Ho Kim, J., 2021. *Solvothermally synthesized anatase TiO2 nanoparticles for photoanodes in dye-sensitized solar cells.* Science and technology of advanced materials, *22*(1), pp.100-112.

9. Han, S.A., **Qutaish, H.**, Park, M.S., Moon, J. and Kim, J.H., 2021. *Strategic approaches to the dendritic growth and interfacial reaction of lithium metal anode*. Chemistry–An Asian Journal, *16*(24), pp.4010-4017.

10. Lee, J., Choi, S.H., **Qutaish, H.**, Hyeon, Y., Han, S.A., Heo, Y.U., Whang, D., Lee, J.W., Moon, J., Park, M.S. and Kim, J.H., 2021. *Structurally stabilized lithium-metal anode via surface chemistry engineering.* Energy Storage Materials, *37*, pp.315-324.

11. **Qutaish, H.**, Lee, J., Hyeon, Y., Han, S.A., Lee, I.H., Heo, Y.U., Whang, D., Moon, J., Park, M.S. and Kim, J.H., 2021. *Design of cobalt catalysed carbon nanotubes in bimetallic zeolitic imidazolate frameworks.* Applied Surface Science, 547, p.149134.

12. Hyeon, Y., Lee, J., **Qutaish, H.**, Han, S.A., Choi, S.H., Moon, S.W., Park, M.S., Whang, D. and Kim, J.H., 2020. *Lithium metal storage in zeolitic imidazolate framework derived nanoarchitectures*. Energy Storage Materials, *33*, pp.95-107.

13. Mueen, R., Morlando, A., **Qutaish, H.**, Lerch, M., Cheng, Z. and Konstantinov, K., 2020. *ZnO/CeO2 nanocomposite with low photocatalytic activity as efficient UV filters*. Journal of Materials Science, *55*(16), pp.6834-6847.

14. Lee, J., Han, S.A., **Qutaish, H.**, Shrestha, L.K., Ariga, K. and Kim, J.H., 2020. *Zeolitic Imidazolate Framework-Derived Nanoarchitectures for Lithium Metal Storage Medium*. General Chemistry, *6*(1), p.190011.

Awards

- Postgraduate Student Excellence Award (2022), Institute for Superconducting & Electronic Materials, Australian Institute of Innovative Materials, University of Wollongong, Australia.

- Postgraduate Student Best Paper Award (2021), Institute for Superconducting & Electronic Materials, Australian Institute of Innovative Materials, University of Wollongong, Australia.
- Matching Scholarship (2019-2023), Institute for Superconducting & Electronic Materials, Australian Institute of Innovative Materials, University of Wollongong, Australia.
- International Postgraduate Tuition Award (2019-2023), Institute for Superconducting & Electronic Materials, Australian Institute of Innovative Materials, University of Wollongong, Australia.